

KDM4C inhibition blocks tumor growth in basal breast cancer by promoting cathepsin L-mediated histone H3 cleavage

Received: 17 October 2023

Accepted: 15 April 2025

Published online: 02 June 2025

 Check for updates

Zheqi Li ^{1,2,3,12}, Guillermo Peluffo^{1,2,3,12}, Laura E. Stevens^{1,2,3}, Xintao Qiu ⁴, Marco Seehawer ^{1,2,3}, Amatullah Tawawalla¹, Xiao-Yun Huang¹, Shawn B. Egri⁵, Shaunak Raval⁵, Maeve McFadden ⁵, Clive S. D'Santos⁶, Eva Papachristou ⁶, Natalie L. Kingston ¹, Jun Nishida ^{1,2,3}, Kyle E. Evans¹, Ji-Heui Seo^{1,2,3}, Kendell Clement ⁷, Daniel Temko ^{7,8,9}, Muhammad Ekram ^{1,2,3}, Rong Li ⁴, Matthew G. Rees ⁵, Melissa M. Ronan ⁵, Jennifer A. Roth ⁵, Anton Simeonov ¹⁰, Stephen C. Kales ¹⁰, Ganesha Rai¹⁰, Madhu Lal-Nag¹⁰, David J. Maloney¹⁰, Ajit Jadhav ¹⁰, Franziska Michor ^{5,7,8,9}, Alex Meissner ^{5,7}, Justin M. Balko ¹¹, Jason S. Carroll ⁶, Matthew L. Freedman^{1,2,3,4,5}, Jacob D. Jaffe⁵, Malvina Papanastasiou ⁵, Henry W. Long ⁴ & Kornelia Polyak ^{1,2,3,4,5} ✉

Basal breast cancer is a subtype with a poor prognosis in need of more effective therapeutic approaches. Here we describe a unique role for the KDM4C histone lysine demethylase in *KDM4C*-amplified basal breast cancers, where KDM4C inhibition reshapes chromatin and transcriptomic landscapes without substantial alterations of its canonical substrates, trimethylated histone H3 lysine 9 (H3K9me3) and lysine 36 (H3K36me3). Rather, KDM4C loss causes proteolytic cleavage of histone H3 mediated by cathepsin L (CTSL), resulting in decreased glutamate–cysteine ligase expression and increased reactive oxygen species. CTSL is recruited to the chromatin by the grainyhead-like 2 (GRHL2) transcription factor that is methylated at lysine 453 following KDM4C inhibition, triggering CTSL histone clipping activity. Deletion of CTSL rescued KDM4-loss-mediated tumor suppression. Our study reveals a function for KDM4C that connects cellular redox regulation and chromatin remodeling.

Breast cancer is a heterogeneous disease classified into luminal, human epidermal growth factor receptor 2-positive (HER2⁺) and basal molecular subtypes¹. Clinical classification is based on the expression of estrogen (ER), progesterone (PR) and HER2 receptors, distinguishing ER⁺, HER2⁺ and triple-negative (ER–PR–HER2[−]) disease. Triple-negative breast cancer (TNBC) is commonly associated with therapeutic resistance and high risk of distant metastasis, leading to shorter patient survival compared to other subtypes². TNBC is also highly heterogeneous and is further divided into luminal, basal and mesenchymal subtypes

with different mutational and therapeutic sensitivity^{2–4}. Most basal breast cancers are TNBC, but there is also an *ERBB2*-amplified basal subtype.

Epigenetic regulators are key determinants of cellular states, and thus, epigenetic mutations are a major source of intratumor heterogeneity^{5,6}. Post-translational histone modifications shape chromatin states and transcriptomes during normal development and in many diseases, including cancer^{7,8}. Frequent somatic mutations in genes encoding histone modifiers like histone demethylases (HDMs)

in human cancers underscore their roles in tumorigenesis^{9,10} and highlight them as emerging therapeutic targets in multiple human cancer types.

We and others previously described that *KDM4C*, which encodes a trimethylated histone H3 lysine 9 (H3K9me3) and lysine 36 (H3K36me3) demethylase¹¹, is amplified in a subset of TNBC^{12,13}. *KDM4C* has key roles in development and differentiation. In embryonic stem cells (ESCs), it is a target of the OCT4 transcription factor and is required for ESCs self-renewal and the generation of induced pluripotent stem cells^{14,15}. The role of *KDM4C* in tumorigenesis is less well understood, although it is one of the few genes with germline variants associated with a multi-cancer phenotype^{16,17}. In glioblastoma, *KDM4C* regulates the p53-MYC nexus¹⁸, while in MLL fusion-driven acute myeloid leukemia, it facilitates epigenetic remodeling by the PRMT1 methyltransferase¹⁹. In TNBC, *KDM4C* has been implicated in genomic instability via its effects on chromosome segregation^{20,21}. However, the mechanisms by which *KDM4C* promotes breast tumorigenesis have not been delineated.

Here we report integrated multi-omic characterization of genetic or pharmacological blockade of *KDM4C* in *KDM4C*-amplified and non-amplified basal breast cancer models. We uncovered an unexpected function for *KDM4C* as a regulator of cathepsin L (CTSL)-mediated histone H3 N-terminal tail clipping in *KDM4C*-amplified tumors via modulating methylation of the grainyhead-like 2 (GRHL2) transcription factor.

Results

KDM4C is amplified in breast cancer and drives tumor growth

KDM4C is one of the most frequently mutated genes encoding HDMs in TNBC in The Cancer Genome Atlas (TCGA)²² and Molecular Taxonomy of Breast Cancer International Consortium (METABRIC)²³ cohorts (Extended Data Fig. 1a). Within TNBC, *KDM4C* amplification is associated with the basal TNBC subtype, and *KDM4C*-amplified cell lines are also more commonly basal or triple-negative (Extended Data Fig. 1b–e). *KDM4C* amplification correlates with mRNA and protein levels in patient-derived xenograft (PDX) models, primary TNBC tumors and cell lines (Extended Data Fig. 1f–l). Based on these analyses, we selected four *KDM4C*-amplified basal breast cancer cell lines (SUM149, HCC1954, HCC38 and HCC70) and four *KDM4C*-non-amplified lines (HCC1806, HDQP1, HCC1143 and HCC1569) to assess the functional relevance of *KDM4C* in basal breast cancer (Extended Data Fig. 2a,b).

We first downregulated *KDM4C* using lentiviral doxycycline (Dox)-inducible shRNAs in five cell lines (three amplified versus two non-amplified) and confirmed effective knockdown by immunoblot analysis (Extended Data Fig. 2c). *KDM4C* downregulation substantially decreased tumor cell growth in vitro and in vivo in all *KDM4C*-amplified cell lines and in a non-amplified cell line (HCC1806) with moderate *KDM4C* expression (Extended Data Fig. 2c–g). We found that sh*KDM4C* expression had no measurable effects in HDQP1 cells, likely due to negligible endogenous *KDM4C* levels (Extended Data Fig. 2b). Similarly, treatment with small-molecule inhibitors of the KDM4 family of enzymes, ML324 (ref. 24) and QC6352 (ref. 25), substantially decreased cell viability in a large panel of cell lines, with QC6352 showing greater selectivity and potency (Extended Data Fig. 3a,b). A PRISM compound screen²⁶, including 32 breast cancer cell lines, demonstrated higher sensitivity to QC6352 in basal than in luminal lines (Extended Data Fig. 3c and Supplementary Table 1). ML324 also substantially decreased SUM149 xenograft growth, with a similar trend observed in HCC1954 xenografts (Extended Data Fig. 3d). Both ML324 and QC6352 impaired the growth of a *KDM4C*-amplified TNBC PDX (HCI-041)^{27,28} (Extended Data Fig. 3e).

KDM4C-loss-induced growth inhibition was dependent on its HDM activity because it was rescued by exogenous expression of wild type (WT) but not a catalytically inactive-mutant (S198M) *KDM4C* in SUM149 cells^{29,30} (Extended Data Fig. 3f–h). Downregulation of two other KDM4 family members, *KDM4A* or *KDM4B*, did not affect the

growth of the cell line tested (Extended Data Fig. 3i–k), confirming the specific requirement for *KDM4C* in basal breast cancer.

Overall, our data in clinical samples and experimental models suggest an oncogenic role for *KDM4C* in a subset of basal breast tumors.

KDM4C-blockade-induced transcriptomic and chromatin changes

To investigate mechanisms underlying *KDM4C*-loss-mediated growth inhibition, we first performed RNA sequencing (RNA-seq) in four Dox-inducible sh*KDM4C*-expressing basal breast cancer cell lines, including *KDM4C*-amplified (HCC1954 and SUM149) and *KDM4C*-non-amplified (HCC1806 and HDQP1) cells. Analysis of the RNA-seq confirmed efficient downregulation of *KDM4C* (Extended Data Fig. 3l and Supplementary Table 2), and more substantial and tightly correlated transcriptional changes were found in *KDM4C*-amplified compared to non-amplified cell lines (Fig. 1a,b, Extended Data Fig. 3m and Supplementary Table 2). Functional annotation by gene set variation analysis (GSVA) with Hallmark signature collections revealed that *KDM4C* genetic depletion or pharmacological inhibition resulted in consistent repression of multiple major metabolic pathways (for example, cholesterol homeostasis and oxidative phosphorylation) uniquely in *KDM4C*-amplified basal cell lines except for QC6352 treatment in HDQP1 cells (Fig. 1c). In line with this observation, cholesterol homeostasis and oxidative phosphorylation were among the top differentially enriched pathways between *KDM4C*-amplified and *KDM4C*-non-amplified TNBCs in the TCGA cohort together with key regulators of cell proliferation (for example, MYC targets; Fig. 1d). We also observed activated transforming growth factor β (TGF- β) signaling and epithelial-to-mesenchymal transition (EMT) in all four cell lines tested, indicating a shift in cell states.

We also generated ML324-resistant derivatives of HCC1954 and SUM149 cell lines (HCC1954-MLR and SUM149-MLR) by prolonged culture with ML324 (10 μ m) to help delineate mechanisms of response and acquired resistance to *KDM4* inhibitors (Extended Data Fig. 3n,o). RNA-seq of MLR lines revealed transcriptional patterns similar to those of ML324-treated parental cells but also identified resistance-specific changes (Extended Data Fig. 3p). Only a few pathways were commonly altered between the two MLR lines, but TGF- β signaling and cholesterol homeostasis were among the top upregulated and downregulated pathways, respectively, highlighting their importance in *KDM4C*-driven tumors (Extended Data Fig. 3q).

Next, we performed chromatin immunoprecipitation followed by sequencing (ChIP-seq) for *KDM4C* in four *KDM4C*-amplified basal (HCC1954, SUM149, HCC70 and HCC2157) and two non-amplified ER⁺ luminal (T47D and MCF7) cell lines and found strong cell-type specificity of *KDM4C* chromatin peaks but similar distributions at promoter and non-promoter loci (Extended Data Fig. 4a,b). Integrating *KDM4C* binding and histone modification patterns demonstrated mutual exclusivity of *KDM4C* with its substrates H3K9me3 and H3K36me3 in most cell lines, except H3K36me3 in T47D, and substantial co-occurrence with H3K4me3 and H3K27ac peaks in all four lines (Extended Data Fig. 4c,d). We also assessed global differences in H3K9me3 and H3K36me3 signal intensity after *KDM4C* blockade, but neither sh*KDM4C* nor ML324 treatment caused substantial changes in the two *KDM4C*-amplified basal cell lines except for H3K36me3 in ML324-treated SUM149 cells (Fig. 1e and Extended Data Fig. 4e). In contrast, pronounced differences in H3K9me3 and H3K36me3 were observed following *KDM4C* downregulation in HCC1806 cells, a *KDM4C*-non-amplified cell line with moderate *KDM4C* expression (Fig. 1e). The differences between ML324 treatment and shRNA knockdown could potentially be explained by the inhibition of other KDM4 family members by ML324. Thus, we also performed ChIP-seq for *KDM4A* and *KDM4B* and found distinct overlap in genomic binding sites among all three KDM4 enzymes, and *KDM4A*-binding sites were associated with the elevated H3K36me3 levels after ML324 treatment (Extended Data Fig. 4f,g).

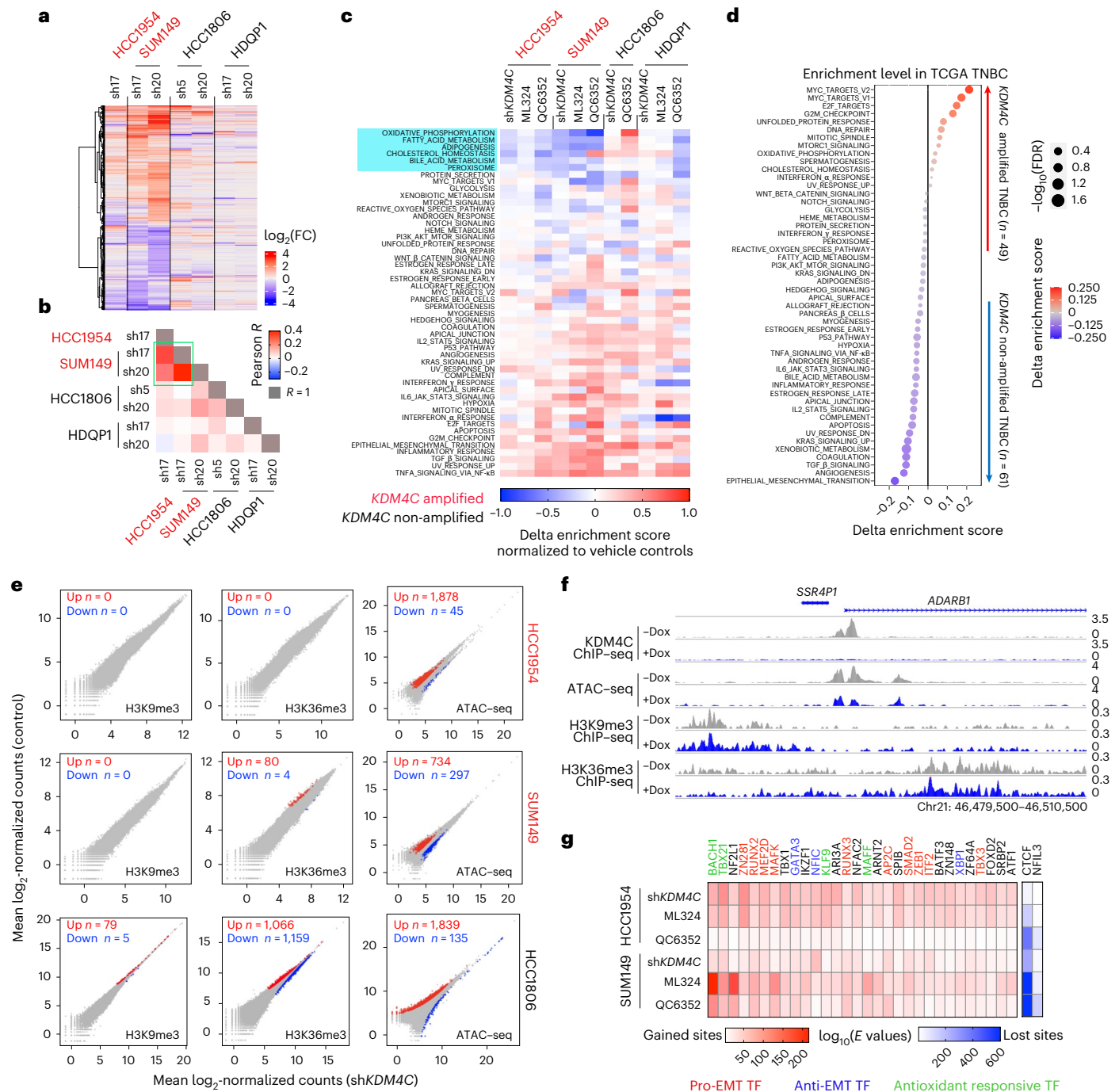


Fig. 1 | KDM4C inhibition-induced transcriptomic and chromatin remodeling. **a**, Heatmap showing the $\log_2(\text{FC})$ of the union of all DEGs between vehicle versus shKDM4C merged from all the indicated Dox-inducible shKDM4C cell models. Gene expression FCs were normalized to each hairpin control. **b**, Heatmap illustrating the Pearson correlation R value of $\log_2(\text{FC})$ of all DEGs from each pairwise comparison. Correlations among KDM4C-amplified basal cell lines are highlighted in a green rectangle. **c**, Heatmap depicting alterations of the 50 Hallmark gene signature enrichment scores induced by downregulation of KDM4C and KDM4 inhibitor treatments. Delta enrichment scores were calculated by subtracting the scores of control groups from each treatment condition. Pathways were ranked from the most decreased to the most increased upon KDM4C inhibition. Metabolic pathways commonly repressed in KDM4C-amplified lines are highlighted by light blue rectangle. **d**, Dot plot showing the 50 Hallmark gene signature enrichment score differences between TNBCs

with ($n = 49$) or without ($n = 61$) KDM4C copy number gain in the TCGA cohort. Delta enrichment scores were calculated by subtracting the mean values of KDM4C-non-amplified group from KDM4C-amplified group. e, Scatter plots representing the \log_2 -normalized counts of H3K9me3 and H3K36me3 ChIP-seq (5 kb bin) and merged ATAC-seq peaks between control and shKDM4C groups in all 3 cell lines. Numbers of differential regions and directionality (up or down) are indicated on each plot. f, Genomic track view of KDM4C, ATAC-seq, H3K36me3 and H3K9me3 signals at the ADARB1 gene locus in SUM149 cells with or without KDM4C knockdown. Chr21, chromosome 21. g, Heatmap showing the top 30 and 2 consistently and uniquely enriched motifs in gained and lost ATAC sites, respectively, normalized to vehicle groups in the indicated cell lines. $\log_{10}(E \text{ values})$ represent the significance of enrichment. Motifs of transcription factors associated with EMT (pro-EMT or anti-EMT) or antioxidant response are highlighted with different colors. TF, transcriptional factor.

Assay for transposase-accessible chromatin using sequencing (ATAC-seq) showed extensive remodeling of accessible chromatin after KDM4C suppression in all three cell lines, albeit to a variable degree. There was a predominant gain in open chromatin in HCC1954 and HCC1806 cells, while SUM149 cells showed a less pronounced increase (Fig. 1e). Chromatin changes in *KDM4C*-amplified cells were not associated with changes in H3K9me3 or H3K36me3 signal intensity, as exemplified by the *ADARBI* genomic locus (Fig. 1f). Moreover, transcription factor motifs enriched in top gained ATAC sites were related to EMT (for example, ZEB1 and SMAD2) and antioxidant pathways (for example, BACH1 and NF2L1), while CTCF and NFIL3 were the only motifs enriched in lost ATAC sites (Fig. 1g).

We also analyzed changes in H3K4me3 signal following KDM4C inhibition due to the prominent overlap detected between KDM4C and H3K4me3 peaks (Extended Data Fig. 4c,d), which has also been reported in ESCs³¹. Downregulation or inhibition of KDM4C led to substantial gains (22.1% in HCC1954 and 22.8% in SUM149) and losses (12.9% in HCC1954 and 27% in SUM149) in H3K4me3 peaks, although most peaks were still detected in all conditions (Extended Data Fig. 4h). Alterations in H3K4me3 peaks were substantially associated with transcriptomic changes except in ML324-treated HCC1954 cells (Extended Data Fig. 4i). A prior study showed that KDM4C is mainly recruited to H3K4me3 marks via its tandem tudor domain (TTD)³². To test if the TTD domain is required for KDM4C knockdown-induced cell growth suppression, we downregulated endogenous KDM4C and exogenously expressed WT KDM4C or a mutant lacking the TTD domain (Δ TTD) in SUM149 cells (Extended Data Fig. 4j). We found that only the WT KDM4C was able to partially rescue the growth inhibitory phenotype (Extended Data Fig. 4k,l), suggesting that the KDM4C–H3K4me3 interaction may be required for this function.

Overall, these data showed that in *KDM4C*-amplified lines, KDM4C blockade induced substantial changes in chromatin patterns with limited changes in its canonical substrates H3K9me3 and H3K36me3.

KDM4C inhibition induces proteolytic cleavage of histone H3

Due to the discrepancy between extensive global accessible chromatin remodeling and limited H3K9me3 and H3K36me3 alterations following KDM4C inhibition, we investigated global changes in histone modification patterns in a comprehensive and unbiased manner using histone mass spectrometry (MS). Surprisingly, we detected the loss of nearly all histone marks corresponding to the N-terminal parts of histones H3 and H4 following ML324 treatment in SUM149 and HCC1954 cells, with *KDM4C* knockdown also exhibiting a similar but weaker trend (Fig. 2a). Generally, a decrease in the levels of some histone marks is compensated by an increase in others. Thus, the concomitant loss of most N-terminal marks could potentially be explained by a proteolytic cleavage event that removed the N terminus of these histones. To investigate this hypothesis, we performed an unbiased proteomic analysis of the extracted histones and found peptides consistent with non-canonical cleavage events at H3A21 and H4K16 (Fig. 2b). We quantified the non-canonical TKAAR peptide from H3 and discerned a general induction of clipped H3 peptides following KDM4C blockade in HCC1954 and SUM149 cells with limited changes in T47D cells (Fig. 2c). Immunoblot analysis using a C-terminal H3 antibody confirmed the increase in N-terminal tail clipping after *KDM4C* knockdown or blockade specifically in the four *KDM4C*-amplified cell lines, while the N-terminal H3 antibody did not detect noticeable differences, likely due to the rapid degradation of the cleaved peptide (Fig. 2d and Extended Data Fig. 5a). Downregulation of KDM4A or KDM4B did not induce histone tail clipping (Extended Data Fig. 5b), and KDM4C-induced clipping was prevented by ectopic overexpression of WT but not catalytically inactive-mutant KDM4C^{S198M} (Extended Data Fig. 5c), indicating that it is specific to KDM4C and requires its demethylase function. Histone MS of ML324-resistant derivatives demonstrated higher baseline H3 clipping in HCC1954-MLR cells that was not further increased by ML324,

whereas limited baseline and higher ML324-induced H3 clipping was observed in SUM149-MLR cells (Extended Data Fig. 5d,e). We also noticed a strong increase in H3Ser10 phospho-peptide in SUM149-MLR cells, which was confirmed by immunoblot (Extended Data Fig. 5f). However, SUM149-MLR cells did not show differential sensitivity toward inhibitors of H3Ser10 kinases (AURKA/AURKB and CDK8; Extended Data Fig. 5g), suggesting a lack of functional relevance.

To identify the endopeptidase that mediates KDM4C-loss-induced histone H3 and H4 tail clipping, we repeated the MS analyses in the presence of various protease inhibitors. Quantification of histone H3 total and cleaved peptides, as well as immunoblot validation, revealed that inhibition of CTSL (by CTSLi-III and SID2668150) or cysteine protease inhibitor E64d, but not serine or aspartyl proteases, reduced histone clipping (Fig. 2e–g and Extended Data Fig. 5h), identifying CTSL as the strongest candidate responsible for H3 clipping. In contrast, loss of H4 peptide was partially rescued only by aspartyl protease inhibitor pepstatin A (Extended Data Fig. 5i), suggesting different mechanisms for histone H3 and H4 proteolysis. CTSL has previously been reported to cleave H3 in mouse ESCs at exactly the same amino acid position (H3A21) as we observed^{33,34}. Further investigation revealed increased cellular CTSL activity following KDM4C blockade or downregulation only in the *KDM4C*-amplified cell lines (Fig. 2h,i, Extended Data Fig. 5j and Supplementary Fig. 1), strengthening the link between histone H3 clipping and CTSL activity. The increase in CTSL activity after KDM4 inhibition was more pronounced in SUM149 and HCC1954 cells, likely due to higher baseline CTSL expression (Extended Data Fig. 5k), which was specific to KDM4C because it was not observed following knockdown of KDM4A or KDM4B (Extended Data Fig. 5l,m). Ectopic expression of WT but not catalytically inactive KDM4C mutant diminished CTSL activation (Extended Data Fig. 5n,o), indicating the requirement for demethylase function.

To prove a role for CTSL in KDM4C-blockade-induced histone clipping, we deleted *CTSL* in five basal breast cancer cell lines (three *KDM4C*-amplified and two non-amplified) using CRISPR–Cas9 (Extended Data Fig. 6a). CTSL immunofluorescence and immunoblot using fractionated cell lysates demonstrated nuclear localization in parental cell lines, but a lack of nuclear signal in *CTSL* knockout (*CTSL*^{KO}) lines (Extended Data Fig. 6b,c). The subcellular localization of CTSL and its maturation were not affected by KDM4C blockade (Extended Data Fig. 6d,e), suggesting that KDM4C-loss-induced histone cleavage is not due to lysosomal rupture-induced translocation of CTSL to the nucleus, as has been reported for external stressors such as viral infection³⁵. Immunoblot analyses using antibodies against the C terminus of H3 revealed a decrease in KDM4 inhibition-induced H3 clipping in *CTSL*^{KO} lines in all three *KDM4C*-amplified cell lines (Fig. 3a and Extended Data Fig. 6f).

Overall, these results established a link between KDM4C demethylase activity and chromatin remodeling via CTSL-mediated histone H3 cleavage in *KDM4C*-amplified cell lines.

Nuclear CTSL is activated by KDM4C inhibition

To confirm the localization of CTSL to the chromatin, we performed CTSL ChIP-seq in SUM149 cells that showed the most pronounced H3 clipping. We detected sharp CTSL peaks resembling transcription factor binding and marked changes after ML324 treatment (Fig. 3b,c). CTSL peaks lost after ML324 treatment (effective CTSL sites) were associated with ML324-induced differentially expressed genes (DEGs) and decreased chromatin accessibility (Fig. 3d,e), whereas gained peaks showed limited association with transcriptional changes (Extended Data Fig. 6g). CTSL peak intensity was not changed in SUM149-MLR cells after ML324 treatment, suggesting that acquired resistance to ML324 is associated with diminished histone H3 tail clipping (Extended Data Fig. 6h). CTSL peaks lost after ML324 treatment substantially overlapped with KDM4C binding sites compared to unchanged peaks (Fig. 3c), highlighting the importance of CTSL loss in ML324-induced chromatin remodeling and the involvement of KDM4C in this process.

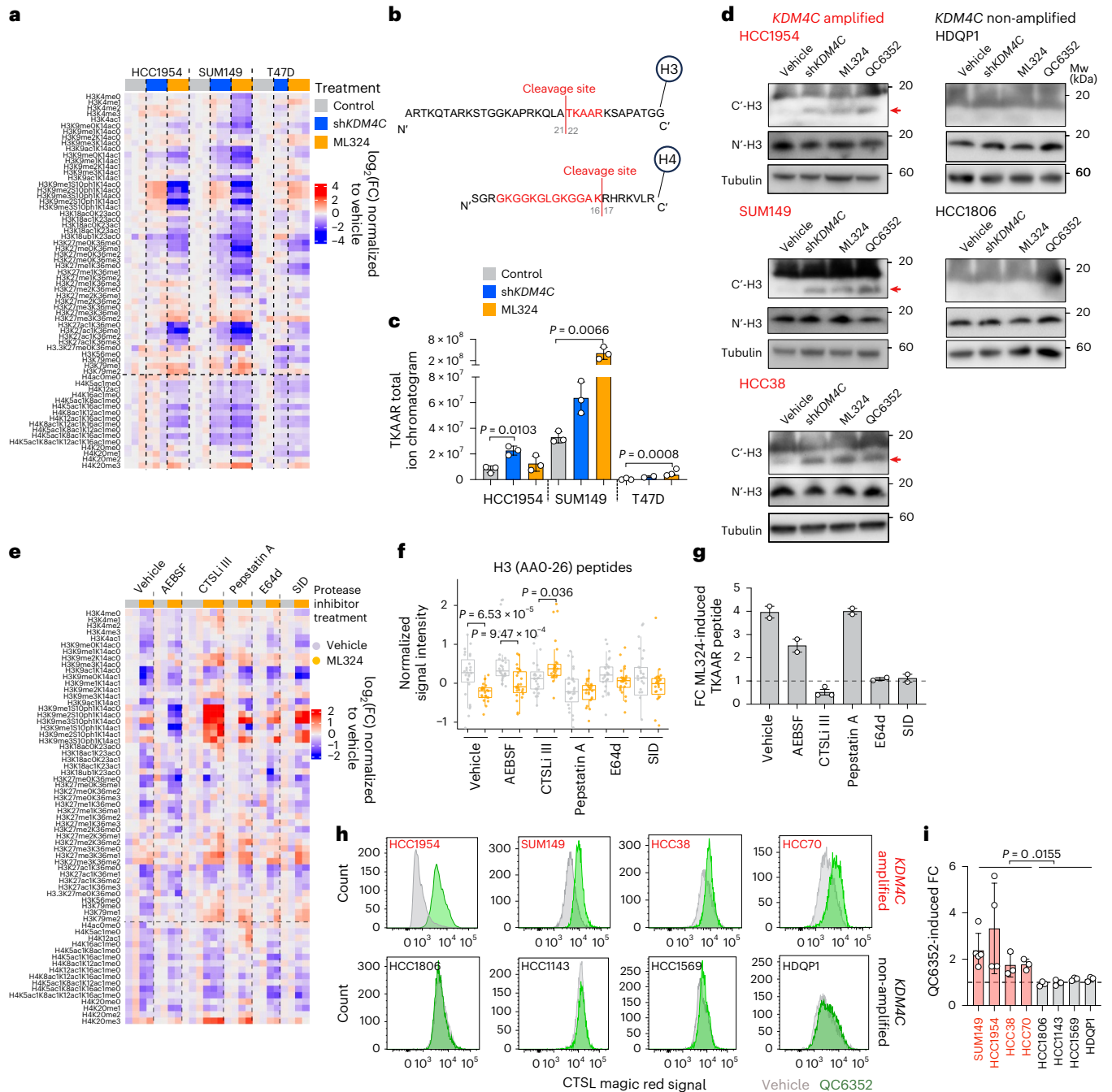


Fig. 2 | KDM4C inhibition induces proteolytic cleavage of histone tails.

a, Heatmap showing histone peptide abundance by MS in the indicated cell lines expressing Dox-inducible sh*KDM4C* following control (no Dox, dimethyl sulfoxide (DMSO)), sh*KDM4C* induction (1 μg ml⁻¹ Dox, DMSO) or 10 μM ML324 (no Dox) treatment. Peptide abundances were normalized to the mean values of vehicle group within each cell line and ranked from N to C terminus. **b**, Schematic illustration of proteolytic cleavage sites in histones H3 and H4 after *KDM4C* blockade. **c**, Bar plot showing the clipped H3 peptide (TKAAR) total ion chromatogram signal intensity in the indicated groups. Mean ± s.d. are shown. Two-sided Dunnett’s test was used within each cell line for groups with biological triplicates, except T47D sh*KDM4C* group. **d**, Immunoblot for histone H3 using C (C’-H3) and N (N’-H3) terminal antibodies in 5 cell lines with inducible sh*KDM4C* infection, following control (DMSO, no Dox), 1 μg ml⁻¹ Dox (sh*KDM4C*), 10 μM ML324 (no Dox) or 1 μM QC6352 (no Dox) for 5 days. Tubulin was used as a loading control. Clipped H3 bands are marked with red arrow. Experiments were repeated independently three times (HCC1954, SUM149 and HCC38) or twice (HDQP1 and HCC1806) with similar results. **e**, Heatmap showing histone peptide abundance by MS in SUM149 cell line following DMSO (vehicle) or 10 μM ML324 treatment in the presence or absence of the indicated protease inhibitors (100 μM AEBSF HCl,

100 μM pepstatin A, 10 μM SID2668150, 10 μM E64d and 5 μM CTSLi-III) for 24 h. Peptide abundances were normalized to the mean values of vehicle group within each cell line and ranked from N to C terminus. **f**, Box plots depicting differences in N-terminal histone H3 (amino acid positions 0–26) peptide abundances between vehicle and *KDM4C*-inhibited samples following the indicated protease treatment in the SUM149 cell line. Box plots span the upper quartile (upper limit), median (center) and lower quartile (lower limit). Whiskers extend a maximum of 1.5 × IQR. Statistical significance of differences was determined by two-sided Kruskal–Wallis test. **g**, Bar plot showing the ML324-induced FC of clipped H3 peptide (TKAAR) total ion chromatogram signal intensity in the indicated groups. Mean ± s.d. are shown for each group with *n* = 3 (CTSLi-III group) and *n* = 2 (all the rest) biological replicates. **h**, Representative flow cytometry plots depicting the shift of CTSL magic red signal after 1 μM QC6352 treatment for 5 days. **i**, Bar plot summarizing the QC6352-induced FCs in CTSL activity merging from *n* = 5 (SUM149), *n* = 4 (HCC1954) and *n* = 3 (other cell lines) independent experiments in each cell line (mean ± s.d.). Two-sided Mann–Whitney *U* test was used to compare average FCs between four *KDM4C*-amplified and four non-amplified cell lines. SID, SID2668150; AEBSF, 4-(2-aminoethyl)benzenesulfonyl fluoride hydrochloride.

To further substantiate N-terminal H3 clipping following KDM4C inhibition and to eliminate the possibility of an unknown N-terminal H3 modification blocking antibody binding, we expressed N-terminal GFP or V5-tagged H3 in SUM149 cells (Extended Data Fig. 6i) and performed ChIP-seq using antibodies against GFP or V5 as well as the C terminus of H3. We detected a more pronounced decrease in overall H3 ChIP-seq signal using GFP or V5 antibodies than C-terminal H3 antibody following ML324 treatment at CTSL binding sites, which was not observed at randomly selected peaks (Fig. 3f–h). The alterations were more pronounced in the V5-tagged than in the GFP-tagged H3 model, potentially due to the steric hindrance associated with the larger GFP tag.

We also performed CTSL Hi-C and ChIP-seq (Hi-ChIP)³⁶ in SUM149 cells to assess ML324-induced global changes in chromatin organization mediated by CTSL. We identified 2,954 and 4,992 differential intrachromosomal and interchromosomal interaction regions induced by ML324 (Extended Data Fig. 6j,k), which overlapped with the majority (74%) of differential CTSL ChIP-seq peaks (Extended Data Fig. 6l), implying that these higher chromatin conformational changes were outcomes of CTSL acting *in cis*.

These data establish that KDM4C-inhibition-induced H3 tail clipping occurs at CTSL peaks that are lost after KDM4C inhibition and results in transcriptional reprogramming via changes in chromatin accessibility and conformation.

GRHL2 mediates CTSL chromatin binding and activity

Next, we investigated how CTSL is recruited to the chromatin because it does not have a known DNA-binding domain. We first performed rapid immunoprecipitation MS (RIME)³⁷ for KDM4C in control and ML324-treated cells but did not detect any CTSL peptides, suggesting that KDM4C may not directly bind CTSL or it is not detectable by this technique (Supplementary Table 3). To analyze CTSL-associated proteins in an unbiased manner, we performed MS of immunoprecipitated CTSL in SUM149 cells at baseline (Dox-inducible *shKDM4C* #17 and #20 lines without Dox induction). CTSL itself and known CTSL-interacting proteins, including CTS3 and CTSB cysteine protease inhibitors, were among the most abundant peptides consistently enriched in CTSL immunoprecipitants compared to IgG controls (Fig. 4a, Extended Data Fig. 7a and Supplementary Table 4). We detected very few previously uncharacterized CTSL binding proteins, including the GRHL2 transcription factor and DEAD-Box helicase 23. Downregulation of KDM4C did not alter the interaction of CTSL with any of these proteins (Extended Data Fig. 7a and Supplementary Table 4). Intriguingly, GRHL2 was also the top predicted transcription factor motif enriched in CTSL peaks in HCC1954 and SUM149 cells (Fig. 4b).

We confirmed the association of GRHL2, CTSL and KDM4C in the nucleus by co-immunoprecipitation experiments for each of

the three proteins (Fig. 4c) and by multicolor immunofluorescence analyses (Extended Data Fig. 7b). Notably, deletion of GRHL2 in SUM149 cells using CRISPR-Cas9 led to the loss of CTSL in KDM4C immunoprecipitants (Extended Data Fig. 7c,d), and deletion of CTSL led to the loss of GRHL2 and KDM4C in CTSL immunoprecipitants (Extended Data Fig. 7e), excluding the possibility that the observed results are due to the cross-reactivity of CTSL antibody with GRHL2 or KDM4C.

To verify the colocalization of CTSL and GRHL2 on the chromatin, we performed GRHL2 ChIP-seq and found that nearly all CTSL binding sites overlapped with GRHL2 peaks in both HCC1954 and SUM149 cell lines (Fig. 4d). Furthermore, *GRHL2*KO in SUM149 cells led to the nearly complete loss of CTSL chromatin binding (Fig. 4e and Extended Data Fig. 7f). Deletion of GRHL2 also diminished KDM4C-inhibition-induced histone H3 cleavage, again confirming the role of nuclear CTSL in this process (Extended Data Fig. 7g). GRHL2 peak signal was not markedly affected by ML324 treatment at CTSL sites lost after ML324 treatment, confirming direct GRHL2 chromatin binding independent of CTSL (Extended Data Fig. 7h). We also analyzed overlap in binding between KDM4C and GRHL2 peaks and CTSL sites lost after ML324 treatment. Although 38% of ML324-induced lost CTSL peaks (effective CTSL sites) overlapped with both GRHL2 and KDM4C (triple overlap), the CTSL peak intensity was substantially lower in these regions compared to only CTSL-GRHL2 overlapping peaks (Fig. 4f), implying that the GRHL2-CTSL complex may have KDM4C-independent functions. Both triple (KDM4C/GRHL2/CTSL) and double (GRHL2/CTSL) overlapping peaks were substantially associated with repression in gene expression after KDM4C blockade (Fig. 4g), and the DEGs and enriched pathways showed considerable overlap (Extended Data Fig. 7i,j). Thus, KDM4C inhibition may alter gene expression via CTSL-mediated histone cleavage through GRHL2 recruitment in both a direct and indirect manner.

Next, we explored potential mechanisms by which KDM4C inhibition induces CTSL-dependent histone H3 cleavage. We hypothesized that either GRHL2 or CTSL is a non-histone substrate of KDM4C and KDM4C inhibition leads to its increased methylation, which then triggers CTSL-mediated histone H3 clipping. To test this hypothesis, we first performed immunoprecipitation using a pan-lysine methylation antibody, followed by immunoblot for GRHL2 or CTSL after KDM4C knockdown or inhibition. Cells were grown in complete medium or lacking methionine to decrease the levels of intracellular S-adenosyl methionine (SAM), a cofactor required for protein methylation. We detected GRHL2 in pan-lysine methyl antibody immunoprecipitants after KDM4C blockade and only in *KDM4C*-amplified cells growing in complete medium (Fig. 4h and Extended Data Fig. 7k,l). To identify the specific methylation sites in GRHL2, we performed MS on in-gel

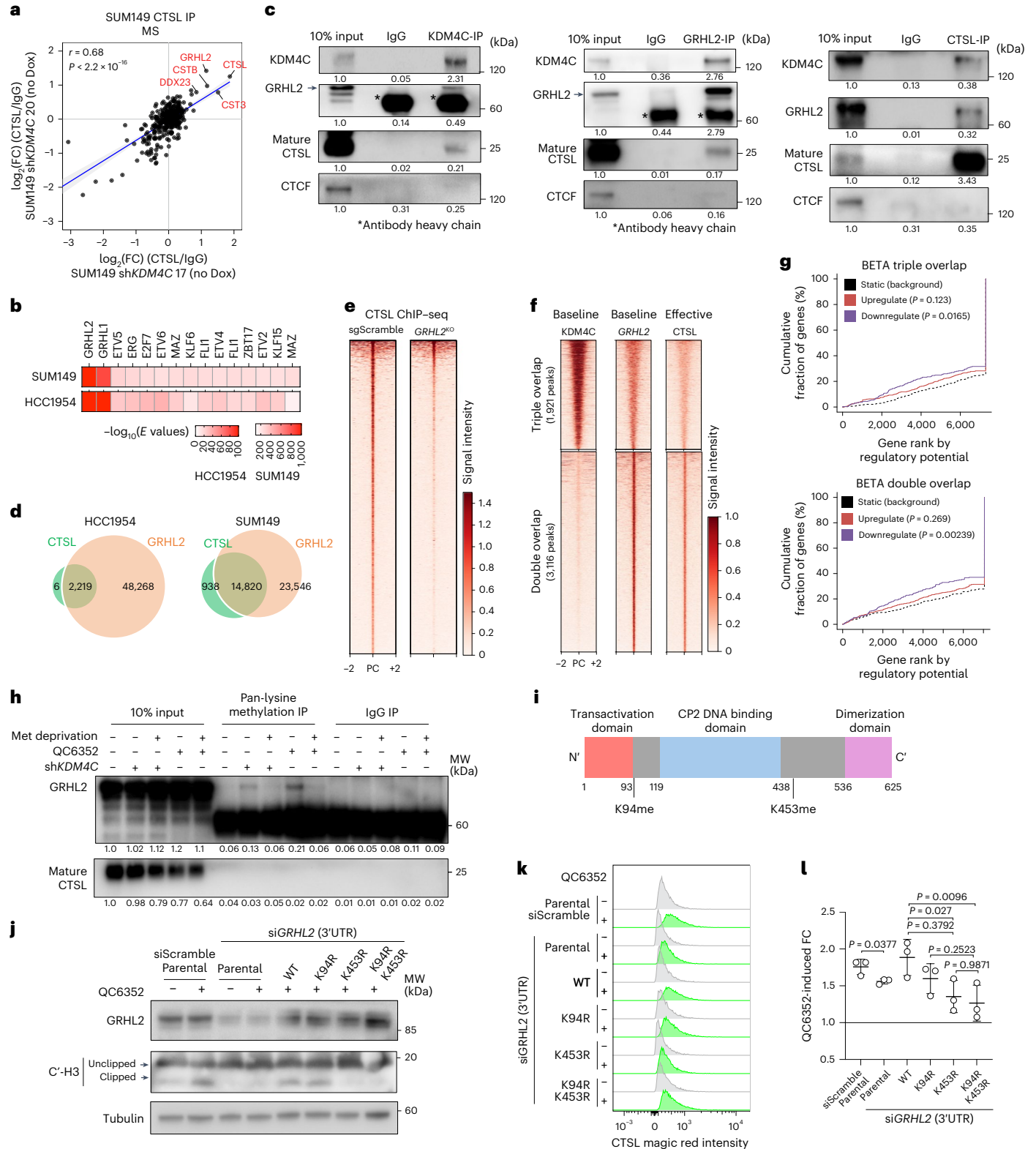
Fig. 4 | GRHL2 recruits CTSL to the chromatin, and its methylation modulates CTSL activity.

a, Scatter plot showing the correlation of $\log_2(\text{FC})$ (normalized to IgG control) MS signal of proteins detected in CTSL immunoprecipitants in SUM149 cell models *shKDM4C* #17 and *shKDM4C* #20 at baseline without Dox treatment. The linear regression line with 95% confidence interval is shown. *P* values were derived from two-sided Pearson correlation. **b**, Heatmap depicting rank order of transcription factor binding site motifs enriched in CTSL binding sites of vehicle-treated cells in SUM149 and HCC1954 cell lines. $\log_{10}(E$ values) were used to define the significance of enrichment. **c**, Immunoblot analysis of KDM4C, GRHL2 and CTSL immunoprecipitants and 10% of input detected with the indicated antibodies in SUM149 cells. CTCF was used as negative control. Signal intensity normalized to input is indicated for each protein. All experiments were repeated at least twice independently with similar results. **d**, Venn diagrams showing intersections of CTSL and GRHL2 binding sites in HCC1954 and SUM149 cells. **e**, Heatmap showing overall intensities of CTSL chromatin binding in scramble control and *GRHL2* KO SUM149 cell line. Signal intensity is illustrated in a 4 kb window (PC). **f**, Heatmaps illustrating triple (CTSL*GRHL2*KDM4C*) and double (CTSL*GRHL2*) overlapping peaks in SUM149 cell lines. Signal

intensity is depicted in a 4 kb window. **g**, Line plot showing BETA for assessing the association of triple and double overlapping peaks with differentially expressed genes in SUM149 following ML324 treatment. One-sided Kolmogorov-Smirnov test was applied to calculate the *P* values. **h**, Immunoblot for GRHL2 and CTSL in 10% input and immunoprecipitants of pan-lysine methylation and IgG antibody from cells with the indicated treatments. GRHL2 and CTSL signal normalized to input is indicated for each condition. The experiment was repeated three times independently with similar results. **i**, Schematic view of GRHL2 protein structure indicating the location of the lysine methylation sites. **j**, Immunoblot for GRHL2 and C-terminal histone H3 following 3 days of treatment with vehicle or 1 μM QC6352 of SUM149 cells expressing WT or the indicated mutant GRHL2. This experiment was repeated twice independently with similar results. **k**, Representative flow cytometry plots depicting the shift of CTSL activity signal in SUM149 cells with the indicated conditions. **l**, Bar plot summarizing the QC6352-induced CTSL magic red FCs in SUM149 cell models merging three independent experiments (mean \pm s.d.). Two-sided ordinary one-way analysis of variance (ANOVA) test was used.

digested GRHL2 immunoprecipitants from QC6352-treated SUM149 cells. We identified two lysine monomethylated sites in GHRL2 at residues K94 and K453 (Fig. 4i and Extended Data Fig. 7m). To determine the functional relevance of these GRHL2 lysine methylation events, we exogenously expressed WT GRHL2 or its single or double lysine-to-arginine mutant variants (that is, K94R, K453R and K94R/K453R) that cannot be methylated³⁸, following the downregulation of endogenous GHRL2 using 3'UTR-targeting siRNAs (Extended Data

Fig. 7n). We found that endogenous GRHL2 knockdown diminished both KDM4C-inhibition-induced histone H3 clipping and CTSL activation, which could be rescued by exogenous expression of the WT GRHL2 or the GRHL2^{K94R} mutant (Fig. 4j–l). In contrast, expression of GRHL2^{K453R} or GRHL2^{K94R/K453R} double mutant was unable to rescue the GRHL2-loss phenotype (Fig. 4j–l). These data demonstrate that mono-methylation of GRHL2 at K453 is required for KDM4C-loss-induced CTSL activation and histone H3 clipping.



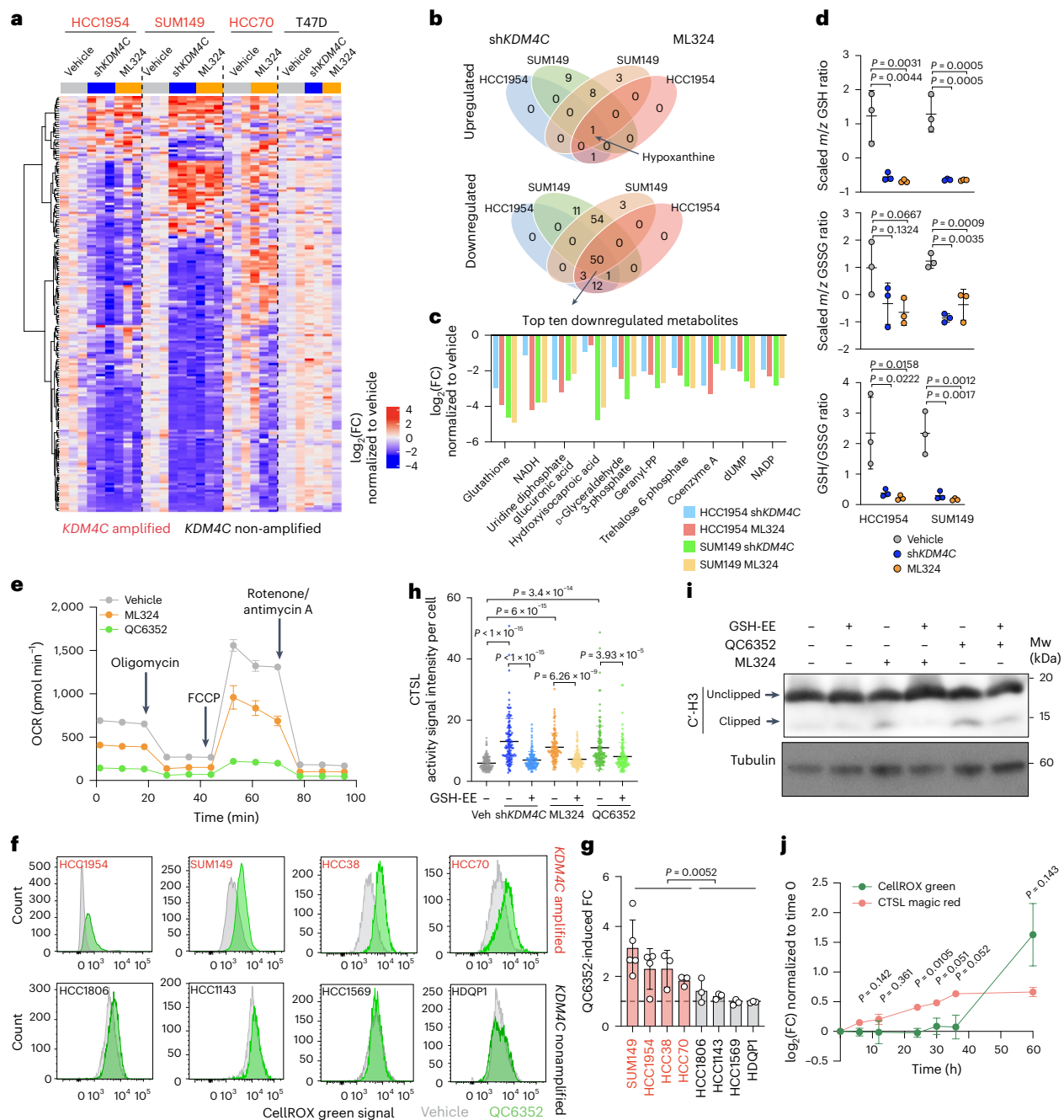


Fig. 5 | KDM4C blockade causes redox imbalance that activates CTSL.

a, Heatmap showing clustering of 248 polar metabolites in Dox-inducible shKDM4C-infected HCC1954, SUM149 and T47D cells following control (no Dox, DMSO), shKDM4C induction (1 $\mu\text{g ml}^{-1}$ Dox, DMSO) or 10 μM ML324 (no Dox) treatment and in HCC70 parental cells with or without 10 μM ML324 treatment. Metabolite abundances in each condition were normalized to the mean value of vehicle group of each cell line. **b**, Venn diagrams showing intersections of upregulated or downregulated metabolites in shKDM4C-expressing HCC1954 and SUM149 cells with either Dox (shKDM4C) or ML324 treatment. **c**, Bar plot representing the top ten consistently decreased metabolites in shKDM4C-expressing HCC1954 and SUM149 cells with either Dox or ML324 treatments. **d**, Dot plots depicting normalized reduced (GSH) and oxidized (GSSG) GSH levels and their ratios in HCC1954 and SUM149 cell lines with shKDM4C or ML324 treatment. Mean \pm s.d. from $n = 3$ is shown. Dunnett's test (two-sided) was used. **e**, Line plot depicting oxygen consumption rate (OCR) changes recorded by seahorse mito-stress assay in SUM149 cell lines treated with DMSO, 10 μM ML324 or 1 μM QC6352 for 3 days. Three time points were recorded for each state. This experiment was repeated three times independently with similar results. **f**, Representative flow cytometry plots

depicting the shift of CellROX green signal in 8 cell lines after 1 μM QC6352 for 5 days. **g**, Bar plot showing QC6352-induced FCs in CellROX green signal merging five (SUM149), four (HCC1954) and three (all the other cell lines) independent experiments of each cell line (mean \pm s.d.). Mann-Whitney U test was used to compare average FCs between four KDM4C-amplified and four non-amplified cell lines. **h**, Dot plot depicting quantification of CTSL activity signal quantified from 120 individual cells from 3 representative fluorescence images of inducible shKDM4C-expressing SUM149 cells treated with DMSO (vehicle), 1 $\mu\text{M ml}^{-1}$ Dox (shKDM4C), 10 μM ML324 or 1 μM QC6352 or combined with 2 mM GSH-EE for 5 days. Mean and s.d. are shown. Statistical significance of differences was determined by two-sided ordinary one-way ANOVA. **i**, Immunoblot analysis of histone H3 using antibodies for the C terminus in SUM149 cells treated with 1 μM of QC6352 in the presence or absence of 2 mM GSH-EE for 3 days. Tubulin was used as a loading control. Experiment was repeated three times independently with similar results. **j**, Line plot illustrating the QC6352-induced $\log_2(\text{FC})$ of CTSL magic red and CellROX green signals at the indicated time points in SUM149 cells. Data represent mean \pm s.d. merged from three independent experiments. Two-sided two-way ANOVA at each time point was used for statistical comparison.

Metabolic shift from KDM4C inhibition aids histone clipping

Our RNA-seq data identified multiple altered metabolic pathways upon KDM4C blockade (Fig. 1b), and the activity of both KDM4C and CTSL is regulated by metabolic factors. KDM4C is an oxygen- and α -ketoglutarate-dependent enzyme³⁹, while optimal CTSL activity is at pH 3.0–6.5 when thiol compounds are present⁴⁰. To test the hypothesis that CTSL-mediated histone clipping is also regulated by KDM4C-associated metabolic changes, we performed polar metabolite profiling in four cell lines (SUM149, HCC1954, HCC70 and T47D) and SUM149 and HCC1954 mouse xenografts with and without KDM4C blockade. Clustering of 248 metabolites showed widespread metabolic changes by KDM4C inhibition in the three *KDM4C*-amplified basal cell lines (Fig. 5a, Extended Data Fig. 8a and Supplementary Table 5) and xenografts (Extended Data Fig. 8b,c), whereas minimal differences were detected in the luminal ER⁺ *KDM4C*-non-amplified T47D cell line (Fig. 5a and Extended Data Fig. 8a). Intersection of upregulated metabolites in both HCC1954 and SUM149 cell lines and KDM4C-blockade treatment conditions revealed hypoxanthine as the single overlap (Fig. 5b), while 50 metabolites were commonly downregulated including reduced glutathione (GSH) as the top affected and other metabolites involved in GSH metabolism (Fig. 5c). Both reduced (GSH) and oxidized GSH (GSSG) and their ratio (GSH/GSSG) were decreased upon KDM4C blockade (Fig. 5d), suggesting an overall redox imbalance due to suppression of GSH biosynthesis pathway. Integration of metabolomic and transcriptomic changes also identified GSH metabolism as the top consistently downregulated pathway in both *KDM4C*-amplified cell lines and tumors along with glycolysis, gluconeogenesis and pentose phosphate pathways (Extended Data Fig. 8d). In line with this observation, KDM4C inhibition dampened general mitochondrial respiration (Fig. 5e), consistent with previous reports on outcomes of redox imbalance^{41,42}.

We confirmed a decrease in GSH and GSH/GSSG ratio following KDM4C downregulation or inhibition by luminescence assays in SUM149 cells (Extended Data Fig. 8e). A similar trend but higher variability was observed in metabolomic profiles in HCC1954 and SUM149 xenografts (Extended Data Fig. 8f). A substantial positive association was also observed between *KDM4C* mRNA and GSSG levels in 72 TNBC tumor samples from a recent multi-omic profiling study⁴³ validating the clinical relevance of our findings (Extended Data Fig. 8g). GSH showed a similar trend but no substantial association potentially due to high levels of reactive oxygen species (ROS) converting GSH to GSSG. Metabolomic profiling of HCC1954-MLR and SUM149-MLR resistant models depicted cell line-dependent differences, with HCC1954-MLR cells showing ML324-induced reduction in many metabolites even at

baseline level and no further changes after ML324, while SUM149-MLR cells showed higher baseline and ML324-induced differences (Extended Data Fig. 8h,i). ML324 did not affect GSH levels and GSH/GSSG ratios in MLR cells, indicating their potential role associated with resistance development, and HCC1954-MLR cells particularly have lower baseline GSH levels than parental cells (Extended Data Fig. 8j). These data imply that KDM4C may be a key modulator of redox balance in *KDM4C*-amplified basal breast cancer cell lines through the GSH pathway.

Next, we investigated the interplay between KDM4C-inhibition-induced reduction in GSH levels and CTSL-mediated histone H3 tail clipping. Similar to the pattern of histone cleavage and CTSL activation, KDM4C inhibition or downregulation induced a more pronounced elevation of ROS in *KDM4C*-amplified basal breast cancer cell lines (Fig. 5f,g and Extended Data Fig. 9a). Increased ROS activity following KDM4C blockade was rescued by overexpression of WT but not catalytically inactive-mutant KDM4C (Extended Data Fig. 9b). Elevation of ROS levels by direct stimulation of H₂O₂ or blockade of GSH biosynthesis by glutamate–cysteine ligase inhibitor buthionine sulfoximine (BSO) increased histone cleavage (Extended Data Fig. 9c) and CTSL activity (Extended Data Fig. 9d–g), and high ROS and active CTSL were detected in the same cells (Extended Data Fig. 9h). In contrast, neutralization of ROS by addition of GSH ethyl ester (GSE-EE), a cell-permeable form of GSH, efficiently reduced CTSL activity in SUM149 cells (Fig. 5h and Extended Data Fig. 9i–k). GSE-EE treatment also reduced QC6352-induced histone H3 clipping in SUM149 cells (Fig. 5i). We also tested if KDM4C blockade or GSE-EE administration changes the CTSL maturation process. Immunoblot analysis following cell fractionation did not show a notable difference in mature CTSL ratios across the treatments in cell nuclei and cytoplasm (Extended Data Fig. 9l), suggesting that the observed CTSL activation changes were not due to altered CTSL maturation.

Given that both ROS and KDM4C–GRHL2 interaction trigger CTSL activation and histone tail clipping, we conducted a time course experiment to determine the temporal order of these events. We found that both ROS and CTSL activity showed a gradual increase during 6 days of KDM4C inhibitor treatment, but CTSL activation occurred as early as 24 h after treatment, while ROS levels started to elevate between 36 and 60 h (Fig. 5j and Extended Data Fig. 9m). These data suggest that an increase in GRHL2 K453 methylation following KDM4C inhibition might serve as an initial trigger of CTSL activation, while GSH repression and ROS induction are downstream events that further boost CTSL activity through positive feedback.

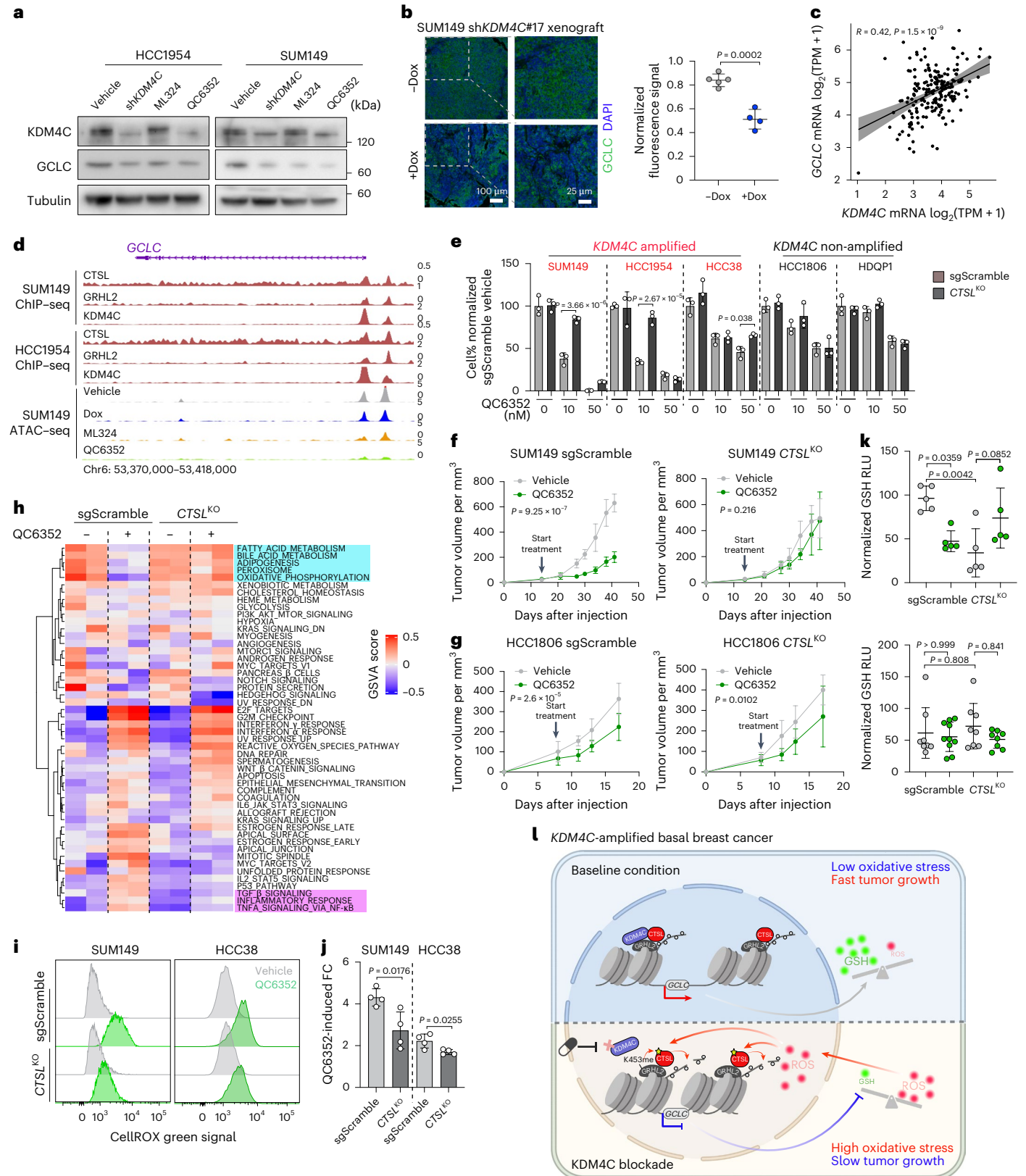
Fig. 6 | KDM4C blockade decreases GCLC expression via CTSL. **a**, Immunoblot analysis of KDM4C and GCLC protein levels in HCC1954 and SUM149 Dox-inducible sh*KDM4C*-expressing cell lines treated with control (no Dox, DMSO), sh*KDM4C* induction (1 $\mu\text{g ml}^{-1}$ Dox, DMSO), 10 μM ML324 (no Dox) or 1 μM QC6352 (no Dox) treatment for 5 days. Tubulin was used as loading control. Experiment was repeated three times independently with similar results. **b**, Representative images of GCLC immunofluorescence staining of xenografts derived from SUM149 cells expressing Dox-inducible sh*KDM4C* from mice fed with ($n = 4$) or without ($n = 5$) Dox diet. Signal intensity of each tumor was quantified by calculating the mean of three representative regions and shown as mean \pm s.d. Two-sided Student's *t* test was used. **c**, Scatter plot depicting correlation between *KDM4C* and *GCLC* mRNA levels in 190 basal breast tumors from the TCGA cohort. Two-sided Pearson correlation was used to calculate the *P* value. The linear regression line with 95% confidence interval is shown. TPM, transcripts per million. **d**, Genomic track view of CTSL, GRHL2 and KDM4C binding in HCC1954 and SUM149 cells at *GCLC* genomic locus. ATAC peaks from Dox-inducible sh*KDM4C*-expressing SUM149 cells treated with vehicle, Dox, ML324 and QC6352 are also displayed using the same scaling. Chr6, chromosome 6. **e**, Bar plot showing the cell percentage normalized to sgScramble cell models treated with DMSO in the indicated groups. Results are shown as mean \pm s.d. from $n = 3$ as representative experiments from at least 2 independent trials. Two-sided ordinary one-way ANOVA was used within each cell

line. **f,g**, Plots depicting the tumor volumes of xenografts derived from SUM149 (**f**) and HCC1806 (**g**) sgScramble and *CTSL*^{KO} cells in mice treated with vehicle or QC6352 at the indicated time points. Data are presented as mean \pm s.d. with $n = 5$ (SUM149) and $n = 10$ (HCC1806) tumors. Two-sided repeated-measure two-way ANOVA was used to compare the tumor growth kinetics. **h**, Heatmap illustrating unsupervised clustering of samples based on the GSVA enrichment scores of the 50 hallmark gene signatures. QC6352 upregulated and downregulated pathways that were rescued by CTSL depletion are highlighted by magenta and cyan rectangles, respectively. **i**, Representative flow cytometry plots depicting the shift of CellROX green signal in SUM149 and HCC38 sgScramble and *CTSL*^{KO} models after 1 μM QC6352 for 5 days. **j**, Bar plot depicting QC6352-induced CellROX green FCs merging three independent experiments (mean \pm s.d.). Two-sided Student's *t* test was used. **k**, Dot plot depicting GSH levels normalized to tumor weight in SUM149 and HCC1806 xenografts collected at endpoint. Data are presented as mean \pm s.d. with $n = 5$ (SUM149) or $n = 10$ (HCC1806) tumors. Two-sided Kruskal–Wallis test was used for each comparison. RLU, relative light units. **l**, Schematic illustration of major findings. HDM KDM4C blocks GRHL2-mediated CTSL activation and histone H3 tail clipping, which have a pivotal role in redox balance via maintaining GSH production and promoting basal breast tumor growth. KDM4C blockade activates CTSL either directly or indirectly and induces redox imbalance, which elevates oxidative stress and impairs basal breast tumor growth. Panel l created with BioRender.com.

KDM4C inhibition decreases GCLC, leading to redox imbalance

To further explore mechanisms underlying the KDM4C-inhibition-induced decrease in GSH, we compared the expression levels of key enzymes and transporters involved in GSH biosynthesis (Extended Data Fig. 10a) in our RNA-seq data. We found a decrease in the expression of several genes, including *GSS* (GSH synthetase), *GCLC* and *GCLM*

(glutamate–cysteine ligase catalytic and modifier subunits, respectively; Extended Data Fig. 10b). Immunoblot analysis confirmed the strong and consistent downregulation of the rate-limiting enzyme GCLC in both HCC1954 and SUM149 cell lines after KDM4C downregulation or inhibition (Fig. 6a). The decrease in GCLC was also validated by immunofluorescence in SUM149 xenografts following Dox-induced



KDM4C knockdown (Fig. 6b). *GCLC* is a subunit of the first rate-limiting enzyme for GSH synthesis coupling glutamate and cysteine into γ -glutamylcysteine, the precursor of GSH. Our prior transcriptomic and metabolomic profiling in 34 TNBC cell lines⁴⁴ identified a positive correlation between *GCLC* and GSH levels, and GSH was the driver of metabolomic heterogeneity in TNBC, splitting samples into low and high groups (Extended Data Fig. 10c). Furthermore, the mRNA levels of *KDM4C* and *GCLC* show a significant positive correlation in basal breast cancer in the TCGA cohort (Fig. 6c), implying coregulation in clinical samples.

We next investigated how *KDM4C* might regulate *GCLC* expression. First, exogenous expression of WT but not catalytically inactive-mutant *KDM4C* rescued *KDM4C* knockdown-induced *GCLC* downregulation, confirming the specificity of this observation to *KDM4C* (Extended Data Fig. 10d). Our ChIP-seq data demonstrated a consistent triple overlap of *CTSL*, *GRHL2* and *KDM4C* peaks at the *GCLC* promoter region in both SUM149 and HCC1954 cell lines, and *KDM4C* inhibition markedly reduced chromatin accessibility of this genomic region (Fig. 6d), implying that *GCLC* downregulation is a potential outcome of *CTSL*-mediated histone H3 tail clipping. This finding was supported by immunoblot analyses in *CTSL*^{KO} cells, where *KDM4C* inhibition failed to dampen *GCLC* expression (Extended Data Fig. 10e). Deletion of *CTSL* also eliminated *KDM4C*-inhibition-induced tumor growth suppression specifically in *KDM4C*-amplified cell models where *CTSL*-mediated histone H3 clipping is observed (Fig. 6e–g). RNA-seq revealed less pronounced QC6352-induced transcriptomic alterations in SUM149 *CTSL*^{KO} cells (Extended Data Fig. 10f–h and Supplementary Table 6). Notably, *CTSL* KO rescued a subset of gene signatures that were altered by QC6352 in sgScramble control cells, including major metabolic functions such as oxidative phosphorylation and fatty acid metabolism (Fig. 6h). In line with this observation, *KDM4C* suppression-associated ROS elevation was partially rescued in *KDM4C*-amplified *CTSL*^{KO} cells (Fig. 6i,j). Finally, *KDM4C* inhibition also failed to decrease GSH levels in xenografts derived from *CTSL*^{KO} SUM149 cells, despite a lower baseline level compared to scramble control (Fig. 6k), while no GSH level changes were detected in HCC1806 *KDM4C*-non-amplified cell line xenografts (Fig. 6k).

Taken together, these results identified the *CTSL*–*GCLC* axis as a key mediator of *KDM4C*-loss-associated metabolomic and epigenetic remodeling and tumor growth suppression in *KDM4C*-amplified basal breast cancer.

Targeting the *KDM4C*–GSH–*CTSL* axis in basal breast cancer

To explore the potential clinical relevance of our findings, we generated *KDM4C* and GSH modulated gene signatures using DEGs associated with *KDM4C* knockdown in HCC1954 and SUM149 cell lines ($n = 23$ genes) and GSH-high versus GSH-low TNBC cell lines ($n = 113$ genes) defined in our previous study⁴⁴, respectively (Supplementary Fig. 2a and Supplementary Table 7). Strong positive correlation between GSH and *KDM4C* signatures was also observed in basal primary tumors in both TCGA and METABRIC cohorts^{22,23} (Supplementary Fig. 2b), recapitulating our findings in cell line models. Furthermore, oxidative stress signature was inversely correlated with *KDM4C* signature (Supplementary Fig. 2c), in line with our experimental results of dampened mitochondrial respiration and increased ROS levels following *KDM4C* inhibition.

The current standard of care for patients with TNBC is chemotherapy with or without immune checkpoint inhibitors². Thus, predictors of patient survival are likely associated with chemotherapy resistance. We examined the enrichment levels of *KDM4C* and GSH signatures between responders and non-responders in five TNBC neoadjuvant patient cohorts treated with different chemotherapies^{45–50}. Although the *KDM4C* and GSH signatures showed a significant positive correlation in all five cohorts, differences between responders and non-responders were only significant in a neoadjuvant cisplatin-treated

cohort⁴⁶ (Supplementary Fig. 2d). In line with this finding, *KDM4C* copy number amplification was uniquely correlated with a lower trend of cisplatin sensitivity in basal cell lineage in the DepMap⁵¹ breast cancer cell line data, while response to paclitaxel, 5-fluorouracil and doxorubicin was not correlated (Supplementary Fig. 2e).

To experimentally validate the prediction that cotargeting *KDM4C* and GSH pathways could overcome cisplatin resistance, we tested the effects of combined cisplatin, BSO and QC6352 treatment in six basal breast cancer cell lines with varying *KDM4C* amplification and *BRCA1* mutation status and GSH metabolic subtypes (Supplementary Fig. 3a). QC6352 and cisplatin combination showed synergistic growth suppression only in HCC3153 cells (Supplementary Fig. 3b,c), and synergism between QC6352 and cisplatin was strengthened with increasing concentration of BSO in a dose-dependent manner in two other *KDM4C*-amplified basal cell lines, SUM149 and HCC38 (Supplementary Fig. 3d,e). In contrast, GSH-low cells (HCC70 and MDA-MB-436) and a *HER2*-amplified basal breast cancer cell line (HCC1954) showed substantial antagonism (Supplementary Fig. 3f–h), likely due to their limited dependency on the GSH pathway. KO of *CTSL* in the SUM149 cell line abolished the enhancement of QC6352 and cisplatin synergy by BSO, again confirming the requirement for *CTSL* to mediate the metabolic effects of *KDM4C* inhibition (Supplementary Fig. 3i). Finally, testing single, dual and triple combinations in the SUM149 xenograft model showed that combination of either QC6352 or BSO with cisplatin was sufficient to suppress GSH production and tumor growth (Supplementary Fig. 3j–n). These results suggest that combined inhibition of *KDM4C* and GSH production might overcome cisplatin resistance in a subset of patients with high GSH pathway activity, encouraging further clinical examination.

Discussion

The frequent genetic alteration of genes encoding histone-modifying enzymes in human cancers implies their role as functional drivers of tumorigenesis. Here we characterized *KDM4C*, an HDM frequently amplified in basal breast cancer, and discovered a unique role for *KDM4C* in *KDM4C*-amplified basal breast cancer in regulating *CTSL*-mediated histone H3 N-terminal tail clipping through modulating lysine methylation of the *GRHL2* transcription factor (Supplementary Table 8).

Reversible post-translational modifications of histone H3 have been extensively characterized, whereas the biological consequences of irreversible histone tail clipping have remained elusive. The tailless histone H3 was shown to precede histone eviction^{52,53}, and blocking *CTSG*-, *ELANE*- and *PRTN3*-mediated histone 3 tail cleavage at Ala21 dominantly induced chromatin opening in monocytes promoting monocyte-to-macrophage differentiation⁵⁴, consistent with our finding that H3 tail clipping leads to decreased chromatin accessibility. Tailless histone H3 could also potentially activate gene expression due to reduced steric effects on the nucleosome and could facilitate recruitment of transcriptional machinery. It may also provide additional docking space for other histone modifiers, such as the PRC2 complex or the *KMT5* histone H4K20 methyltransferase, which may explain higher H3K27me3 and H4K20me3 abundance after *KDM4C* inhibition. Another study revealed that N-terminally truncated histone H3 interferes with intratail H3K36me3 regulation⁵⁵, which could in part explain our inability to detect substantial changes in H3K36me3 following *KDM4C* inhibition, although the cleavage occurred at Ala21. The effects of histone H3 tail clipping on the chromatin are likely to be context-dependent, because we observed cell line-specific differences in chromatin accessibility and transcriptional profiles following *KDM4C* inhibition and mechanisms of acquired ML324 resistance were also somewhat different between HCC1954 and SUM149 models. We also detected histone H4 cleavage upon *KDM4C* blockade that is regulated by a distinct mechanism, as it was universally observed in all cell lines, including the ER⁺ luminal T47D cells, and was blocked by

aspartic acid protease inhibitors. Histone H4 clipping might shape the epigenome differently from that of H3; uncovering this requires future studies.

CTSL is a lysosomal protease, but a nuclear function for CTSL was also reported in cell cycle regulation via proteolytic cleavage of the CDP/Cux transcription factor⁵⁶. Subsequently, CTSL was described as a nuclear protease that cleaves histone H3 during embryonic development^{34,57} and cellular differentiation⁵⁸. Resolving the three-dimensional crystal structure of the CTSL–H3 peptide complex revealed the structural basis of this process³³. However, the mechanism by which CTSL is recruited to the chromatin has been elusive. Here we identified the GRHL2 transcription factor as a chromatin recruiter of CTSL in *KDM4C*-amplified basal breast cancer cells. Furthermore, we discovered that GRHL2 is lysine methylated in a *KDM4C* activity-dependent manner, and its methylation at K453 is required for CTSL-mediated histone H3 clipping. Numerous transcription factors, including p53, E2F-1 and STAT3, have been shown to be methylated at arginine or lysine residues, which can modulate their ability to activate transcription^{59,60}. In many cases, transcription factor methylation is triggered by environmental signals like DNA damage, and methylation/demethylation is carried out by histone methyltransferases and demethylases^{59,60}. Our data suggest that GRHL2 might be a non-histone substrate of *KDM4C*, because *KDM4C* blockade increased its methylation. Our data show that *KDM4C* inhibition does not affect GRHL2–CTSL interaction. However, it is possible that a mono-methylation reader protein could also be part of the complex, or GRHL2 K453 methylation could directly or indirectly influence the catalytic site of CTSL via its inhibitors, cystatin B and cystatin C. Indeed, deletion of *Ctsb* in mice leads to increased nuclear CTSL activity and persistent cleavage of histone H3 in the brain⁶¹. Our results imply that GRHL2 K94 methylation may not have a direct role in regulating CTSL-mediated histone H3 clipping, but it may influence DNA binding given its proximity to the DNA-binding domain. Moreover, the observation of GRHL2 methylation only in *KDM4C*-amplified cells upon *KDM4C* blockade suggests distinct evolutionary paths in *KDM4C*-amplified tumors, with a high level of *KDM4C* keeping GRHL2 demethylated, thereby preventing histone clipping. Further studies are required to decipher the exact mechanisms by which *KDM4C*–GRHL2 regulates CTSL-mediated histone clipping and to delineate why this function is selected for in *KDM4C*-amplified basal breast cancers.

Our metabolomic profiling showed a substantial decrease in GSH, GSSG and their ratio after *KDM4C* inhibition. Previous studies have described that both ROS and GSH can extensively modulate the epigenome. For example, the accumulation of ROS reduces the availability of SAM, limiting the activities of DNMTs and HMTs, leading to global epigenetic alteration⁶². GSH may also directly affect the chromatin via S-glutathionylation of histone H3, destabilizing nucleosome structure and opening chromatin^{63,64}. The GSH biosynthesis pathway has previously been identified as a therapeutic vulnerability in TNBC⁶⁵ and inhibition of the glutamate–cystine antiporter xCT efficiently impaired the growth of glutamine auxotroph TNBC lines⁶⁶. GSH also has a role in therapeutic resistance, and pharmacological depletion of GSH sensitizes cells to cisplatin^{67,68}. Here we found that the *KDM4C*–CTSL axis is an alternative route to inhibit GSH production, which could yield synergism with cisplatin in a subset of basal breast tumors. Because cisplatin is more effective in DNA repair-defective (for example, *BRCA1* mutant) tumors⁶⁹, our results suggest that combined targeting of *KDM4C*–GSH may be a putative therapeutic strategy in these patients.

A limitation of our study is that we did not perform quantitative ChIP–seq experiments using spike-in controls, and thus, the lack of global differences in H3K9me3 following *KDM4C* inhibition needs to be interpreted with caution. Our functional studies were performed in cell lines; therefore, the methylation of GRHL2 and its association with CTSL and *KDM4C* activity would need to be validated in primary patient samples. Finally, mechanisms that drive the evolution of *KDM4C*-amplified

basal breast cancer to prevent GRHL2 methylation and histone H3 clipping by CTSL would need to be delineated in future studies.

In summary, we discovered a unique function of *KDM4C* specific to *KDM4C*-amplified basal breast cancer, elucidating the underlying mechanisms and clinical significance. Our results serve as a basis for the clinical testing of *KDM4C* inhibitors in *KDM4C*-amplified basal breast cancer, potentially in combination with chemotherapy and agents targeting the glutamine/GSH pathway.

Online content

Any methods, additional references, Nature Portfolio reporting summaries, source data, extended data, supplementary information, acknowledgements, peer review information; details of author contributions and competing interests; and statements of data and code availability are available at <https://doi.org/10.1038/s41588-025-02197-z>.

References

- Perou, C. M. et al. Molecular portraits of human breast tumours. *Nature* **406**, 747–752 (2000).
- Garrido-Castro, A. C., Lin, N. U. & Polyak, K. Insights into molecular classifications of triple-negative breast cancer: improving patient selection for treatment. *Cancer Discov.* **9**, 176–198 (2019).
- Lehmann, B. D. et al. Multi-omics analysis identifies therapeutic vulnerabilities in triple-negative breast cancer subtypes. *Nat. Commun.* **12**, 6276 (2021).
- Lehmann, B. D. et al. Identification of human triple-negative breast cancer subtypes and preclinical models for selection of targeted therapies. *J. Clin. Invest.* **121**, 2750–2767 (2011).
- Alderton, G. K. Epigenetic and genetic heterogeneity in metastasis. *Nat. Rev. Cancer* **17**, 141 (2017).
- Carter, B. & Zhao, K. The epigenetic basis of cellular heterogeneity. *Nat. Rev. Genet.* **22**, 235–250 (2021).
- Henikoff, S. & Shilatifard, A. Histone modification: cause or cog? *Trends Genet.* **27**, 389–396 (2011).
- Audia, J. E. & Campbell, R. M. Histone modifications and cancer. *Cold Spring Harb. Perspect. Biol.* **8**, a019521 (2016).
- Baylin, S. B. & Jones, P. A. Epigenetic determinants of cancer. *Cold Spring Harb. Perspect. Biol.* **8**, a019505 (2016).
- Flavahan, W. A., Gaskell, E. & Bernstein, B. E. Epigenetic plasticity and the hallmarks of cancer. *Science* **357**, eaal2380 (2017).
- Berry, W. L. & Janknecht, R. *KDM4/JMJD2* histone demethylases: epigenetic regulators in cancer cells. *Cancer Res.* **73**, 2936–2942 (2013).
- Nikolsky, Y. et al. Genome-wide functional synergy between amplified and mutated genes in human breast cancer. *Cancer Res.* **68**, 9532–9540 (2008).
- Liu, G. et al. Genomic amplification and oncogenic properties of the *GASC1* histone demethylase gene in breast cancer. *Oncogene* **28**, 4491–4500 (2009).
- Loh, Y.-H., Zhang, W., Chen, X., George, J. & Ng, H.-H. *Jmjd1a* and *Jmjd2c* histone H3 Lys 9 demethylases regulate self-renewal in embryonic stem cells. *Genes Dev.* **21**, 2545–2557 (2007).
- Das, P. P. et al. Distinct and combinatorial functions of *Jmjd2b/Jmjd4b* and *Jmjd2c/Kdm4c* in mouse embryonic stem cell identity. *Mol. Cell* **53**, 32–48 (2014).
- Katainen, R. et al. Novel germline variant in the histone demethylase and transcription regulator *KDM4C* induces a multi-cancer phenotype. *J. Med. Genet.* **59**, 644–651 (2021).
- Villacis, R. A. R. et al. Rare germline alterations in cancer-related genes associated with the risk of multiple primary tumor development. *J. Mol. Med.* **95**, 523–533 (2017).
- Lee, D. H. et al. Histone demethylase *KDM4C* controls tumorigenesis of glioblastoma by epigenetically regulating p53 and c-Myc. *Cell Death Dis.* **12**, 89 (2021).

19. Cheung, N. et al. Targeting aberrant epigenetic networks mediated by PRMT1 and KDM4C in acute myeloid leukemia. *Cancer Cell* **29**, 32–48 (2016).
20. Garcia, J. & Lizcano, F. KDM4C activity modulates cell proliferation and chromosome segregation in triple-negative breast cancer. *Breast Cancer* **10**, 169–175 (2016).
21. Garcia, J. & Lizcano, F. Kdm4c is recruited to mitotic chromosomes and is relevant for chromosomal stability, cell migration and invasion of triple negative breast cancer cells. *Breast Cancer* **12**, 1178223418773075 (2018).
22. Koboldt, D. et al. Comprehensive molecular portraits of human breast tumours. *Nature* **490**, 61–70 (2012).
23. Curtis, C. et al. The genomic and transcriptomic architecture of 2,000 breast tumours reveals novel subgroups. *Nature* **486**, 346–352 (2012).
24. Rai, G. et al. *Probe Reports From the NIH Molecular Libraries Program* (National Center for Biotechnology Information, 2010).
25. Chen, Y. K. et al. Design of KDM4 inhibitors with antiproliferative effects in cancer models. *ACS Med. Chem. Lett.* **8**, 869–874 (2017).
26. Yu, C. et al. High-throughput identification of genotype-specific cancer vulnerabilities in mixtures of barcoded tumor cell lines. *Nat. Biotechnol.* **34**, 419–423 (2016).
27. Guillen, K. P. et al. A human breast cancer-derived xenograft and organoid platform for drug discovery and precision oncology. *Nat. Cancer* **3**, 232–250 (2022).
28. Sun, H. et al. Comprehensive characterization of 536 patient-derived xenograft models prioritizes candidates for targeted treatment. *Nat. Commun.* **12**, 5086 (2021).
29. Zhao, E. et al. KDM4C and ATF4 cooperate in transcriptional control of amino acid metabolism. *Cell Rep.* **14**, 506–519 (2016).
30. Kupershmit, I., Khoury-Haddad, H., Awwad, S. W., Guttmann-Raviv, N. & Ayoub, N. KDM4C(GASC1) lysine demethylase is associated with mitotic chromatin and regulates chromosome segregation during mitosis. *Nucleic Acids Res.* **42**, 6168–6182 (2014).
31. Pedersen, M. T. et al. The demethylase JMJD2C localizes to H3K4me3-positive transcription start sites and is dispensable for embryonic development. *Mol. Cell. Biol.* **34**, 1031–1045 (2014).
32. Pack, L. R., Yamamoto, K. R. & Fujimori, D. G. Opposing chromatin signals direct and regulate the activity of lysine demethylase 4C (KDM4C). *J. Biol. Chem.* **291**, 6060–6070 (2016).
33. Adams-Cioaba, M. A., Krupa, J. C., Xu, C., Mort, J. S. & Min, J. Structural basis for the recognition and cleavage of histone H3 by cathepsin L. *Nat. Commun.* **2**, 197 (2011).
34. Duncan, E. M. et al. Cathepsin L proteolytically processes histone H3 during mouse embryonic stem cell differentiation. *Cell* **135**, 284–294 (2008).
35. Ju, X. et al. Neuraminidase of influenza A virus binds lysosome-associated membrane proteins directly and induces lysosome rupture. *J. Virol.* **89**, 10347–10358 (2015).
36. Thibodeau, A., Marquez, E. J., Shin, D. G., Vera-Licona, P. & Ucar, D. Chromatin interaction networks revealed unique connectivity patterns of broad H3K4me3 domains and super enhancers in 3D chromatin. *Sci. Rep.* **7**, 14466 (2017).
37. Mohammed, H. et al. Endogenous purification reveals GREB1 as a key estrogen receptor regulatory factor. *Cell Rep.* **3**, 342–349 (2013).
38. Dasgupta, M., Dermawan, J. K., Willard, B. & Stark, G. R. STAT3-driven transcription depends upon the dimethylation of K49 by EZH2. *Proc. Natl Acad. Sci. USA* **112**, 3985–3990 (2015).
39. Cascella, B. & Mirica, L. M. Kinetic analysis of iron-dependent histone demethylases: α -ketoglutarate substrate inhibition and potential relevance to the regulation of histone demethylation in cancer cells. *Biochemistry* **51**, 8699–8701 (2012).
40. Rawlings, N. D. & Salvesen, G. (eds). *Handbook of Proteolytic Enzymes* 1808–1817 (Academic Press, 2013).
41. Wang, M., Wang, R., Xie, X., Sun, G. & Sun, X. Araloside C protects H9c2 cardiomyoblasts against oxidative stress via the modulation of mitochondrial function. *Biomed. Pharmacother.* **117**, 109143 (2019).
42. Armstrong, J. A. et al. Oxidative stress alters mitochondrial bioenergetics and modifies pancreatic cell death independently of cyclophilin D, resulting in an apoptosis-to-necrosis shift. *J. Biol. Chem.* **293**, 8032–8047 (2018).
43. Gong, Y. et al. Metabolic-pathway-based subtyping of triple-negative breast cancer reveals potential therapeutic targets. *Cell Metab.* **33**, 51–64 (2021).
44. Jovanovic, B. et al. Heterogeneity and transcriptional drivers of triple-negative breast cancer. *Cell Rep.* **42**, 113564 (2023).
45. Miyake, T. et al. GSTP1 expression predicts poor pathological complete response to neoadjuvant chemotherapy in ER-negative breast cancer. *Cancer Sci.* **103**, 913–920 (2012).
46. Silver, D. P. et al. Efficacy of neoadjuvant cisplatin in triple-negative breast cancer. *J. Clin. Oncol.* **28**, 1145 (2010).
47. Popovici, V. et al. Effect of training-sample size and classification difficulty on the accuracy of genomic predictors. *Breast Cancer Res.* **12**, R5 (2010).
48. Magbanua, M. J. M. et al. Serial expression analysis of breast tumors during neoadjuvant chemotherapy reveals changes in cell cycle and immune pathways associated with recurrence and response. *Breast Cancer Res.* **17**, 73 (2015).
49. Prat, A. et al. Research-based PAM50 subtype predictor identifies higher responses and improved survival outcomes in HER2-positive breast cancer in the NOAH study. *Clin. Cancer Res.* **20**, 511–521 (2014).
50. Itoh, M. et al. Estrogen receptor (ER) mRNA expression and molecular subtype distribution in ER-negative/progesterone receptor-positive breast cancers. *Breast Cancer Res. Treat.* **143**, 403–409 (2014).
51. Tsherniak, A. et al. Defining a cancer dependency map. *Cell* **170**, 564–576 (2017).
52. Santos-Rosa, H. et al. Histone H3 tail clipping regulates gene expression. *Nat. Struct. Mol. Biol.* **16**, 17–22 (2009).
53. Azad, G. K., Swagatika, S., Kumawat, M., Kumawat, R. & Tomar, R. S. Modifying chromatin by histone tail clipping. *J. Mol. Biol.* **430**, 3051–3067 (2018).
54. Cheung, P. et al. Repression of CTSG, ELANE and PRTN3-mediated histone H3 proteolytic cleavage promotes monocyte-to-macrophage differentiation. *Nat. Immunol.* **22**, 711–722 (2021).
55. Psathas, J. N., Zheng, S., Tan, S. & Reese, J. C. Set2-dependent K36 methylation is regulated by novel intratril interactions within H3. *Mol. Cell. Biol.* **29**, 6413–6426 (2009).
56. Goulet, B. et al. A cathepsin L isoform that is devoid of a signal peptide localizes to the nucleus in S phase and processes the CDP/Cux transcription factor. *Mol. Cell* **14**, 207–219 (2004).
57. Morin, V. et al. The protease degrading sperm histones post-fertilization in sea urchin eggs is a nuclear cathepsin L that is further required for embryo development. *PLoS ONE* **7**, e46850 (2012).
58. Ferrari, K. J. et al. Intestinal differentiation involves cleavage of histone H3 N-terminal tails by multiple proteases. *Nucleic Acids Res.* **49**, 791–804 (2021).
59. Carr, S. M., Poppy Roworth, A., Chan, C. & La Thangue, N. B. Post-translational control of transcription factors: methylation ranks highly. *FEBS J.* **282**, 4450–4465 (2015).
60. Mannervik, M. Beyond histones: the elusive substrates of chromatin regulators. *Genes Dev.* **38**, 357–359 (2024).

61. Daura, E., Tegelberg, S., Hakala, P., Lehesjoki, A. E. & Joensuu, T. Cystatin B deficiency results in sustained histone H3 tail cleavage in postnatal mouse brain mediated by increased chromatin-associated cathepsin L activity. *Front. Mol. Neurosci.* **15**, 1069122 (2022).
62. Kietzmann, T., Petry, A., Shvetsova, A., Gerhold, J. M. & Görlach, A. The epigenetic landscape related to reactive oxygen species formation in the cardiovascular system. *Br. J. Pharmacol.* **174**, 1533–1554 (2017).
63. García-Giménez, J. L. et al. Histone h3 glutathionylation in proliferating mammalian cells destabilizes nucleosomal structure. *Antioxid. Redox Signal.* **19**, 1305–1320 (2013).
64. De Luca, A. et al. Treatment of doxorubicin-resistant MCF7/Dx cells with nitric oxide causes histone glutathionylation and reversal of drug resistance. *Biochem. J.* **440**, 175–183 (2011).
65. Beatty, A. et al. Metabolite profiling reveals the glutathione biosynthetic pathway as a therapeutic target in triple-negative breast cancer. *Mol. Cancer Ther.* **17**, 264–275 (2018).
66. Timmerman, L. A. et al. Glutamine sensitivity analysis identifies the xCT antiporter as a common triple-negative breast tumor therapeutic target. *Cancer Cell* **24**, 450–465 (2013).
67. Rocha, C. R. R. et al. Glutathione depletion sensitizes cisplatin- and temozolomide-resistant glioma cells in vitro and in vivo. *Cell Death Dis.* **5**, e1505 (2014).
68. Li, Q. et al. The effects of buthionine sulfoximine on the proliferation and apoptosis of biliary tract cancer cells induced by cisplatin and gemcitabine. *Oncol. Lett.* **11**, 474–480 (2016).
69. Byrski, T. et al. Response to neoadjuvant therapy with cisplatin in BRCA1-positive breast cancer patients. *Breast Cancer Res. Treat.* **115**, 359–363 (2009).

Publisher's note Springer Nature remains neutral with regard to jurisdictional claims in published maps and institutional affiliations.

Open Access This article is licensed under a Creative Commons Attribution 4.0 International License, which permits use, sharing, adaptation, distribution and reproduction in any medium or format, as long as you give appropriate credit to the original author(s) and the source, provide a link to the Creative Commons licence, and indicate if changes were made. The images or other third party material in this article are included in the article's Creative Commons licence, unless indicated otherwise in a credit line to the material. If material is not included in the article's Creative Commons licence and your intended use is not permitted by statutory regulation or exceeds the permitted use, you will need to obtain permission directly from the copyright holder. To view a copy of this licence, visit <http://creativecommons.org/licenses/by/4.0/>.

© The Author(s) 2025

¹Department of Medical Oncology, Dana–Farber Cancer Institute, Boston, MA, USA. ²Department of Medicine, Brigham and Women's Hospital, Boston, MA, USA. ³Department of Medicine, Harvard Medical School, Boston, MA, USA. ⁴Center for Functional Cancer Epigenetics, Dana–Farber Cancer Institute, Boston, MA, USA. ⁵The Eli and Edythe L. Broad Institute, Cambridge, MA, USA. ⁶Cambridge Research Institute, University of Cambridge, Cambridge, UK. ⁷Department of Stem Cell and Regenerative Biology, Harvard University, Cambridge, MA, USA. ⁸Department of Biostatistics, Harvard T. H. Chan School of Public Health, Boston, MA, USA. ⁹Department of Data Sciences, Dana–Farber Cancer Institute, Boston, MA, USA. ¹⁰National Center for Advancing Translational Sciences, Bethesda, MD, USA. ¹¹Vanderbilt University Medical Center, Nashville, TN, USA. ¹²These authors contributed equally: Zheqi Li, Guillermo Peluffo. ✉ e-mail: kornelia_polyak@dfci.harvard.edu

Methods

Ethics statement

All human and animal studies were conducted in compliance with the relevant ethical guidelines and approved by the appropriate ethics committees as detailed below. All animal studies were conducted in accordance with the regulations formulated by the Dana-Farber Cancer Institute (DFCI) Animal Care and Use Committee protocol 11-023. Surgically resected breast tumor samples have been previously described^{70,71} and were collected at the Instituto Nacional de Enfermedades Neoplásicas (Lima, Perú) following institutionally approved protocol INEN 10-018. Written informed consent was obtained from all participants or waived for deceased patients. Samples were deidentified before transport to the laboratory.

Breast cancer cell lines

Breast cancer cell lines were obtained from American Type Culture Collection (ATCC), Leibniz Institute DSMZ – German Collection of Microorganisms and Cell Cultures GmbH (DSMZ) or generously provided by outside academic institutions under Material Transfer Agreement (MTA) (see Supplementary Table 9 for details) and cultured following the provider's recommendations. The identity of the cell lines was confirmed by short tandem repeat analysis, and they were regularly tested for mycoplasma. Details of the generation of cell line derivatives are described in Supplementary Note.

Animal experiments

For xenograft assays using *KDM4C* knockdown HCC1954 and SUM149 models, as well as cisplatin/QC6352/BSO drug combination assay, female NCr nude (CrTac:NCr-Foxn1nu) mice were purchased from Taconic Biosciences at 5–6 weeks of age. For experiments using HCl-041 PDX, *KDM4C* knockdown HCC1806 and *CTSL*^{ko} SUM149 and HCC1806 models, female NSG (NOD.Cg-Prkdcscid Il2rgtm1Wjl/Szj) mice were purchased from the Jackson Laboratory at 5–6 weeks of age. Mice were housed 5 to a cage with ad libitum access to food and water in 20 °C ambient temperature, 40–50% humidity and a 12-h light/12-h dark cycle. Experimental details are described in Supplementary Note.

Immunoblot and immunoprecipitation assays

Details of immunoblot analyses are described in Supplementary Note. For immunoprecipitation, cells were cultured to 80% confluency in three 15 cm dishes, washed and collected in ice-cold PBS and then lysed in cytoplasmic lysis buffer (10 mM HEPES, 10 mM KCl, 1.5 mM MgCl₂, 0.5% NP40 and 0.5 mM DTT) by rotating at 4 °C for 10 min. The lysates were centrifuged, and nuclear pellets were lysed in nuclear lysis buffer (20 mM HEPES, 300 mM NaCl, 1.5 mM MgCl₂, 0.5% NP40, 10% glycerol and 0.2 mM EDTA) by rotating at 4 °C for 10 min. The samples were sonicated using a cup-probe sonicator for a total of 5 min with a 20 s on/10 s off cycle at 75% amplitude, followed by centrifugation. Supernatants were diluted twofold with dilution buffer (20 mM Tris–HCl (pH 8.0), 1.5 mM MgCl₂, 0.5% NP40 and 0.2 mM EDTA). DNase I digestion was performed using Qiagen DNase I at 20 U ml⁻¹ for 30 min at 37 °C. Each sample was divided into two for immunoprecipitation with 5 µg of specific antibody or isotype IgG control, both incubated overnight at 4 °C. Next, 25 µl of Pierce protein A/G magnetic beads were added to each sample and incubated for an additional 2 h at 4 °C. The samples were washed twice with low-salt washing buffer (20 mM Tris–HCl (pH 8.0), 150 mM NaCl, 1.5 mM MgCl₂, 0.5% NP40 and 0.2 mM EDTA) and once with low Tris–EDTA buffer. The beads were resuspended in nuclear lysis buffer containing lithium dodecyl sulfate and a reducing reagent and heated at 95 °C for 5 min. The supernatants were used directly for immunoblotting, together with 10% input loading. Detailed antibody information is provided in Supplementary Table 9. Immunoblot intensity of each band was quantified using ImageJ (v1.53q) and labeled in the panels.

Metabolomic profiling

Inducible sh*KDM4C*-infected HCC1954, SUM149, T47D and HCC70 parental cells were plated in duplicate in 3 biological replicates for each group following control (no doxycycline (Dox), DMSO), sh*KDM4C* induction (plus 0.1 µg ml⁻¹ Dox) or 10 µM ML324 (ML, no Dox) treatment in the first 3 lines and with or without 10 µM ML324 treatment in HCC70 for 5 days. Polar metabolites were extracted as described⁷² (further details are given in Supplementary Note).

Histone MS

Exponentially growing cells were collected by trypsinization, pelleted, washed and snap frozen. For inhibitor treatment, 100 µM AEBSF HCl, 100 µM pepstatin A, 10 µM SID2668150, 10 µM E64d and 5 µM cathepsin inhibitor III were applied for 24 h. Histone modification profiling was performed as described in ref. 73. Briefly, histones were extracted from cell nuclei by acid extraction and precipitated with trichloroacetic acid. Isolated histones (10 µg per sample) were propionylated, desalted and digested overnight with trypsin following standard protocols. A second round of propionylation was performed before desalting. Before MS analysis, a reference mixture of isotopically labeled synthetic peptides for histones H3 and H4 was added to each sample. Peptides were separated using a C18 column (Thermo Fisher Scientific, EASY-nLC 1000) and analyzed by MS using a parallel reaction monitoring method on a Q Exactive Plus Orbitrap (Thermo Fisher Scientific). Chromatographic peak areas of endogenous (light, L) and synthetic standard (heavy, H) peptides were extracted using Skyline, and L:H peak area ratios were calculated. These ratios were log₂-transformed, normalized to an unmodified region of H3 (41–49) or H4 (68–78), row median normalized for each histone mark and further adjusted to the mean of vehicle groups. For peptide clipping identification, samples were analyzed using liquid chromatography MS (Proxeon EASY-nLC 1000 UHPLC and Q Exactive⁺ mass spectrometer) in two different ways. First, samples were injected using a targeted, parallel reaction monitoring acquisition method to strictly monitor for the presence of defined combinatorial forms of modified histone peptides. Second, samples were injected for a second time, and peptides were quantified using an unbiased, data-dependent acquisition (DDA) strategy that monitors for all peptides present in the sample. Results were analyzed independently using the Skyline software package (v4.0) and the Spectrum Mill (v7.0), respectively.

Immunoprecipitation MS

For MS on CTSL immunoprecipitants, pulled-down proteins were digested on beads using trypsin digest buffer (2 M urea, 50 mM Tris–HCl, 2 mM DTT and 0.005 µg ml⁻¹ trypsin) with shaking for 1 h at 25 °C. Supernatant was transferred to a cold tube, and the beads were washed twice with urea buffer (2 M urea and 50 mM Tris–HCl), combining the wash volumes with the original supernatant. This entire process, including the digestion, was repeated for a second time. Both digests from each sample were pooled. Each sample was then subjected to reducing conditions (5 mM dithiothreitol) to cleave disulfide bonds. Unmodified cysteine residues were then alkylated (10 mM iodoacetamide) to prevent the reformation of disulfides. Proteins were then digested into peptides using an overnight trypsin digest. Samples were isotopically labeled to multiplex the sample set, allowing for more robust cross-sample comparisons. Samples were analyzed via liquid chromatography MS (Proxeon EASY-nLC 1000 UHPLC and Q Exactive⁺ mass spectrometer), using an unbiased, DDA strategy. Results were processed using Spectrum Mill. Proteins were filtered based on the criteria that they must include two or more unique human peptides. Results were interpreted using the ProTIGY interactive visualization tool (v0.7.5). For MS on GRHL2 immunoprecipitants, cells were first treated with 1 µM QC6352 for 5 days, followed by the standard immunoprecipitation procedure. Proteins were separated using SDS–PAGE followed by Coomassie blue staining. Standard in-gel digestion protocol was performed on the GRHL2 SDS–PAGE gel band. Briefly, gel pieces were destained using

50% acetonitrile/H₂O and 50 mM ammonium bicarbonate solution on a shaker (400 r.p.m.) for 1.5 h at room temperature. Subsequently, proteins were reduced and alkylated with 10 mM dithiothreitol at 37 °C and 50 mM iodoacetamide at room temperature, respectively, for 45 min at 400 r.p.m. Gel pieces were washed once with 50% acetonitrile/H₂O and twice with 50 mM ammonium bicarbonate solution for 15 min each at 400 r.p.m. and then dehydrated with 100% acetonitrile for 10 min. Sample was digested overnight with 50 ng trypsin at 600 r.p.m. at 37 °C, and the supernatant was lyophilized before reverse-phase C18 StageTip desalting following standard protocol. Peptides were lyophilized and reconstituted in 5 µl 3% acetonitrile/5% formic acid, and 4 µl were subjected to nano liquid chromatography–tandem mass spectrometry. Peptides were separated on a self-packed C18 column with a 60-min gradient (Vanquish Neo UHPLC; Thermo Fisher Scientific) and analyzed using a standard DDA on an Exploris 480 (Thermo Fisher Scientific). The RAW file was searched in Spectrum Mill (Rev BI.08.02.218) against a SwissProt database, using cysteine carbamidomethylation as a fixed modification and lysine methylation as a variable modification. Spectra annotation was generated by Interactive Peptide Spectral Annotator⁷⁴.

ChIP–seq

ChIP–seq was performed as previously described in ref. 75. Further details are given in Supplementary Note.

qPLEX-RIME

qPLEX-RIME was performed essentially as described in ref. 76, except we only used formaldehyde for cross-linking. Further details are given in Supplementary Note.

RNA-seq

RNA-seq libraries were prepared using the Illumina TruSeq Stranded mRNA sample preparation kit from 500 ng of purified total RNA according to the manufacturer's protocol (see details in Supplementary Note).

CTSL activity and ROS assays

CTSL activity was detected using the Magic Red Cathepsin L Assay Kit (MyBiosource), and ROS levels were assessed using the CellROX Green and CellROX Orange reagents (Thermo Fisher Scientific) following the manufacturer's protocol. Briefly, 2×10^5 cells were seeded in 6-well plates and treated with DMSO, 1 µg ml⁻¹ Dox, 10 µM ML324 or 1 µM QC6352 for the indicated time. For live cell imaging, adherent living cells were directly stained with 1× Magic Red CTSL substrates or 1× CellROX Green reagent for 30 min at 37 °C. Cells were washed 3× with PBS and stained with Hoechst 33342 for 5 min, and the images were acquired using a Nikon Eclipse microscope using ×20 magnification. ROS and CTSL magic red intensity were quantified per cell using ImageJ (v1.53q) for statistical comparison. For flow cytometry, cells were first digested and then stained with 200 µl PBS solution containing 1× magic red and 1× CellROX green for 30 min at 37 °C. Stained cells were dissociated into single cells and resuspended in 300 µl PBS and analyzed on the BD LSRFortessa Cell Analyzer with FITC and PE-Texas Red channels. An unstained sample was used as negative control. FCS files derived from BD FACSDiva (v9.0) were further analyzed using FlowJo (v10.10), and the geometric mean of each sample was calculated for statistical comparison. Gating strategy is included as Supplementary Fig. 1.

Seahorse mito-stress assay

Seahorse mito-stress assay was performed using the Seahorse XF Cell Mito-Stress Test Kit (Agilent) following the manufacturer's protocol (details are described in Supplementary Note).

GSH-Glo and GSH/GSSG assay

GSH and GSSG quantification was performed using the GSH-Glo GSH Assay Kit or GSH/GSSG-Glo Assay Kit (Promega) following the manufacturer's protocol (details are described in Supplementary Note).

Cellular viability and colony growth assays

Cell numbers were determined by the FluoReporter Blue Fluorometric dsDNA Quantitation Kit (Thermo Fisher Scientific). For drug dose response assays, 4,000 cells were seeded into a 96-well plate per well on day 0, cell numbers were quantified on day 5 after treatment and cell growth rates at different doses were normalized to the mean of vehicle values. Nonlinear fit of dose response curves was conducted by PRISM, and area under the curve (AUC) values were derived. For combination treatment, cells were pretreated with corresponding doses of ML324 and QC6352 for 3 days in 10 cm dishes and then replated into a 96-well plate with 4,000 cells per well. A combination of BSO, cisplatin and ML324/QC6352 was added after 24 h with 6 biological replicates, and cell numbers were quantified after 5 days. The expected drug combination responses were calculated using the ZIP reference model in SynergyFinder⁷⁷. Deviations between observed and expected responses indicate synergy for positive values and antagonism for negative values. For colony growth assays, cells were seeded into 6-well plates with 5,000 cells per well in triplicate and treated with compounds 24 h after plating. For siRNA knockdown experiments, reverse transfection was performed on day 0 with 31.25 nmol siRNAs per well using Lipofectamine RNAiMAX Reagent. siRNA transfection was refreshed on day 6. Cells were quantified between 12 and 18 days in different experiments. Briefly, cells were fixed in ice-cold methanol (Thermo Fisher Scientific) for 10 min and then stained with crystal violet staining solution (0.5%) at room temperature for 15 min. Images of each well were taken after washing three times with ddH₂O. For quantification, crystal violet was dissolved in 10% SDS with a 500 µl volume for each well. Optical density at 450 nm value of 100 µl of destained crystal violet solution from each assay well was measured using a microplate reader with three technical replicates.

Immunofluorescence analyses

Immunofluorescence staining was performed on cells growing in 48-well plates on glass coverslips. In total, 10,000 cells were seeded into each well. Inducible SUM149 shKDM4C-infected cells were treated with control (no Dox, DMSO), shKDM4C induction (plus 1 µg ml⁻¹ Dox), 10 µM ML324 (no Dox), 1 µM QC6352 (no Dox) for 5 days or 1 µM Leu–Leu methyl ester hydrobromide for 24 h. Cells were then washed, fixed in 4% paraformaldehyde and blocked in 5% BSA/0.3% Triton X-100/PBS solution for 1 h. Primary antibodies against CTSL (Novus Biologicals, AF952; 1:100), GRHL2 (Sigma-Aldrich, HPA004820; 1:100) and KDM4C (Novus Biologicals, NBPI-49600; 1:100) were applied for 1 h at room temperature. Cells were washed, incubated with secondary antibodies for 30 min at room temperature and mounted using VECTASHIELD Antifade Mounting Medium with DAPI (Vector Laboratories). Cells were imaged using a Zeiss 980 Confocal Imaging System at ×63 magnification. In total, 10–13 Z-stack images were taken and merged for final visualization. Immunofluorescence staining on formalin-fixed paraffin-embedded tissue sections was performed essentially as described⁷⁸. Briefly, FFPE sections were deparaffinized and rehydrated, followed by antigen retrieval in citrate buffer (pH 6, DAKO) for 30 min in a steamer. Endogenous peroxidase was quenched by a 10-min incubation in 3% H₂O₂. Blocking solution (0.3% Triton X and 5% goat serum in PBS) was applied for 1 h. Primary antibody was applied at a 1:100 dilution in blocking buffer overnight at 4 °C in a moist chamber. Secondary antibody was applied for 30 min at room temperature. Slides were mounted with Vibrance Antifade Mounting Medium with DAPI (VECTASHIELD). Images were acquired using a Nikon Eclipse microscope.

Hi-ChIP

In situ long-range DNA-protein contact libraries were essentially generated as published⁷⁹ with minor modifications described in Supplementary Note.

ATAC-seq

Inducible *shKDM4C*-infected SUM149, HCC1954 and HCC1806 models were plated in 15 cm dishes and treated for 5 days under the following conditions: control (0.1% DMSO, no Dox), $1 \mu\text{g ml}^{-1}$ Dox or $10 \mu\text{M}$ ML324 (no Dox). One sample from each shKDM4C17 and 20 model was used for SUM149 and HCC1954 cells, and biological duplicates from shKDM4C 5 were used for HCC1806. Fifty thousand cells were resuspended in 1 ml of cold ATAC-seq resuspension buffer (RSB; 10 mM Tris-HCl (pH 7.4), 10 mM NaCl and 3 mM MgCl₂). Cells were centrifuged at maximum speed for 10 min in a prechilled (4 °C) fixed-angle centrifuge. Supernatant was carefully aspirated, and cell pellets were resuspended in 50 μl of ATAC-seq RSB containing 0.1% NP40, 0.1% Tween 20 and 0.01% digitonin by pipetting up and down 3 times and incubated on ice for 3 min. After lysis, 1 ml of ATAC-seq RSB containing 0.1% Tween 20 was added, and the tubes were inverted to mix. Nuclei were centrifuged for 5 min at maximum speed in a prechilled fixed-angle centrifuge. Supernatant was removed, and nuclei were resuspended in 50 μl of transposition mix (25 μl (2 \times) TD buffer, 2.5 μl transposase (100 nM final), 16.5 μl PBS, 0.5 μl 1% digitonin, 0.5 μl (10%) Tween 20 and 5 μl water) by pipetting up and down 6 times. Transposition reactions were incubated at 37 °C for 30 min in a thermomixer with shaking at 1,000 r.p.m. Reactions were cleaned up with Qiagen MinElute columns. Libraries were amplified as previously described⁸⁰. The 35-bp paired-end reads were sequenced on a NextSeq500 instrument (Illumina).

PRISM screen

PRISM screen was performed as previously described²⁶. Further details are given in Supplementary Note.

RNA-seq data analysis

RNA-seq data were processed using the VIPER pipeline⁸¹. Further details are given in Supplementary Note.

ChIP-seq and ATAC-seq data analyses

ChIP-seq and ATAC-seq data processing were based on the ChIPs pipeline⁸². Further details are given in Supplementary Note.

Hi-ChIP analysis

CTSL Hi-ChIP data were processed using the HiC-Pro pipeline (v3.1.0)⁸³. Briefly, reads were aligned to the hg19 reference genome using Bowtie2 (ref. 84). After restriction site detection, a second round of alignment was performed. Validated pairs were filtered and distributed to the whole genome, binned in 500 kb resolution. Interchromosomal and intrachromosomal interactions were visualized using the HiTC package (v1.38.0)⁸⁵ after ICE normalization. Differential interchromosomal and intrachromosomal interaction sites were called using the HiCCompare package (v1.16.0)⁸⁶ using the cutoff of interaction frequency >50 and adjusted $P < 0.05$.

Statistics and reproducibility

All quantitative data are presented as the mean values \pm s.d. with indicated replicates in the corresponding legends including Figs. 2c,g,i, 4l, 5d,e,g,h,j and 6b,e-g,j,k, Extended Data Figs. 2e,f, 3a-e,h,k,l,n, 4l, 5g,m,o, 8e,f,j and 9b,e,g,i,k, and Supplementary Fig. 3j-n. All box plots span the upper quartile (upper limit), median (center) and lower quartile (lower limit). Whiskers extend a maximum of 1.5 \times interquartile range (IQR). No statistical methods were used to predetermine the sample size for the experiments. Sequencing data that did not pass quality control were excluded from analysis. In all in vivo experiments, mice were randomized to treatment groups; otherwise, experiments were not randomized. Sequencing data processing was performed by bioinformaticians blinded to the identity of the samples. The investigators were not blinded to allocation during other experiments and outcome assessment. Figure 6l was created with BioRender.com. All figures were assembled with Affinity Designer 2.0. Bioinformatic data

were analyzed and visualized using R (v.4.3.1) software. Experimental data were analyzed and visualized using GraphPad Prism (v.10.3.1) software. Statistic test in R uses a precision floating-point format, which has a lower limit of approximately 2.2×10^{-16} , and the smallest allowable reported P value in GraphPad PRISM is 1×10^{-15} . When P values fall below these thresholds, the tools report a range (that is, $P < 2.2 \times 10^{-16}$ in R and $P < 1 \times 10^{-15}$ in GraphPad) rather than attempt to report a less precise or unreliable value.

Reporting summary

Further information on research design is available in the Nature Portfolio Reporting Summary linked to this article.

Data availability

All data needed to evaluate the conclusions in the paper are present in the paper and/or Supplemental Information. All raw and processed genomic data were deposited in the Gene Expression Omnibus (GEO) under accession [GSE199913](https://www.ncbi.nlm.nih.gov/datasets/genome/GCF_000001405.13/). All the genomic data were aligned to the human reference genome GRCh37/hg19 (https://www.ncbi.nlm.nih.gov/datasets/genome/GCF_000001405.13/). RIME data are available on ProteomeXchange with identifier [PXD031768](https://www.ebi.ac.uk/pride/archive/projects/PXD031768) (<https://www.ebi.ac.uk/pride/archive/projects/PXD031768>). The original mass spectra, spectral library and the protein sequence database used for searches have been deposited in the public proteomics repository MassIVE (identifier [MSV000096930](https://massive.ucsd.edu/v09/MSV000096930/); <http://massive.ucsd.edu>) and are accessible at <ftp://massive.ucsd.edu/v09/MSV000096930/>. The mRNA expression data and the clinical data of TCGA and METABRIC were downloaded from the TCGA data portal (<https://portal.gdc.cancer.gov>) and Synapse (Syn1688369), respectively. For TCGA, RNA-seq reads were reprocessed using Salmon (v0.14.1)⁸⁷ and log₂(transcripts per million + 1) values were used. For genes with multiple probes in METABRIC, probes with the highest IQR were selected to represent the gene. Copy number information of *KDM4C* from TCGA and METABRIC was downloaded from cBioPortal and predicted by the GISTIC algorithm⁸⁸. Gene copy number, subtype and RNA-seq (fragments per kilobase of transcript per million mapped read) for 57 breast cancer cell lines were downloaded from Cancer Cell Line Encyclopedia⁸⁹; copy number gain or deletion was defined as log₂ copy number above or below 1.2. AUCs for different chemotherapy drugs were downloaded from DepMap (<https://depmap.org/portal/>)⁵¹. Microarray data from five neoadjuvant therapy TNBC cohorts were downloaded from GEO with the following accessions: [GSE32646](https://www.ncbi.nlm.nih.gov/datasets/genome/GSE32646/), [GSE32603](https://www.ncbi.nlm.nih.gov/datasets/genome/GSE32603/), [GSE20194](https://www.ncbi.nlm.nih.gov/datasets/genome/GSE20194/), [GSE25066](https://www.ncbi.nlm.nih.gov/datasets/genome/GSE25066/) and [GSE18864](https://www.ncbi.nlm.nih.gov/datasets/genome/GSE18864/). log₂-Normalized probe intensities were used for signature enrichment analysis. The mRNA and normalized metabolomic profile data from the Fudan University Shanghai Cancer Center (FUSCC) cohort were downloaded from ref. 43 and GEO with the accession code [GSE118527](https://www.ncbi.nlm.nih.gov/datasets/genome/GSE118527/). For *KDM4C* ChIP-seq peak overlap analysis, publicly available H3K27ac ChIP-seq data were downloaded from GEO with the accession codes [GSE72956](https://www.ncbi.nlm.nih.gov/datasets/genome/GSE72956/) (HCC1954), [GSE57436](https://www.ncbi.nlm.nih.gov/datasets/genome/GSE57436/) (MCF7) and [GSE65201](https://www.ncbi.nlm.nih.gov/datasets/genome/GSE65201/) (T47D). H3K4me3 ChIP-seq data were downloaded from [GSE54693](https://www.ncbi.nlm.nih.gov/datasets/genome/GSE54693/) (MCF7) and [GSE80592](https://www.ncbi.nlm.nih.gov/datasets/genome/GSE80592/) (T47D). Source data are provided with this paper.

Code availability

This study does not report original code. All data were analyzed and processed using published software packages, the details of which are provided and cited in Methods.

References

- Balko, J. M. et al. Profiling of residual breast cancers after neoadjuvant chemotherapy identifies DUSP4 deficiency as a mechanism of drug resistance. *Nat. Med.* **18**, 1052–1059 (2012).
- Balko, J. M. et al. Triple-negative breast cancers with amplification of JAK2 at the 9p24 locus demonstrate JAK2-specific dependence. *Sci. Transl. Med.* **8**, 334ra53 (2016).

72. Geck, R. C. et al. Inhibition of the polyamine synthesis enzyme ornithine decarboxylase sensitizes triple-negative breast cancer cells to cytotoxic chemotherapy. *J. Biol. Chem.* **295**, 6263–6277 (2020).
73. Creech, A. L. et al. Building the connectivity map of epigenetics: chromatin profiling by quantitative targeted mass spectrometry. *Methods* **72**, 57–64 (2015).
74. Brademan, D. R., Riley, N. M., Kwiciecien, N. W. & Coon, J. J. Interactive peptide spectral annotator: a versatile web-based tool for proteomic applications. *Mol. Cell. Proteomics* **18**, S193–S201 (2019).
75. Peluffo, G. et al. EN1 is a transcriptional dependency in triple-negative breast cancer associated with brain metastasis. *Cancer Res.* **79**, 4173–4183 (2019).
76. Papachristou, E. K. et al. A quantitative mass spectrometry-based approach to monitor the dynamics of endogenous chromatin-associated protein complexes. *Nat. Commun.* **9**, 2311 (2018).
77. Ianevski, A., Giri, A. K. & Aittokallio, T. SynergyFinder 2.0: visual analytics of multi-drug combination synergies. *Nucleic Acids Res.* **48**, W488–W493 (2020).
78. Janiszewska, M. et al. Subclonal cooperation drives metastasis by modulating local and systemic immune microenvironments. *Nat. Cell Biol.* **21**, 879–888 (2019).
79. Mumbach, M. R. et al. Enhancer connectome in primary human cells identifies target genes of disease-associated DNA elements. *Nat. Genet.* **49**, 1602–1612 (2017).
80. Buenrostro, J. D., Wu, B., Chang, H. Y. & Greenleaf, W. J. ATAC-seq: a method for assaying chromatin accessibility genome-wide. *Curr. Protoc. Mol. Biol.* **109**, 21.29.1–21.29.9 (2015).
81. Cornwell, M. et al. VIPER: visualization pipeline for RNA-seq, a Snakemake workflow for efficient and complete RNA-seq analysis. *BMC Bioinformatics* **19**, 135 (2018).
82. Taing, L. et al. CHIPS: a Snakemake pipeline for quality control and reproducible processing of chromatin profiling data. *F1000Research* <https://doi.org/10.12688/f1000research.52878.1> (2021).
83. Servant, N. et al. HiC-Pro: an optimized and flexible pipeline for Hi-C data processing. *Genome Biol.* **16**, 259 (2015).
84. Langmead, B. & Salzberg, S. L. Fast gapped-read alignment with Bowtie 2. *Nat. Methods* **9**, 357–359 (2012).
85. Servant, N. et al. HiTC: exploration of high-throughput ‘C’ experiments. *Bioinformatics* **28**, 2843–2844 (2012).
86. Stansfield, J. C., Cresswell, K. G., Vladimirov, V. I. & Dozmorov, M. G. HiCcompare: an R-package for joint normalization and comparison of Hi-C datasets. *BMC Bioinformatics* **19**, 279 (2018).
87. Patro, R., Duggal, G., Love, M. I., Irizarry, R. A. & Kingsford, C. Salmon provides fast and bias-aware quantification of transcript expression. *Nat. Methods* **14**, 417–419 (2017).
88. Gao, J. et al. Integrative analysis of complex cancer genomics and clinical profiles using the cBioPortal. *Sci. Signal.* **6**, pl1 (2013).
89. Ghandi, M. et al. Next-generation characterization of the cancer cell line encyclopedia. *Nature* **569**, 503–508 (2019).
- GRHL2 and CTSL complex, respectively. We thank the DFCI Molecular Biology Core Facility for its outstanding sequencing service. We thank the N. Danial Lab (DFCI) for technical assistance and training for the seahorse assay. We thank A. Welm (University of Utah) for providing us with PDX samples. We thank the Bioinformatics Core at the Cancer Research UK Cambridge Institute for the analysis of the RIME data. This research was supported by the Department of Defense (W81XWH-14-1-0212 to A.M. and K.P.), the National Cancer Institute (NCI; R35 CA197623 to K.P. and P01CA250959 to K.P. and H.L.) and the Charles A. King Trust Postdoctoral Research Fellowship (to Z.L.). The content is solely the responsibility of the authors and does not necessarily represent the official views of the National Institutes of Health/NCI.

Author contributions

Z.L., G.P. and K.P. conceptualized the project. Z.L. and G.P. developed the methodology. Z.L., X.Q., K.C., S.B.E., L.E.S., M.P., D.T., M.E. and R.L. carried out formal analysis. Z.L., G.P., N.L.K., J.-H.S., S.B.E., K.E.E., E.P., C.S.D., M.S., X.-Y.H., J.N., M.G.R., M.M.R., J.A.R., A.T., S.R. and M.M. conducted the investigation. A.S., S.C.K., G.R., M.L.-N., D.J.M., A.J. and J.M.B. arranged the resources. Z.L., G.P. and K.P. wrote the original draft of the paper. A.M., F.M., J.S.C., J.D.J., M.L.F., H.W.L. and K.P. provided supervision. A.M., F.M., J.S.C., J.D.J., M.L.F., H.W.L. and K.P. secured funding. All authors contributed to the study design and participated in the writing, reviewing and editing of the paper.

Competing interests

K.P. serves on the Scientific Advisory Board of the Susan G. Komen Foundation, the V Foundation and Ideaya Biosciences; is an adviser to Curie.Bio; holds equity in Antares and stock options in Ideaya Biosciences; receives sponsored research funding from Novartis and received honoraria from AstraZeneca and sale of Scorpion Therapeutics stocks upon their acquisition by Eli Lilly in the past 12 months. F.M. is a cofounder of and has equity in Harbinger Health, has equity in Zephyr AI, and serves as a consultant for Harbinger Health, Zephyr AI and Red Cell Partners. F.M. declares that none of these relationships are directly or indirectly related to the content of this paper. L.E.S. and M.E. are current employees of AstraZeneca. M.L.-N. is a current employee of InSphero. D.J.M. is a current employee of Veralox Therapeutics. A.J. is a current employee of Pfizer. J.J. is a current employee of Odyssey Therapeutics. The other authors declare no competing interests.

Additional information

Extended data is available for this paper at <https://doi.org/10.1038/s41588-025-02197-z>.

Supplementary information The online version contains supplementary material available at <https://doi.org/10.1038/s41588-025-02197-z>.

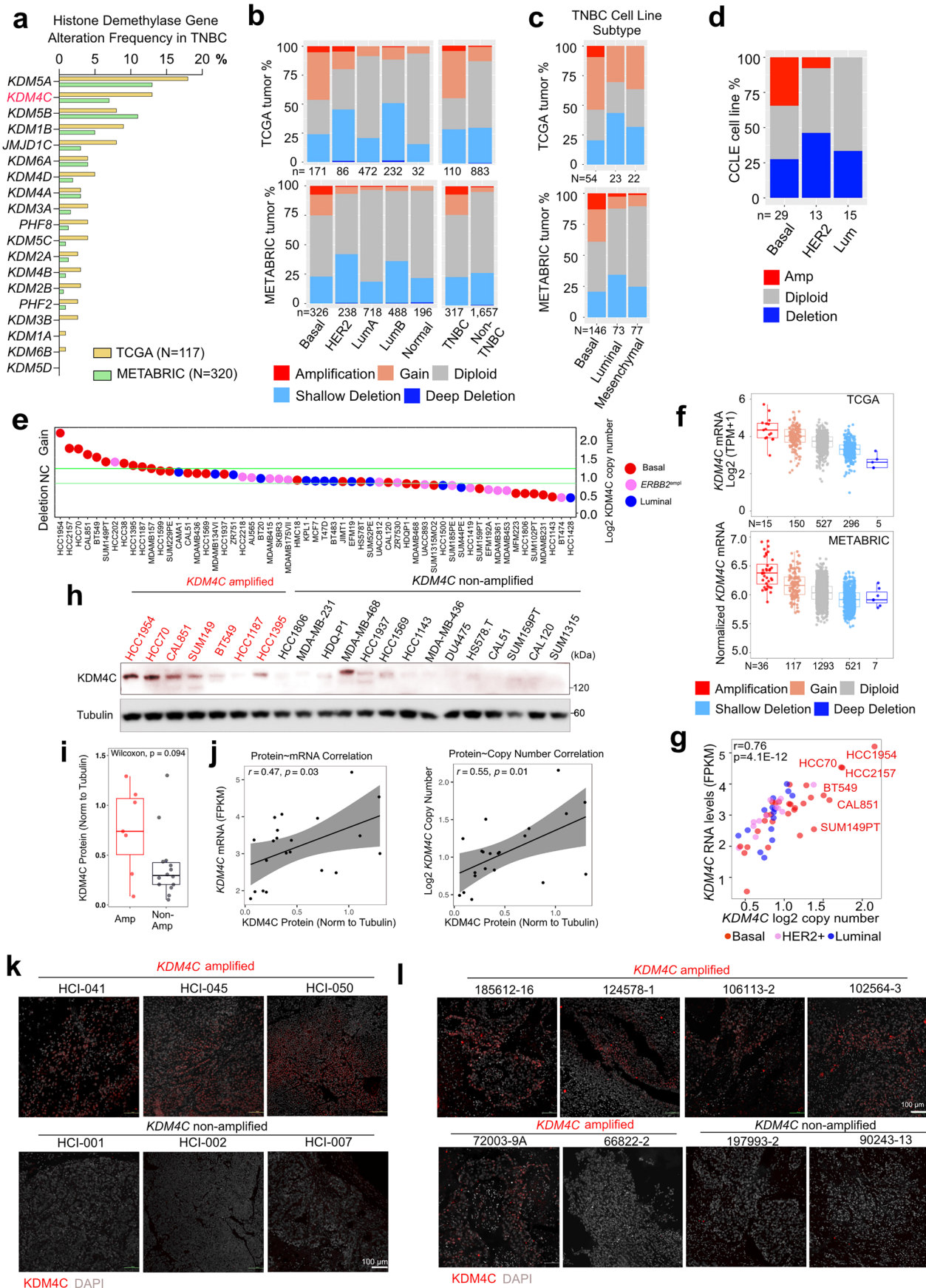
Correspondence and requests for materials should be addressed to Kornelia Polyak.

Peer review information *Nature Genetics* thanks Kristina Havas and the other, anonymous, reviewer(s) for their contribution to the peer review of this work.

Reprints and permissions information is available at www.nature.com/reprints.

Acknowledgements

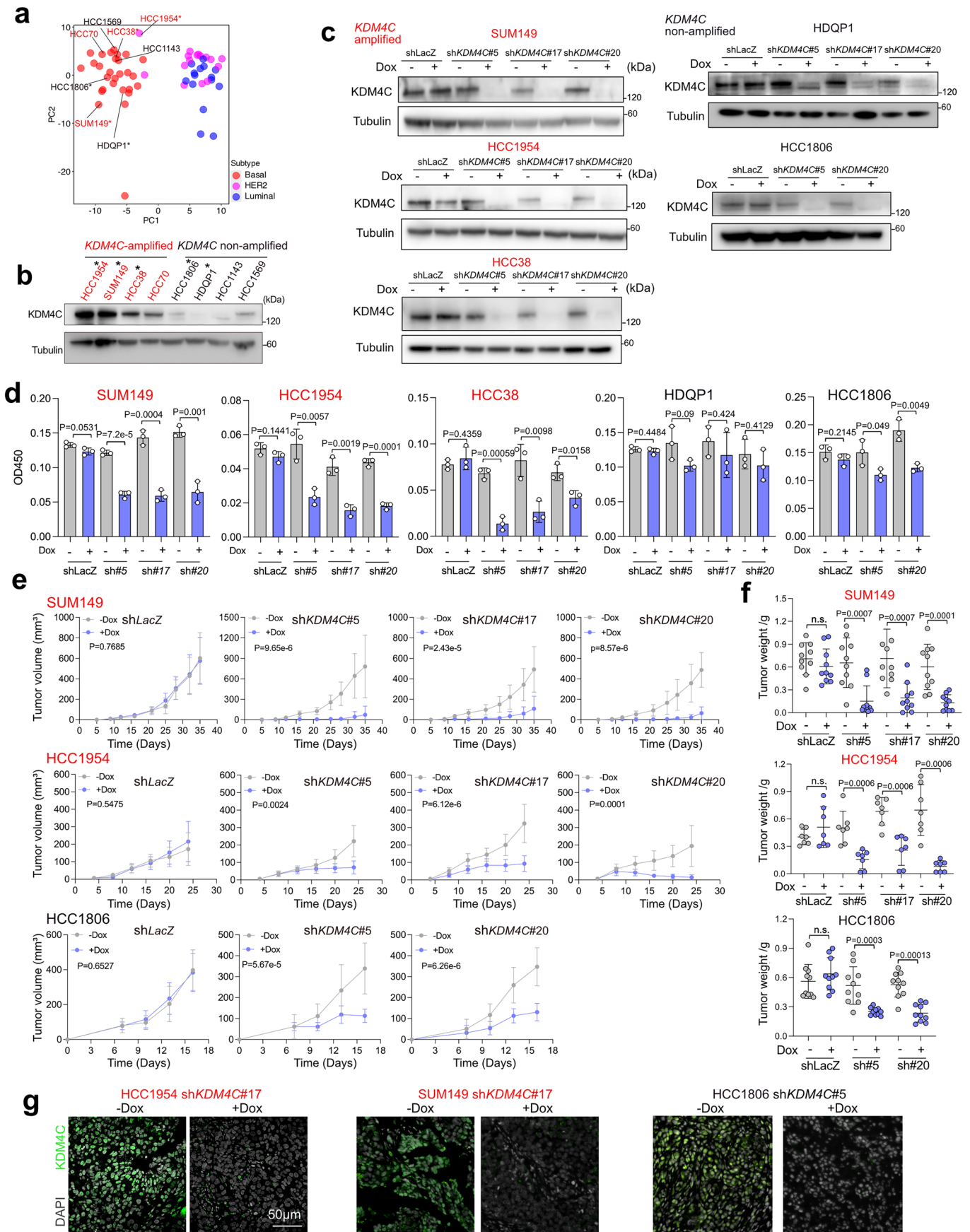
We thank members of our laboratories for their critical reading of this paper and useful discussions. We thank W. Kaelin (DFCI) and M. Eck (DFCI) for useful discussions on KDM4C and the structural biology of



Extended Data Fig. 1 | See next page for caption.

Extended Data Fig. 1 | *KDM4C* is frequently amplified in TNBC. **a**, Bar plot representing alteration frequencies of 19 genes encoding histone demethylases in TCGA and METABRIC TNBC tumors. **b**, Stacked bar plots showing *KDM4C* copy number alteration distribution across PAM50 subtypes in TCGA and METABRIC cohorts. **c**, Stacked bar plots showing *KDM4C* copy number alteration distribution across TNBC transcriptomic subtypes. **d**, Stacked bar plot depicting *KDM4C* copy number alteration distribution across 57 breast cancer cell lines. **e**, Dot plot showing \log_2 copy number value of *KDM4C* in 57 breast cancer cell lines from CCLE. Colors indicate tumor subtypes. NC indicates no changes. **f**, Box plots showing *KDM4C* mRNA expression in TCGA and METABRIC TNBC tumors grouped by copy number alteration types. **g**, Scatter plot illustrating correlation of *KDM4C* mRNA expression and \log_2 copy number in 57 breast cancer cell lines. Colors indicate subtype. R and p values were determined by two-sided Pearson correlation. **h**, Immunoblot showing *KDM4C* protein levels across 21 basal breast cancer cell lines with or without *KDM4C* amplification. Tubulin was

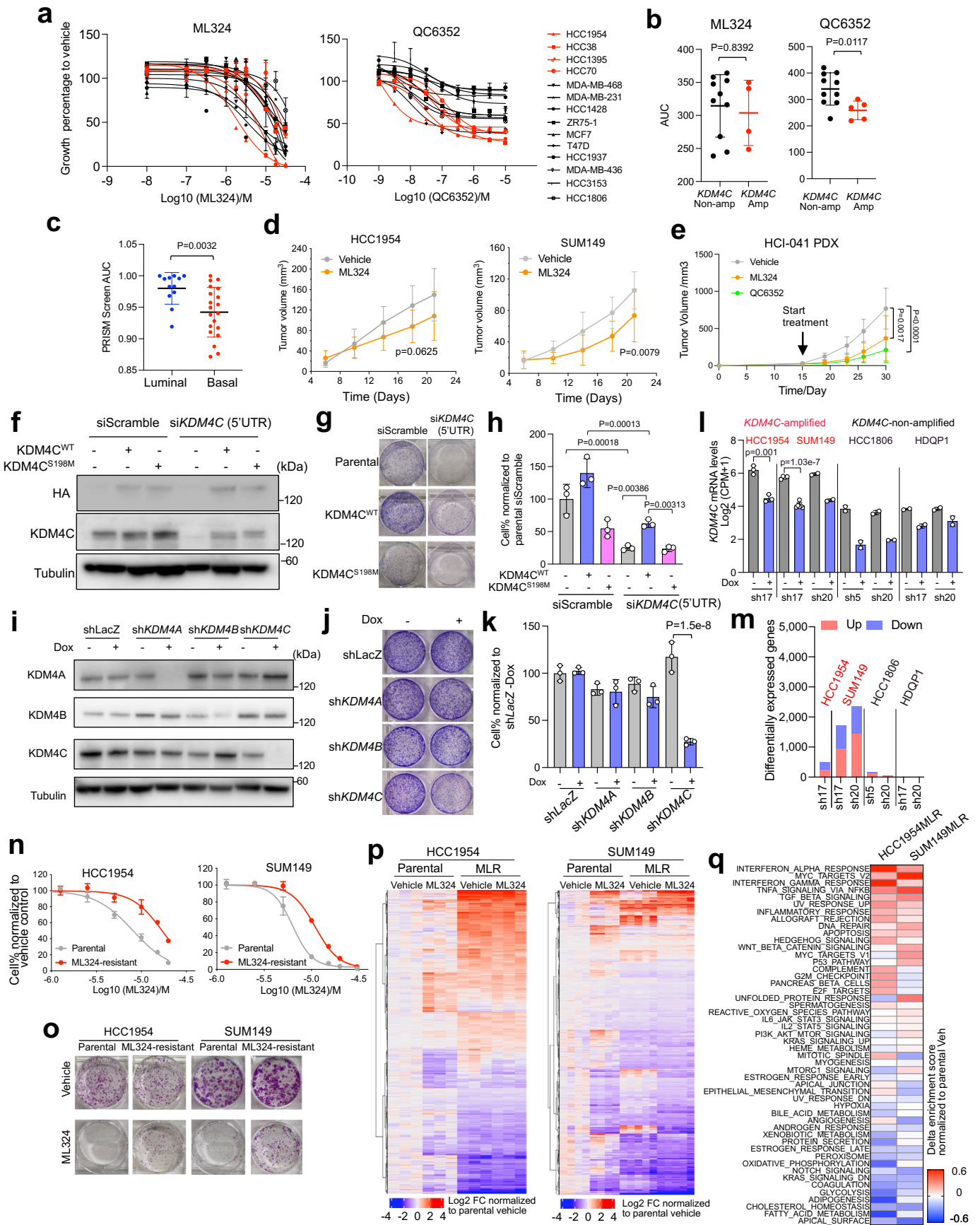
used as loading control. **i**, Box plot showing quantification of *KDM4C* protein levels normalized to tubulin from **h**. Each dot represents a cell line in **h** from $n = 7$ *KDM4C*-amplified and $n = 14$ *KDM4C* non-amplified basal breast cancer cell lines. Two-sided Mann–Whitney U test was used. **j**, Scatter plots depicting the correlation of *KDM4C* protein-to-mRNA and protein-to-copy number across all 21 cell lines in **h**. P and R values were calculated based on two-sided Pearson correlation. The linear regression lines with 95% confidence interval are shown. **k, l**, Representative images of immunofluorescence analysis of *KDM4C* expression in six PDX models (**k**) and eight primary TNBC clinical samples (**l**). Scale bar, 100 μm . *KDM4C* amplification status is indicated for each sample. Staining experiments for **k** and **l** have been performed once, while multiple regions were taken for each tissue. All box plots span the upper quartile (upper limit), median (center) and lower quartile (lower limit). Whiskers extend a maximum of $1.5 \times \text{IQR}$. Specific sample sizes are labeled for **b–d** and **f**.



Extended Data Fig. 2 | See next page for caption.

Extended Data Fig. 2 | *KDM4C* knockdown diminishes basal breast tumor growth. **a**, Principal component analysis plot showing the clustering of 59 breast cancer cell lines based on PAM50 gene expression panel profiled by CCLE. The names of the eight cell lines used in this study are indicated, and five of these, used for doxycycline-inducible sh*KDM4C* model engineering, are highlighted with an asterisk. **b**, Immunoblot analysis for *KDM4C* in four *KDM4C*-amplified and four non-amplified cell lines used in this study. Tubulin was used as a loading control. This experiment has been performed once. **c**, Immunoblot showing *KDM4C* protein levels in the doxycycline-inducible *KDM4C* knockdown models; 2–3 hairpins were used in each line. Tubulin was used as loading control. Longer exposure for HCC1806 and HDQP1 models was used, given their low baseline levels. All experiments were repeated twice with similar results, except HDQP1, which was done once. **d**, Bar plots depicting quantification of colony growth

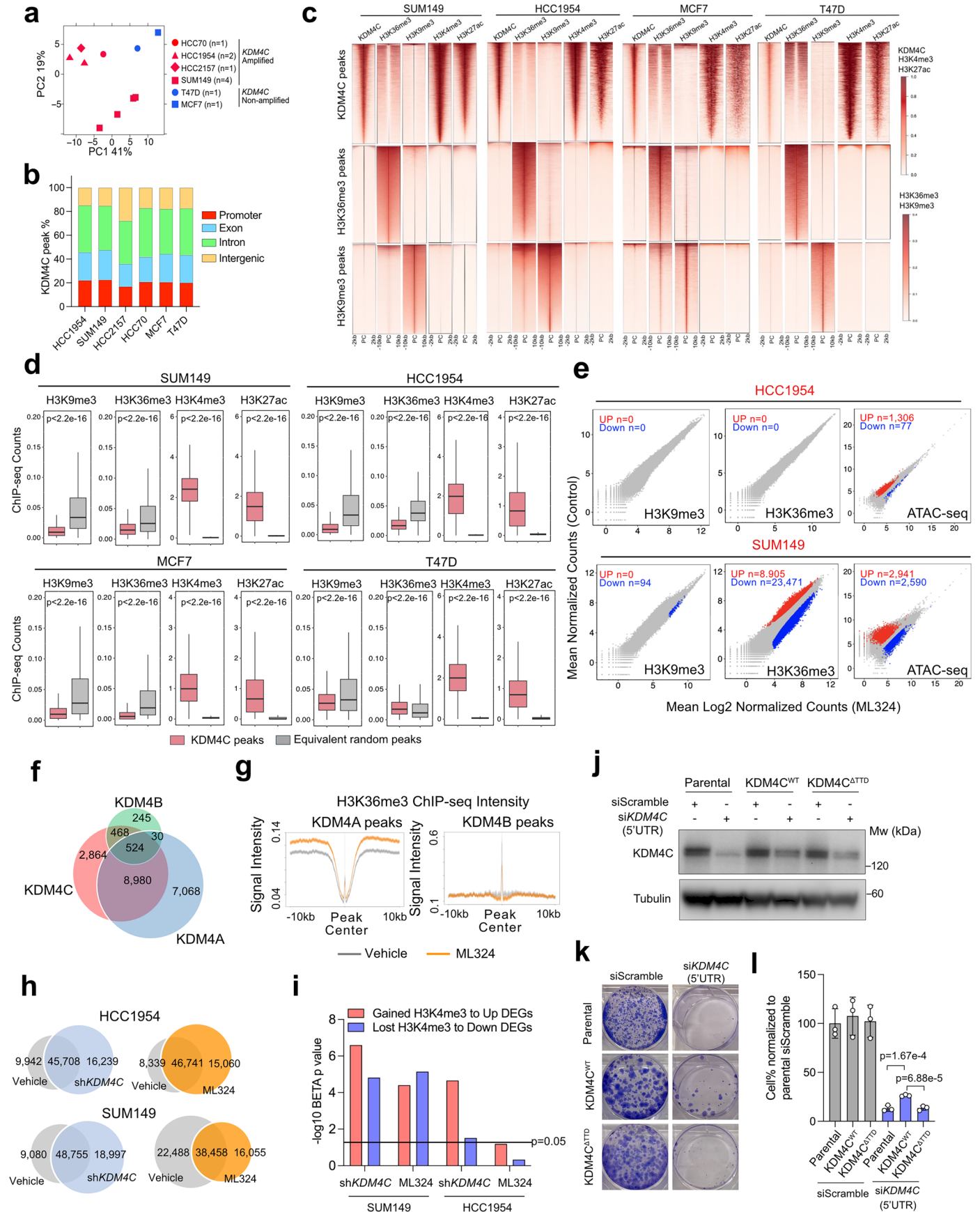
assays in the indicated models in the presence or absence of 1 µg/ml doxycycline. Data represent mean ± s.d. from n = 3 of a representative experiment from at least two independent trials with similar results. Two-sided ordinary one-way ANOVA was used in each cell line. **e**, Growth curves depicting tumor volumes of HCC1954, SUM149 and HCC1806 xenografts expressing sh*LacZ* or sh*KDM4C* Dox-inducible shRNA on control or doxycycline diet. Each dot represents mean ± s.d. of ten tumors per group. Two-sided repeated-measure two-way ANOVA was used for comparing tumor growth ratios within each model. **f**, Dot plots depicting tumor weights at endpoint. Data represent mean ± s.d. of seven (HCC1954) or ten (SUM149 and HCC1806) tumors per group. Two-sided Kruskal–Wallis test was used. **g**, Representative images of *KDM4C* immunofluorescence in HCC1954, SUM149 and HCC1806 xenografts in the presence or absence of doxycycline diet treatment. DAPI was used to stain nuclei. Scale bar, 50 µm.



Extended Data Fig. 3 | See next page for caption.

Extended Data Fig. 3 | Pharmacological and transcriptomic characterization of KDM4C blockade. **a**, Dose–response curve to ML324 and QC6352 in *KDM4C*-amplified (n = 5 for QC6352 and n = 4 for ML324) and non-amplified (n = 10) breast cancer cell lines (mean \pm s.d. with n = 6 from one experiment). **b**, Quantification of area under the curve (AUC) in **a** (two-sided Mann–Whitney U test). **c**, Dot plots showing PRISM screen-derived QC6352 AUC between luminal and (n = 12) and basal (n = 20) breast cancer cell lines (two-sided Mann–Whitney U test). **d,e**, Plots depicting tumor volume of HCC1954 and SUM149 xenografts (**d**) and HCl-041 PDX (**e**). Mean \pm s.d. from n = 10 (**d**) or n = 4–5 (**e**) tumors per group are shown (two-sided repeated-measure two-way ANOVA). **f,i**, Immunoblot for KDM4C and HA in SUM149 cells overexpressing HA-tagged *KDM4C*^{WT} and *KDM4C*^{S198M} with siRNA interference against *KDM4C* 5'UTR region for 3 days (**f**) and KDM4A/KDM4B/KDM4C from SUM149 Dox-inducible cell models with or without 1 μ g/ml doxycycline for 3 days (**i**) with tubulin was loading controls. (three (**f**) and two (**i**) independent repeats with similar results). **g,h**, Representative images (**g**) and quantification (**h**) of colony growth assay

with mean \pm s.d. from n = 3 of SUM149 parental and KDM4C overexpression models transfected with *KDM4C* 5'UTR siRNA. (two-sided ordinary one-way ANOVA and two independent repeats with similar results). **j,k**, Representative images (**j**) and quantification (**k**) of colony growth assay of SUM149-inducible cell models from one experiment (mean \pm s.d. with n = 3 and two-sided ordinary one-way ANOVA). **l**, Bar plot showing *KDM4C* mRNA levels from RNA-seq with mean \pm s.d. from n = 3 (HCC1954), n = 4 (SUM149 sh17 – Dox), n = 6 (SUM149 sh17 + Dox) and n = 2 (others; two-sided Student's t test for HCC1954 and SUM149 sh17 models). **m**, Stacked bar plot showing numbers of differentially expressed genes (DEGs). **n**, ML324 dose–response curves of parental and ML324-resistant (MLR) cells (mean \pm s.d. with n = 3). **o**, Representative images of colony growth assay in parental and MLR cells treated with or without 10 μ m ML324 for 2 weeks. **p**, Heatmaps showing the union of DEGs induced by ML324 or in MLR compared to parental cells normalized to the parental-vehicle controls. **q**, Heatmap depicting the alteration of the Hallmark signature enrichment scores in MLR models.

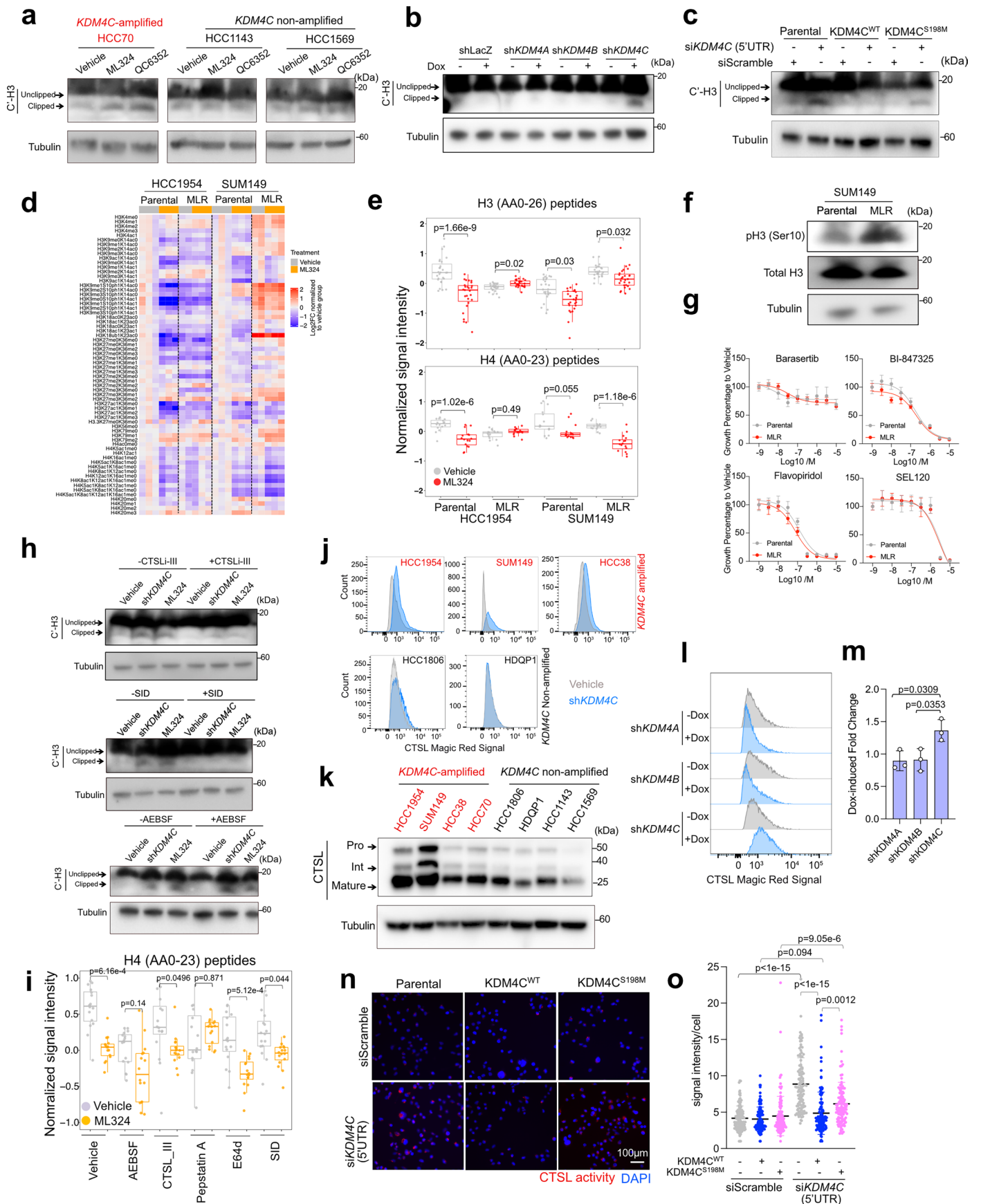


Extended Data Fig. 4 | See next page for caption.

Extended Data Fig. 4 | Chromatin alterations following KDM4C inhibition.

a, Principal component analysis of KDM4C peaks in the indicated cell lines. **b**, Stacked bar plots showing the distribution of KDM4C peaks in the indicated cell lines in distinct genomic regions. **c**, Heatmap illustrating CHIP-seq peaks for the indicated marks and cell lines. Windows of peak center with ± 2 kb or ± 10 kb are shown. **d**, Box plots showing the CHIP-seq read counts for the indicated histone mark projected on KDM4C peaks or the equivalent number of random peaks (HCC1954, $n = 21,768$; SUM149, $n = 19,675$; MCF7, $n = 18,160$; T47D, $n = 19,244$). Box plots span the upper quartile (upper limit), median (center) and lower quartile (lower limit). Whiskers extend a maximum of $1.5 \times$ IQR (two-sided Mann-Whitney U test). **e**, Scatter plots representing the \log_2 -normalized counts of H3K9me3 and H3K36me3 CHIP-seq (5 kb bin) and merged ATAC-seq peaks between controls and ML324-treated groups in two cell lines. Numbers of differential regions are indicated. **f**, Venn diagram showing the intersection of KDM4A, KDM4B and KDM4C CHIP-seq peaks in the SUM149 cell line. **g**, Plot depicting H3K36me3 CHIP-seq signal in the presence or absence of ML324

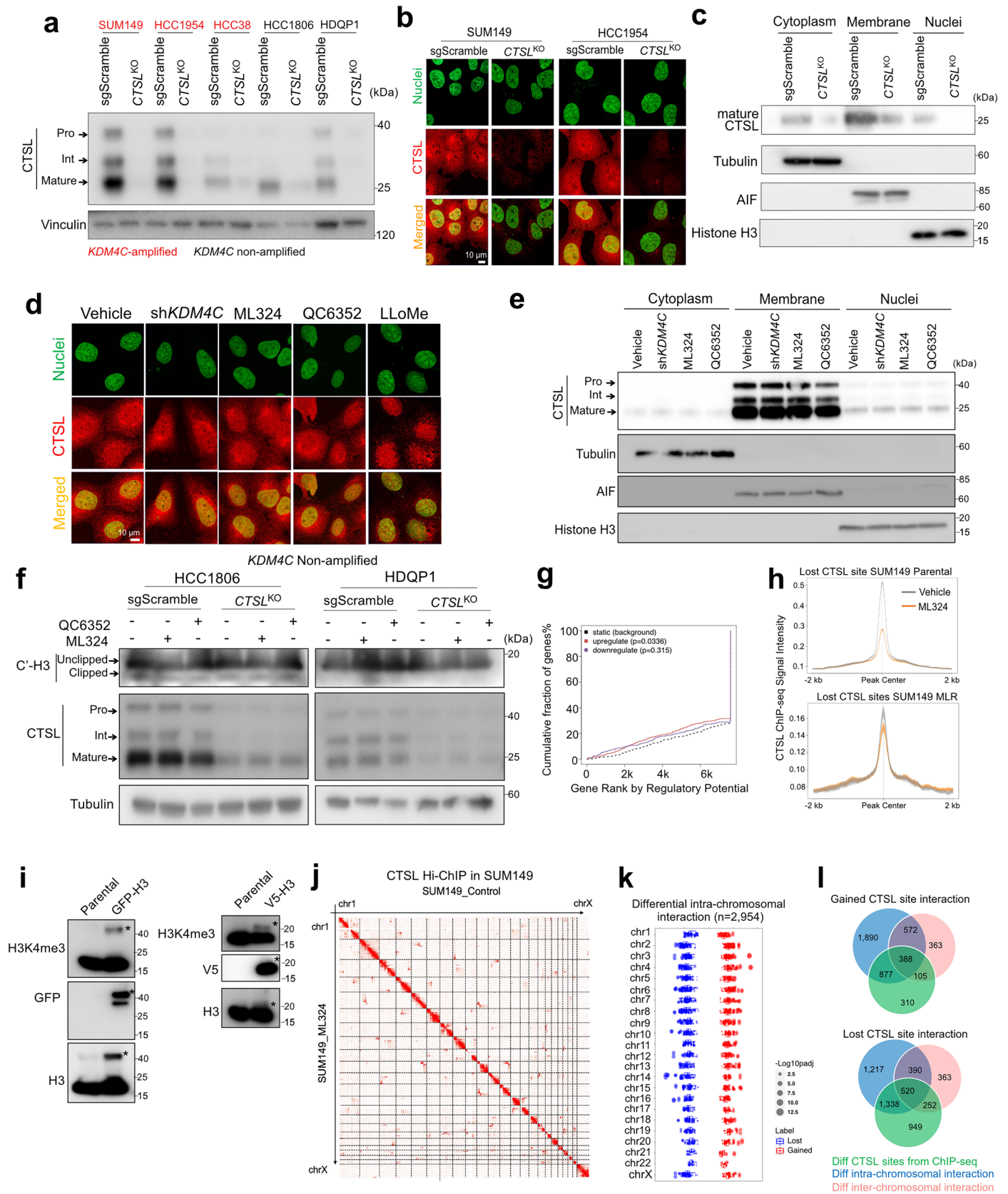
treatment at KDM4A or KDM4B peaks. Windows of peak center with ± 10 kb are shown. The 95% confidence interval of each curve is presented. **h**, Venn diagrams showing intersections of H3K4me3 peaks between vehicle and shKDM4C or ML324-treated groups in two cell lines. **i**, Bar plots showing $-\log_{10}(p)$ calculated by the BETA algorithm representing the association of differential H3K4me3 peaks with differentially expressed genes from RNA-seq in the indicated contexts. **j**, Immunoblot analysis for KDM4C in cell lysates of SUM149 cells with or without KDM4C^{WT} or KDM4C^{ΔTTD} overexpressing with 5'UTR region siRNA interference for 3 days. Tubulin was used as loading control. This experiment was repeated independently three times with similar results. **k, l**, Representative images (**k**) and quantification (**l**) of colony growth assay of SUM149 parental and KDM4C^{WT} or KDM4C^{ΔTTD} mutant overexpression models transfected with siRNA against *KDM4C* 5'UTR region. Data are presented as mean \pm s.d. with $n = 3$ normalized to parental with siScramble group from a representative experiment from three independent repeats with similar results (two-sided ordinary one-way ANOVA).



Extended Data Fig. 5 | See next page for caption.

Extended Data Fig. 5 | KDM4C inhibition induces proteolytic cleavage of histone tails. a–c, Immunoblot for C'-H3 in three cell lines following DMSO, 10 μM ML324 or 1 μM QC6352 treatment for 5 days (**a**), SUM149 doxycycline-inducible models with or without 1 $\mu\text{g}/\text{ml}$ doxycycline for 5 days (**b**) and SUM149 cells overexpressing KDM4C^{WT} and KDM4C^{S198M} with siRNA against *KDM4C* 5'UTR for 5 days (**c**; two independent repeats for all with similar results). **d,** Heatmap showing normalized histone peptide abundance in parental and MLR models with or without ML324 treatment. **e,i,** Box plots showing average N-terminal peptides abundances of histone H3 ($n = 27$ peptides) or H4 ($n = 16$ peptides) in the indicated groups (two-sided Kruskal–Wallis test). Box plots span the upper quartile (upper limit), median (center) and lower quartile (lower limit). Whiskers extend a maximum of $1.5 \times \text{IQR}$. **f,** Immunoblot for total and phospho-histone H3 (Ser10) in SUM149 parental and MLR cells (two independent repeats with similar results). **g,** Cell viability curves normalized to vehicle group in response to CDK8 or AURKA/AURKB inhibitors in SUM149 parental and MLR cells (mean \pm s.d. of $n = 6$ from one experiment). **h,** Immunoblot for C'-H3 in SUM149-inducible-

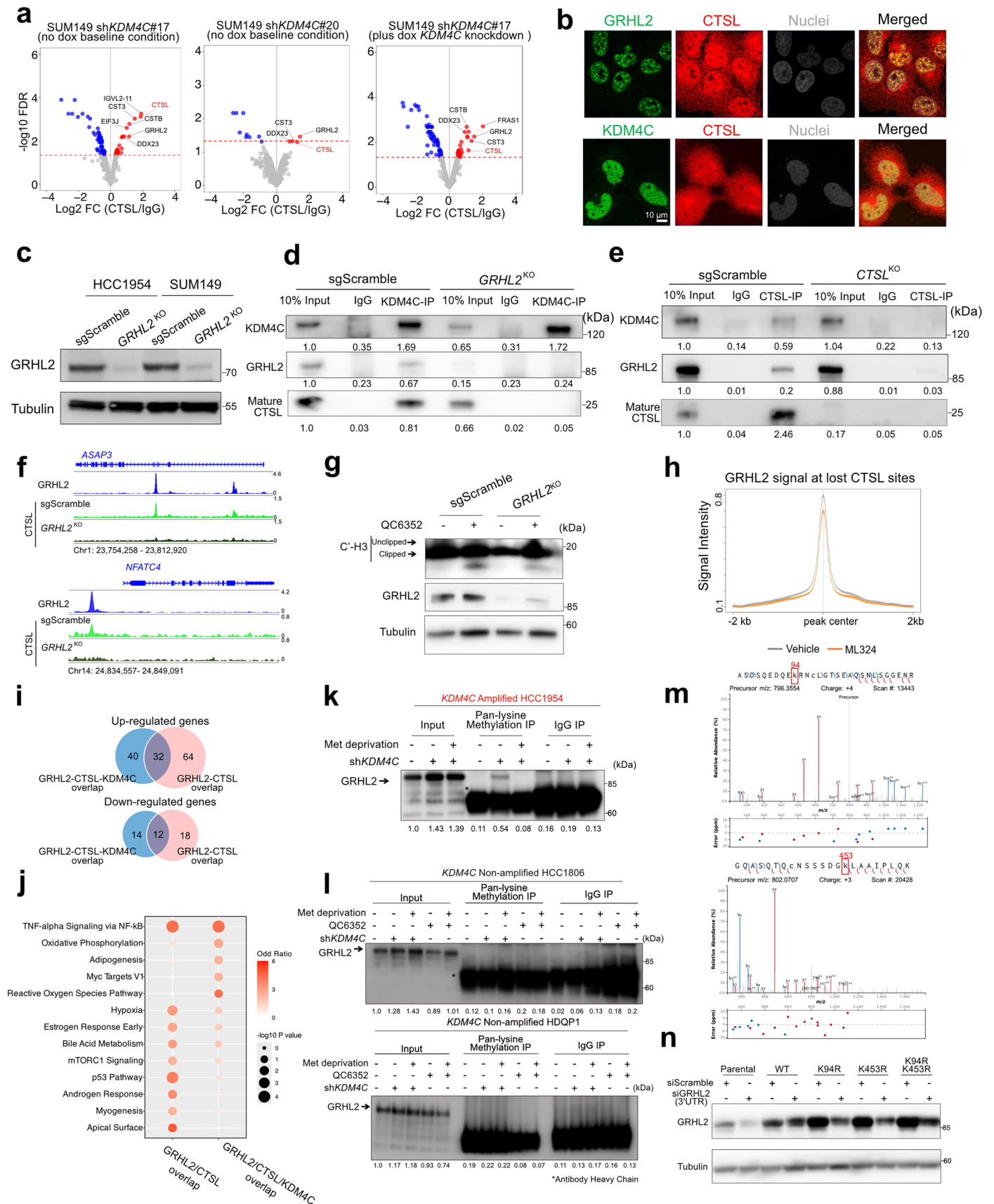
sh*KDM4C* cells with either 1 $\mu\text{g}/\text{ml}$ doxycycline or 10 μM ML324 with different protease inhibitors (5 μM CTSL-inhibitor III, 10 μM SID2668150 or 100 μM AEBSF), with tubulin as loading control (three independent repeats for CTSLi-III experiment with similar results and one experiment for the rest). **j,** Representative plots depicting the CTSL activity signal in the indicated sh*KDM4C* cell models with 1 $\mu\text{g}/\text{ml}$ doxycycline treatment for 5 days. **k,** Immunoblot analysis for CTSL in the indicated cell lines from one experiment. **l,m** Representative plot (**l**) and quantification of mean \pm s.d. from three independent experiments (**m**) of indicated SUM149 models with or without 1 $\mu\text{g}/\text{ml}$ doxycycline for 5 days (two-sided ordinary one-way ANOVA). **n,o,** Representative images of CTSL activity signal in SUM149 cells overexpressing KDM4C^{WT} and KDM4C^{S198M} with siRNA interference against *KDM4C* 5'UTR for 5 days (**n**) and quantification of signals of 120 cells from three to four representative regions in mean \pm s.d. (two-sided ordinary one-way ANOVA; **o**). Scale bar, 100 μm . Tubulin was used as loading control for all the immunoblots.



Extended Data Fig. 6 | See next page for caption.

Extended Data Fig. 6 | CTSL is a chromatin-bound histone H3 protease activated by KDM4C inhibition. **a**, Immunoblot depicting CTSL in sgScramble and *CTSL*^{KO} models in the indicated cell lines with vinculin as a loading control (two independent repeats with similar results). **b**, Immunofluorescence staining of CTSL and nuclei in the corresponding sgScramble and *CTSL*^{KO} derivatives from one experiment. Scale bar, 10 μ m. **c**, Immunoblot depicting CTSL in different fractions in SUM149 sgScramble and *CTSL*^{KO} derivatives with tubulin, AIF and histone H3 as controls for subcellular fractionation (two independent repeats with similar results). **d**, Immunofluorescence for CTSL and nuclei in SUM149-inducible-sh*KDM4C* cells treated with DMSO, 1 μ g/ml doxycycline (sh*KDM4C*), 10 μ m ML324 or 1 μ m QC6352 for 3 days from one experiment. Treatment of 1 μ m LLoMe for 24 h was a positive control. Scale bar, 10 μ m. **e**, Immunoblot for CTSL in the indicated fractions of SUM149-inducible-sh*KDM4C* cells under the same treatment as **d** for 5 days (three independent repeats with similar results). **f**, Immunoblot showing C'-H3 and CTSL in HCC1806 and HDQP1 sgScramble and *CTSL*^{KO} derivatives with 10 μ m ML324 or 1 μ m QC6352 treatment for 5 days with tubulin as loading control (two independent repeats with similar results).

g, Binding and Expression Target Analysis showing association between ML324-induced gained CTSL sites and differentially expressed genes in SUM149 cells (one-sided Kolmogorov–Smirnov test). **h**, Intensity plots depicting CTSL ChIP-seq signal in vehicle and ML324-treated SUM149 parental and MLR cells at lost CTSL sites at \pm 2 kb range of the peak centers. The 95% confidence interval is presented. **i**, Immunoblot showing H3K4me3, total H3 levels in SUM149 cells ectopically expressing GFP- (left) and V5-tagged (right) histone H3 from one experiment. Ectopic proteins were differentiated by molecular weight and indicated by an asterisk. **j**, Heatmap showing intrachromosomal and interchromosomal CTSL interactions in SUM149 cells with vehicle or ML324 treatment. **k**, Box plot showing ML324-induced differential intrachromosomal CTSL interactions with frequency >10 and adjusted p value < 0.05. Box plots span the upper quartile (upper limit), median (center) and lower quartile (lower limit). Whiskers extend a maximum of 1.5 \times IQR. **l**, Venn diagrams showing intersections among ML324-induced gained or lost CTSL binding sites in ChIP-seq and intrachromosomal or interchromosomal interaction sites in Hi-ChIP.



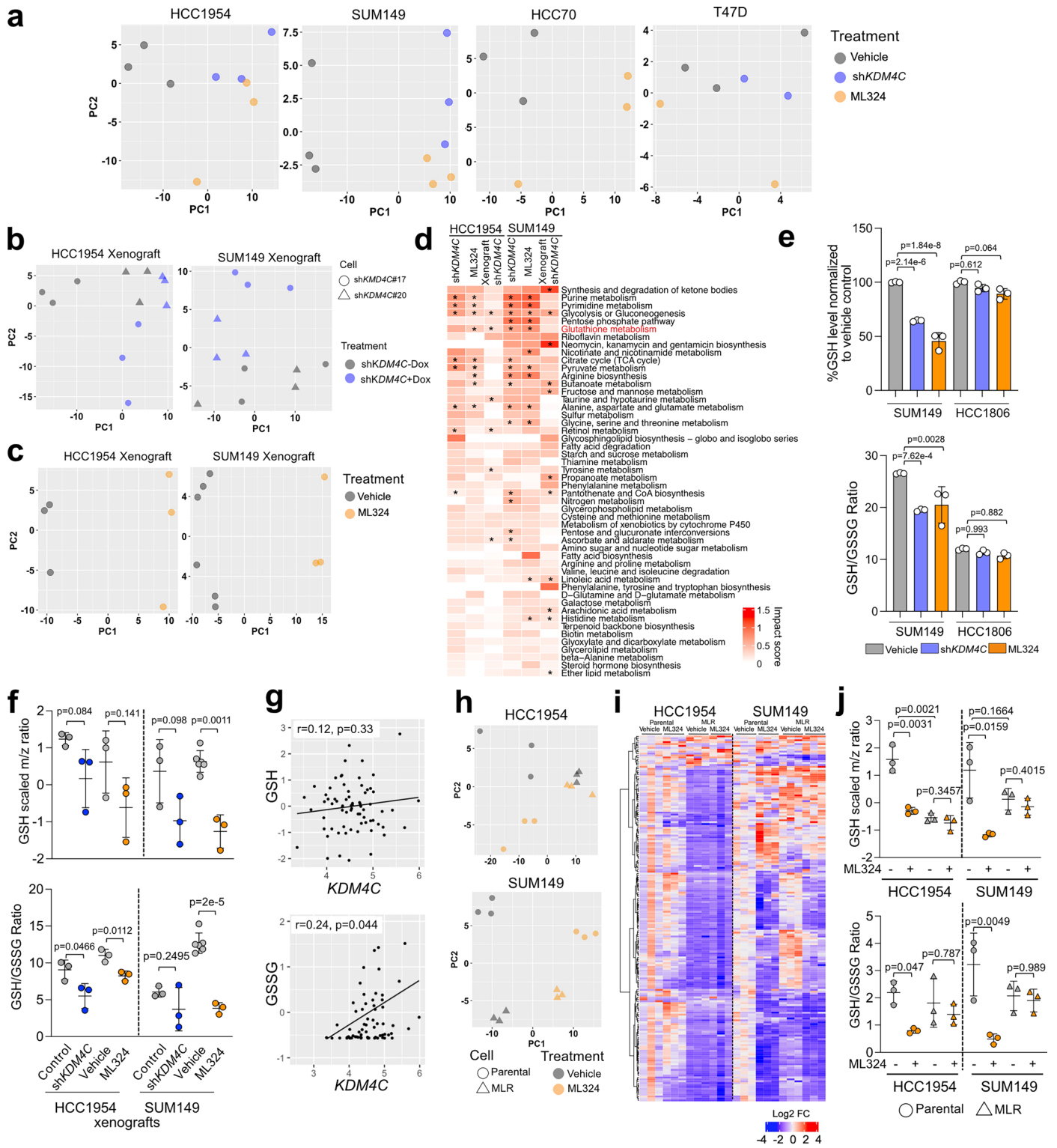
Extended Data Fig. 7 | See next page for caption.

Extended Data Fig. 7 | Regulation of CTSL chromatin binding and activity by GRHL2.

a, Volcano plots showing CTSL-interacting proteins in SUM149 sh*KDM4C* models (17 and 20 without doxycycline and 17 with doxycycline treatment) identified by mass spectrometry of CTSL immunoprecipitants. Red and blue indicate targets with FDR < 0.05 compared to IgG control. **b**, Immunofluorescence staining of CTSL (red), nuclei (gray) and GRHL2 or KDM4C (green) in SUM149 cell line from one experiment. Scale bar, 10 μ m. **c**, Immunoblot depicting the expression of GRHL2 in HCC1954 and SUM149 sgScramble and *GRHL2*^{ko} derivatives with tubulin as a loading control (two independent repeats with similar results). **d, e**, Immunoblot for KDM4C, GRHL2 and CTSL in the indicated immunoprecipitants of KDM4C in SUM149 *GRHL2*^{ko} (**d**) and CTSL in *CTSL*^{ko} (**e**) derivatives for one experiment. **f**, Genomic track view of GRHL2 (in parental cells) and CTSL ChIP-seq signal in SUM149 sgScramble and *GRHL2*^{ko} models at the *ASAP3* and *NFATC4* loci. **g**, Immunoblot for C'-H3 and GRHL2 of SUM149 sgScramble and *GRHL2*^{ko} models following 1 μ M of QC6352 treatment for 5 days with tubulin as a loading control (two independent repeats with similar results). **h**, Intensity plot depicting GRHL2 ChIP-seq

signal in vehicle and ML324-treated SUM149 cells on lost CTSL binding sites.

i, Venn diagram showing the intersection of upregulated or downregulated differentially expressed genes associated with triple (KDM4C + GRHL2 + CTSL) and double (GRHL2 + CTSL) overlap peaks. **j**, Dot plot depicting Hallmark signature enrichment predicted from top 300 triple (KDM4C + GRHL2 + CTSL) and double (GRHL2 + CTSL) overlap peaks-associated genes. (Fisher's exact test using Enrichr). **k, l**, Immunoblot for GRHL2 in 10% input and immunoprecipitants of pan-lysine methylation and IgG antibody in *KDM4C*-amplified HCC1954 (**k**) and *KDM4C* non-amplified HCC1806 and HDQP1 cells (**l**) grown in the indicated conditions from one experiment. **m**, Annotated mass spectra for methylated lysine 94 and 453. Lowercase amino acids indicate these are modified (**c** is alkylated cysteine, and **k** is monomethylated lysine). **n**, Immunoblot of GRHL2 in SUM149 cells following 3 days of siRNA transfection targeting the 3'UTR region of GRHL2, following 3 days of WT or mutant GRHL2 lentiviral infection (two independent repeats with similar results). Target proteins from IP experiments were quantified by normalizing to the corresponding input and labeled below each band.

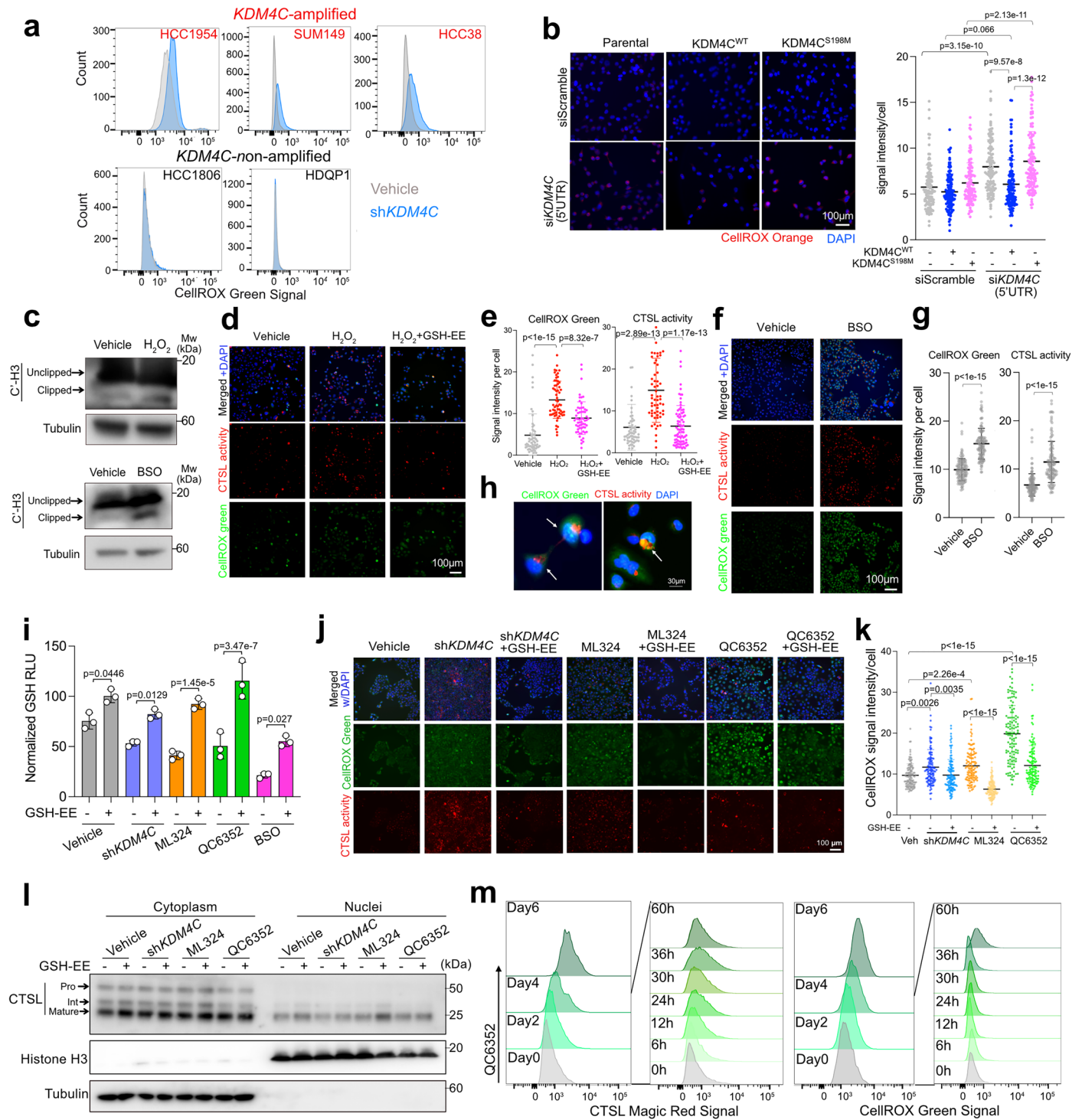


Extended Data Fig. 8 | See next page for caption.

Extended Data Fig. 8 | KDM4C-blockade-induced metabolic alteration.

a–c. Principal component analysis plots of metabolomic profiles of the indicated doxycycline-inducible *shKDM4C* models treated with vehicle (DMSO, no doxycycline), 0.1 $\mu\text{g/ml}$ doxycycline (Dox) or 10 μm ML324 (no doxycycline) for 5 days (**a**), HCC1954 and SUM149 doxycycline-inducible *shKDM4C* cells-derived xenografts with regular (–Dox) or doxycycline (+Dox) diets (**b**) or vehicle and ML324 treatments (**c**). **d.** Heatmap illustrating the impact scores of metabolic pathways significantly altered by doxycycline (*shKDM4C*) or ML324 treatment after integration of metabolomics and RNA-seq data in cell lines or in tumors. Metabolic pathways were ranked starting from the strongest consistent impact (asterisk: pathways with p value < 0.05). **e.** Bar plots showing intracellular GSH levels and GSH/GSSG ratio in SUM149 and HCC1806 inducible-*shKDM4C*-expressing cell models treated vehicle (DMSO), 1 $\mu\text{g/ml}$ doxycycline or 10 μm ML324 for 2 days. Data are presented as mean \pm s.d. from $n = 3$ from one experiment (two-sided ordinary one-way ANOVA). **f.** Dot plot showing GSH levels and GSH/GSSG ratio measured by mass spectrometry in HCC1954 and

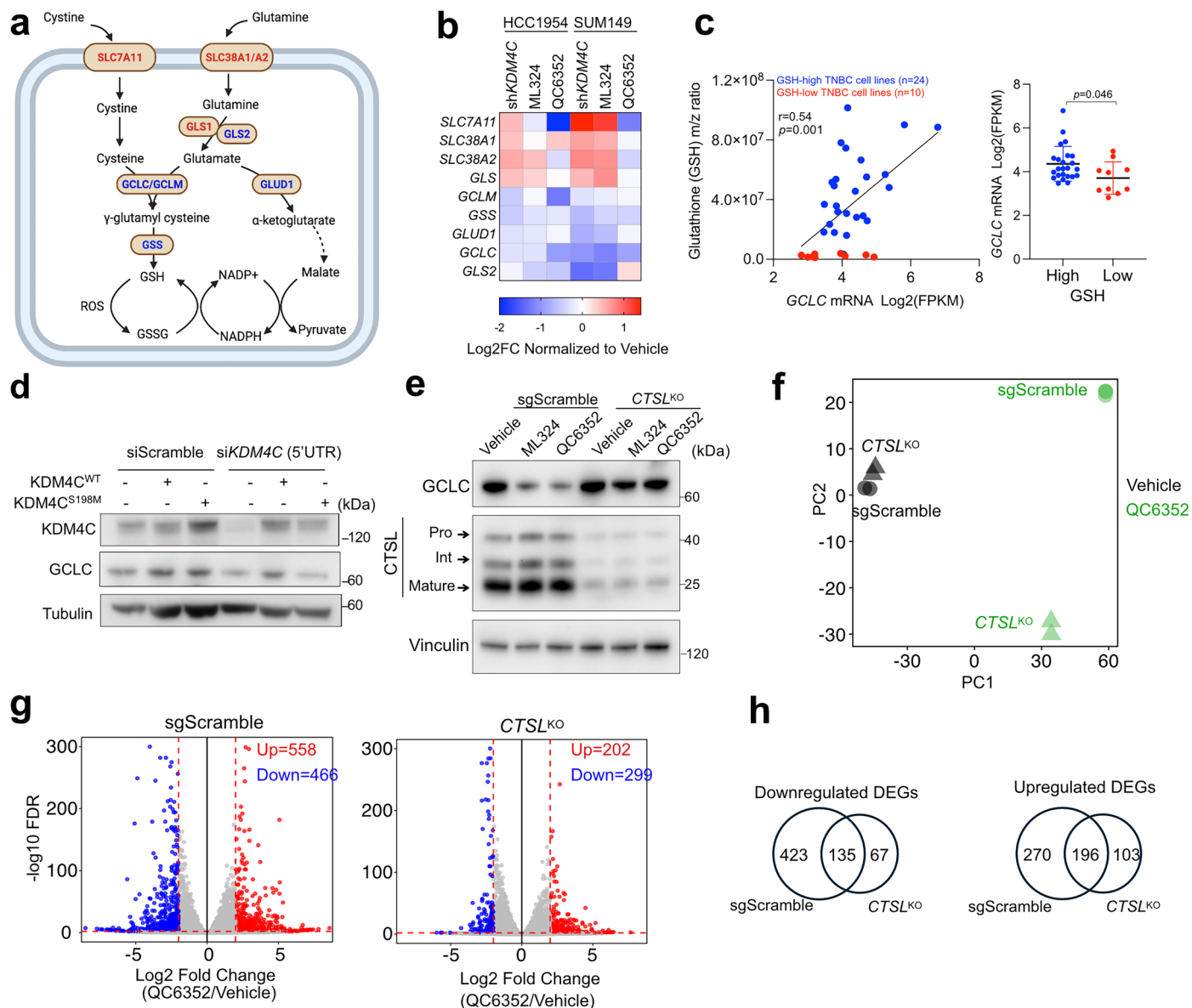
SUM149-inducible *shKDM4C* model-derived xenografts from mice fed regular (control) or doxycycline diets (*shKDM4C*) or treated with vehicle or ML324. Data represent mean \pm s.d. with $n = 6$ tumors (SUM149 vehicle group) or $n = 3$ tumors for all the other groups (two-sided Student's t test). **g.** Scatter plot representing correlations between *KDM4C* mRNA expression and GSH or GSSG abundance in 72 TNBC tumors profiled in the FUSCC cohort⁴⁴. R and p values were derived from two-sided Pearson correlation. **h, i.** Principal component analysis plots (**h**) and a heatmap of unsupervised clustering of 248 polar metabolites (**i**) of metabolomic profiles of HCC1954 and SUM149 parental or ML324-resistant (MLR) models treated with DMSO or 10 μm ML324 for 5 days. Metabolite abundances in each condition were normalized to the mean value of vehicle group of each parental cell line. **j.** Dot plots depicting the GSH levels and GSH/GSSG ratio measured by mass spectrometry in HCC1954 and SUM149 parental or MLR models treated with DMSO or 10 μm ML324 for 5 days. Data represent mean \pm s.d. of $n = 3$ biological replicates per group (two-sided ordinary one-way ANOVA).



Extended Data Fig. 9 | See next page for caption.

Extended Data Fig. 9 | KDM4C-blockade-induced redox imbalance aids histone clipping. **a**, Plots showing the CellROX green signal of five inducible-sh*KDM4C* models treated with or without 1 $\mu\text{g}/\text{ml}$ doxycycline for 5 days. **b**, Representative images (left) and quantification (right) of CellROX orange signal in SUM149 cells overexpressing *KDM4C*^{WT} and *KDM4C*^{S198M} with siRNA against *KDM4C* 5'UTR for 5 days. Mean \pm s.d. of 120 cells from three to four representative regions are shown (two-sided ordinary one-way ANOVA). Scale bar, 100 μm . **c**, Immunoblot for C'-H3 from SUM149 cells treated with 0.5 mM H_2O_2 for 1 day (top) or 1 μM BSO for 3 days (bottom; two (BSO) and three (H_2O_2) independent repeats with similar results). **d, f**, Representative images of CTSL activity and CellROX green signal in SUM149 cells treated with water, 0.5 mM H_2O_2 with or without 2 mM GSH-EE for 1 day (**d**) or 1 μM BSO for 3 days (**f**). Scale bar, 100 μm . **e, g**, Quantification of **d** and **f**. Mean \pm s.d. are shown from 60 (**e**) or 120 (**g**) cells from three representative regions of each condition (two-sided ordinary one-way ANOVA for **e** and Student's *t* test for **g**). **h**, Magnified images

of H_2O_2 -treated SUM149 cells. Overlapped CTSL and ROS nuclei signals are highlighted. Scale bar, 30 μm . **i**, Bar plot showing intracellular GSH levels in inducible-sh*KDM4C* SUM149 cells with DMSO, 1 $\mu\text{g}/\text{ml}$ doxycycline (sh*KDM4C*), 10 μM ML324 or 1 μM QC6352 with or without 2 mM GSH-EE for 2 days normalized to the corresponding cell numbers. Mean \pm s.d. are shown from $n = 3$ from one experiment (two-sided ordinary one-way ANOVA). **j**, Representative images of CTSL activity and CellROX green signal under the same conditions as **i** for 5 days. Scale bar, 100 μm . **k**, Mean \pm s.d. are shown for ROS signal of 120 cells from three representative regions (two-sided ordinary one-way ANOVA). **l**, Immunoblot of CTSL isoforms in different fractions of SUM149 cells under the same conditions as **i** for 5 days with tubulin and histone H3 as loading controls (three independent repeats with similar results). **m**, Plots showing CTSL activity and CellROX green signals in SUM149 cells treated with 1 μM QC6352 for the indicated time. Representative experiment from three independent repeats is shown.



Extended Data Fig. 10 | KDM4C suppression triggers redox imbalance via decreasing *GCLC*. **a**, Schematic view of glutathione synthesis pathway. Enzymes or transporters analyzed in **b** are indicated with red and blue representing increase and decrease upon KDM4C blockade, respectively. **b**, Heatmap showing fold change in expression of nine key enzymes or transporters involved in glutathione biosynthesis in HCC1954 and SUM149 Dox-inducible shKDM4C cell lines following treatment with 0.1 μg/ml doxycycline (Dox), 10 μM ML324 or 1 μM QC6352 for 5 days. Gene expression was normalized to the corresponding vehicle controls. **c**, Left: scatter plots showing the correlation of *GCLC* expression with GSH abundance from 34 TNBC cell lines. R and p values were derived from two-sided Pearson correlation. Right: dot plot depicting mean \pm s.d. of *GCLC* expression ($\log_2(\text{FPKM})$) in GSH-high ($n=24$) and GSH-low ($n=10$) TNBC cell lines (two-sided Mann–Whitney U test). **d**, Immunoblot for KDM4C and GCLC in SUM149 cells overexpressing KDM4C^{WT} and KDM4C^{S198M} with siRNA against

KDM4C 5'UTR for 3 days with tubulin as a loading control (two independent repeats with similar results). **e**, Immunoblots showing CTSL and GCLC protein levels in SUM149 sgScramble and CTSL^{KO} cell lines treated with or without 10 μM ML324 or 1 μM QC6352 for 5 days, with vinculin as a loading control (three independent repeats with similar results). **f**, Principal component analysis plot of RNA-seq profiles of SUM149 sgScramble and CTSL^{KO} models treated with DMSO (vehicle) or 1 μM QC6352 for 3 days. **g**, Volcano plots showing QC6352-induced differentially expressed genes in SUM149 sgScramble and CTSL^{KO} models. DEGs were selected with adjusted $p < 0.05$ and $\log_2(\text{FC}) > 2$, and specific numbers were labeled on the plots. FDR values were calculated by the Wald test following Benjamini–Hochberg correction using DESeq2. **h**, Venn diagram illustrating the overlap of upregulated and downregulated DEGs induced by QC6352 in SUM149 sgScramble and CTSL^{KO} models.

Reporting Summary

Nature Portfolio wishes to improve the reproducibility of the work that we publish. This form provides structure for consistency and transparency in reporting. For further information on Nature Portfolio policies, see our [Editorial Policies](#) and the [Editorial Policy Checklist](#).

Statistics

For all statistical analyses, confirm that the following items are present in the figure legend, table legend, main text, or Methods section.

- | | |
|-------------------------------------|--|
| n/a | Confirmed |
| <input type="checkbox"/> | <input checked="" type="checkbox"/> The exact sample size (n) for each experimental group/condition, given as a discrete number and unit of measurement |
| <input type="checkbox"/> | <input checked="" type="checkbox"/> A statement on whether measurements were taken from distinct samples or whether the same sample was measured repeatedly |
| <input type="checkbox"/> | <input checked="" type="checkbox"/> The statistical test(s) used AND whether they are one- or two-sided
<i>Only common tests should be described solely by name; describe more complex techniques in the Methods section.</i> |
| <input type="checkbox"/> | <input checked="" type="checkbox"/> A description of all covariates tested |
| <input type="checkbox"/> | <input checked="" type="checkbox"/> A description of any assumptions or corrections, such as tests of normality and adjustment for multiple comparisons |
| <input type="checkbox"/> | <input checked="" type="checkbox"/> A full description of the statistical parameters including central tendency (e.g. means) or other basic estimates (e.g. regression coefficient) AND variation (e.g. standard deviation) or associated estimates of uncertainty (e.g. confidence intervals) |
| <input type="checkbox"/> | <input checked="" type="checkbox"/> For null hypothesis testing, the test statistic (e.g. F , t , r) with confidence intervals, effect sizes, degrees of freedom and P value noted
<i>Give P values as exact values whenever suitable.</i> |
| <input checked="" type="checkbox"/> | <input type="checkbox"/> For Bayesian analysis, information on the choice of priors and Markov chain Monte Carlo settings |
| <input checked="" type="checkbox"/> | <input type="checkbox"/> For hierarchical and complex designs, identification of the appropriate level for tests and full reporting of outcomes |
| <input type="checkbox"/> | <input checked="" type="checkbox"/> Estimates of effect sizes (e.g. Cohen's d , Pearson's r), indicating how they were calculated |

Our web collection on [statistics for biologists](#) contains articles on many of the points above.

Software and code

Policy information about [availability of computer code](#)

Data collection	Images were acquired by Nikon Eclipse microscope and Zeiss 980 Confocal Imaging System. Bulk RNA-seq/ChIP-seq/Hi-ChIP/ATAC-seq were performed using an Illumina NextSeq500 or NovaSeq 6000 instrument. Immunoblots were imaged using ChemiDoc MP imaging system (BioRad). Histone mass spectrometry was analyzed with Q Exactive Plus Orbitrap (Thermo Fisher Scientific). Metabolomic profiling was analyzed using a 5500 QTRAP hybrid triple quadrupole mass spectrometer (AB/SCIEX) coupled to a Prominence UFLC HPLC system (Shimadzu) with HILIC chromatography (Waters Amide XBridge). Fluorescence and luminescence data were read by BioTek Synergy 2 Alpha Microplate Reader. qPLRX-RIME data were collected by Dionex Ultimate 3000 UHPLC system coupled with the LTQ.Orbitrap Velos mass spectromete. Flow cytometry data was collected using LSRFortessa High-Parameter Flow Cytometer.
Data analysis	Statistical analyses were performed using GraphPad Prism (v10.3.1) or R(v4.3.1). Immunofluorescence and immune blot data was analyzed using ImageJ(v1.53q). Synergy was assessed based on BLISS model using SynergyFinder (v2.0). ChIPseq peak calling was performed using CHIPs pipeline and analyzed by Seqplots (v.1.12.0), BEDtools (v. 2.30.0), deepTools (v.3.5.0). RNAseq experiments were analyzed using STAR (v2.5.1b), DESeq2 (v1.41.1), edgeR (v 3.14), Salmon (v0.14.1) and GSEA (v. 1.34.0). Hi-ChIP data were analyzed by HiC-Pro (v.3.1.0) pipeline. Differential interaction sites were analyzed by HiTC (v. 1.38.0) and HiCCompare (v. 1.16.0). Metabolomic data was analyzed using MetaboAnalyst (v4.0). Histone Mass Spec data were analyzed using Sky (v4.0) and Spectrum Mill (v7.0) software package. IP-mass spec data were analyzed using ProTIGY interactive, visualization tool (v0.7.5). Flow cytometry data were analyzed using BD FACSDiva (v9.0) and FlowJo (v10.10).

For manuscripts utilizing custom algorithms or software that are central to the research but not yet described in published literature, software must be made available to editors and reviewers. We strongly encourage code deposition in a community repository (e.g. GitHub). See the Nature Portfolio [guidelines for submitting code & software](#) for further information.

Data

Policy information about [availability of data](#)

All manuscripts must include a [data availability statement](#). This statement should provide the following information, where applicable:

- Accession codes, unique identifiers, or web links for publicly available datasets
- A description of any restrictions on data availability
- For clinical datasets or third party data, please ensure that the statement adheres to our [policy](#)

All data needed to evaluate the conclusions in the paper are present in the paper and/or the Supplemental Information. All raw and processed genomic data was deposited to GEO under accession number: GSE199913. All the genomic data were aligned to human reference genome GRCh37/hg19 (https://www.ncbi.nlm.nih.gov/datasets/genome/GCF_000001405.13/). RIME data are available via ProteomeXchange with identifier PXD031768. The original mass spectra, spectral library, and the protein sequence database used for searches have been deposited in the public proteomics repository MassIVE (identifier MSV000096930, <http://massive.ucsd.edu>) and are accessible at <ftp://massive.ucsd.edu/v09/MSV000096930/>. The mRNA expression data and the clinical data of TCGA and METABRIC were downloaded from TCGA data portal (<https://portal.gdc.cancer.gov>) and Synapse (Syn1688369) respectively. For TCGA, RNA-seq reads were reprocessed using Salmon v0.14.1103 and Log2 (TPM+1) values were used. For genes with multiple probes in METABRIC, probes with the highest inter-quartile range (IQR) were selected to represent the gene. Copy number information of KDM4C from TCGA and METABRIC were downloaded from cBioPortal predicted by GISTIC algorithm104. Fifty-seven breast cancer cell line copy number, lineage information and RNA-seq (FPKM) were downloaded from Cancer Cell Line Encyclopedia105. AUC towards different chemotherapy drugs were downloaded from DepMap (<https://depmap.org/portal/>)52. Microarray data from five neoadjuvant therapy TNBC cohort were downloaded from GSE32646, GSE32603, GSE20194, GSE25066 and GSE18864 respectively. Log2 normalized probe intensities was used for signature enrichment analysis. The mRNA and normalized metabolomic profile data from FUSCC cohort were downloaded from Gong et. al. and GSE118527. For the KDM4C peak overlap analysis, public available data for H3K27ac ChIP-seq were downloaded from GSE72956 (HCC1954), GSE57436 (MCF7), GSE65201 (T47D). H3K4me3 ChIP-seq were downloaded from GSE54693 (MCF7) and GSE80592 (T47D).

Field-specific reporting

Please select the one below that is the best fit for your research. If you are not sure, read the appropriate sections before making your selection.

Life sciences Behavioural & social sciences Ecological, evolutionary & environmental sciences

For a reference copy of the document with all sections, see [nature.com/documents/nr-reporting-summary-flat.pdf](https://www.nature.com/documents/nr-reporting-summary-flat.pdf)

Life sciences study design

All studies must disclose on these points even when the disclosure is negative.

Sample size	Sample size for each experiment is indicated in the legend. No statistical methods were used to predetermine sample sizes. The sample size was chosen empirically to provide a sufficient level of statistical power for detecting indicated biological effects based on previous published literatures (e.g. PMID 26409824, 31239270), with a minimal n=4, maximum n=12, mostly n=5-10 for in vivo experiments.
Data exclusions	Sequencing data that did not meet the QC was excluded
Replication	High throughput sequencing, large cell line panel examination, screen, mass spectrometry, animal experiments and clinical sample-related experiments were performed once due to time, cost and resource limitations, while sufficient number of biological replicates were included when applicable. Data present in Extended Data Fig. 2g, 3j-k, 5g, 5h, 5k, 6b, 6d, 6i, 7d, 7e, 7k-n, 8e, 9b, 9i, and Supplementary Figure 3 were performed once with technical replicates. All the other experiments were performed at least 2-3 times with successful replication showing similar observations. Key experiments have been repeated by multiple different personnel at different times. Number of replicates and sample size are indicated in the figure legends.
Randomization	Mice were randomized to treatment groups after they developed palpable tumors. For in vitro studies, randomization was not applied because the samples (e.g., cultured cells and other biological materials) exhibit high homogeneity, and they are relatively consistent across different replicates. This ensures that the experimental and control groups have similar baseline level without the need for randomization.
Blinding	Sequencing data processing was performed by bioinformaticians blinded to the identity of samples. For most in vitro assay blinding was not possible as samples had to be labeled. The investigators were not blinded to allocation during other experiments and outcome assessment.

Reporting for specific materials, systems and methods

We require information from authors about some types of materials, experimental systems and methods used in many studies. Here, indicate whether each material, system or method listed is relevant to your study. If you are not sure if a list item applies to your research, read the appropriate section before selecting a response.

Materials & experimental systems

n/a	Involved in the study
<input type="checkbox"/>	<input checked="" type="checkbox"/> Antibodies
<input type="checkbox"/>	<input checked="" type="checkbox"/> Eukaryotic cell lines
<input checked="" type="checkbox"/>	<input type="checkbox"/> Palaeontology and archaeology
<input type="checkbox"/>	<input checked="" type="checkbox"/> Animals and other organisms
<input checked="" type="checkbox"/>	<input type="checkbox"/> Human research participants
<input checked="" type="checkbox"/>	<input type="checkbox"/> Clinical data
<input checked="" type="checkbox"/>	<input type="checkbox"/> Dual use research of concern

Methods

n/a	Involved in the study
<input type="checkbox"/>	<input checked="" type="checkbox"/> ChIP-seq
<input type="checkbox"/>	<input checked="" type="checkbox"/> Flow cytometry
<input checked="" type="checkbox"/>	<input type="checkbox"/> MRI-based neuroimaging

Antibodies

Antibodies used

Rabbit polyclonal KDM4C antibody Novus Biologicals Cat# NBP1-49600, RRID:AB_10011699 (WB/ChIP-seq/IF/IP)
 Goat polyclonal Anti-cathepsin L antibody Novus Biologicals Cat# AF952, RRID:AB_355737 (ChIP-seq/Hi-ChIP/IF/IP)
 Mouse monoclonal Anti-cathepsin L antibody (Clone 33/2) Novus Cat# NB100-1775, RRID:AB_10124480 (WB)
 Mouse monoclonal Anti- α tubulin antibody (Clone B-5-1-2) Sigma-Aldrich Cat# T5168, RRID:AB_477579 (WB)
 Rabbit monoclonal Anti-vinculin antibody (Clone E1E9V) Cell Signaling Technology Cat# 13901, RRID:AB_2728768 (WB)
 Rabbit polyclonal Anti-GRHL2 antibody Sigma-Aldrich Cat# HPA004820, RRID:AB_1857928 (ChIP-seq/WB/IF/IP)
 Rabbit polyclonal Anti-GCLC antibody Abcam Cat# ab53179, RRID:AB_880163 (WB/IF)
 Rabbit polyclonal Anti-Histone H3 antibody (C-terminus) Abcam Cat# ab1791, RRID:AB_302613 (WB/ChIP-seq)
 Rabbit polyclonal Anti-Histone H3 antibody (N-terminus) Abcam Cat# ab18521, RRID:AB_732917 (WB)
 Rabbit polyclonal Anti-GFP antibody Novus Biologicals Cat# NB600-308, RRID:AB_10003058 (ChIP-seq/WB)
 Rabbit polyclonal Anti-V5 Tag antibody Novus Biologicals Cat# NB600-381, RRID:AB_10001084 (ChIP-seq/WB)
 Rabbit polyclonal Anti-Histone H3 (tri methyl K9) antibody Abcam Cat# ab8898, RRID:AB_306848 (ChIP-seq)
 Rabbit polyclonal Anti-Histone H3 (tri methyl K36) antibody Abcam Cat# ab9050, RRID:AB_306966 (ChIP-seq)
 Rabbit monoclonal Anti-Histone H3 (tri methyl K4) antibody Abcam Cat# ab8580, RRID:AB_306649 (ChIP-seq)
 Rabbit polyclonal Anti-Histone H3 (acetylation K27) antibody Diagenode C15410196, RRID:AB_2637079 (ChIP-seq)
 Rabbit polyclonal Anti-KDM4A antibody Bethyl Laboratories Cat# A300-861A, RRID:AB_609461 (ChIP-seq)
 Rabbit polyclonal Anti-KDM4B antibody Active Motif Cat# 61222, RRID:AB_2615033 (ChIP-seq)
 Rabbit monoclonal Anti-AIF antibody (Clone D39D2) Cell Signaling Technology Cat# 5318, AB_10634755 (WB)
 Mouse polyclonal Anti-Histone H3 antibody Active Motif Cat# 39763, RRID:AB_2650522 (WB)
 Rabbit monoclonal Anti-KDM4B antibody (Clone D7E6) Cell Signaling Technology Cat# 8639, RRID:AB_11140642(WB)
 Rabbit monoclonal Anti-KDM4A antibody (CloneC37E5) Cell Signaling Technology Cat# 5328, RRID:AB_10828595 (WB)
 Rabbit monoclonal Anti-HA-Tag antibody (Clone C29F4) Cell Signaling Technology Cat# 3724,RRID:AB_1549585 (WB)
 Rabbit polyclonal Anti-pan methyl Lysine antibody Abcam Cat# ab7315, RRID:AB_305840 (IP)
 Mouse monoclonal Anti-CTCF antibody (clone 48) BD Biosciences Cat# 612149, RRID:AB_399520 (WB)
 Rabbit IgG Isotype Control, Thermo Fisher Scientific, Cat# 31887, RRID:AB_2532177 (IP)
 Goat IgG Isotype Control, Novus, Cat# NB410-28088, RRID:AB_1853319 (IP)
 Goat anti-Rabbit IgG (H+L) Secondary Antibody Thermo Fischer Scientific Cat#65-6120,RRID:AB_2533967 (WB)
 Goat anti-Mouse IgG (H+L) Secondary Antibody Thermo Fischer Scientific Cat#62-6520,RRID:AB_2533947(WB)
 Rabbit anti-Goat IgG (H+L) Secondary Antibody Thermo Fischer Scientific Cat#81-1620,RRID:AB_2534006(WB)

Validation

Rabbit polyclonal KDM4C antibody Vacliated for reactivity towards human Application: Immunoblot: 1:1000; Immuofluorescence: 1:100; ChIP-seq:5 μ g; Immuno precipitation:5 μ g Product info: https://www.novusbio.com/products/lysine-k-specific-demethylase-4c-kdm4c-jmjd2c-antibody_nbp1-49600?srsId=AfmBOoqmd0j5ZL00l-t3ANOqrbp2-kSudBRwzYeSQGRi4YuHAoXmE4EK
 Goat polyclonal Anti-cathepsin L antibody Vacliated for reactivity towards human Application: Immunoblot: 1:1000; Immuofluorescence: 1:100; ChIP-seq:5 μ g; Immuno precipitation:5 μ g Product info:https://www.rndsystems.com/products/human-cathepsin-l-antibody_af952
 Mouse monoclonal Anti-cathepsin L antibody (Clone 33/2) Vacliated for reactivity towards human Application: Immunoblot: 1:1000 Product info:https://www.novusbio.com/products/cathepsin-l-antibody-33-2_nb100-1775?srsId=AfmBOopCCoWHK-W10SqvMXCxpFOaVV-HvUhkI2duacXyIJ5MM3nFmJNl
 Mouse monoclonal Anti- α tubulin antibody (Clone B-5-1-2) Vacliated for reactivity towards human Application: Immunoblot: 1:5000 Product info:<https://www.sigmaaldrich.com/US/en/product/sigma/t5168?srsId=AfmBOoqlVRpraazSYrRkTt0VHhogR02DdUMsSFI5HPhswHijEVZua1X>
 Rabbit monoclonal Anti-vinculin antibody (Clone E1E9V) Vacliated for reactivity towards human Application: Immunoblot: 1:1000 Product info:https://www.cellsignal.com/products/primary-antibodies/vinculin-e1e9v-xp-rabbit-mab/13901?srsId=AfmBOopHeR-cRxmZBHWKy1R4jd5ESDDClsh_9-3IG1nWGMQRQ1BQxi1fS
 Rabbit polyclonal Anti-GRHL2 antibody Vacliated for reactivity towards human Application: Immunoblot: 1:1000; Immuofluorescence: 1:100; ChIP-seq:5 μ g; Immuno precipitation:5 μ g Product info:<https://www.sigmaaldrich.com/US/en/product/sigma/hpa004820?srsId=AfmBOoo8PYd7bsydb7k1QADl4yGAmWX--T3t6ZdBrFkhtf2VG1r0sw8e>
 Rabbit polyclonal Anit-GCLC antibody Vacliated for reactivity towards human Application: Immunoblot: 1:1000; Immuofluorescence: 1:100 Product info:<https://www.abcam.com/en-us/products/primary-antibodies/gclc-antibody-ab53179>
 Rabbit polyclonal Anti-Histone H3 antibody (C-terminus) Vacliated for reactivity towards human Application: Immunoblot: 1:1000; ChIP-seq:5 μ g Product info:<https://www.abcam.com/en-us/products/primary-antibodies/histone-h3-antibody-nuclear-marker-and-chip-grade-ab1791>
 Rabbit polyclonal Anti-Histone H3 antibody (N-terminus) Vacliated for reactivity towards human Application: Immunoblot: 1:1000 Product info:<https://www.abcam.com/en-us/products/primary-antibodies/histone-h3-antibody-ab18521>
 Rabbit polyclonal Anti-GFP antibody Vacliated for reactivity towards human Application: Immunoblot: 1:1000; ChIP-seq:5 μ g Product info:https://www.novusbio.com/products/gfp-antibody_nb600-308?srsId=AfmBOoqGduykvQyNYH9P-KQtFiu6SzieSeVFbYvmHMNHOOX64AoUmuA

Rabbit polyclonal Anti-V5 Tag antibody Vacliated for reactivity towards human Application: Immunoblot: 1:1000; ChIP-seq:5 µg Product info:https://www.novusbio.com/products/v5-epitope-tag-antibody_nb600-381?srsltid=AfmBOoo2xPUimSUVvU_PgZyN5TJwHfslqD50vthOUsaPPNjXzOZKZw

Rabbit polyclonal Anti-Histone H3 (tri methyl K9) antibody Vacliated for reactivity towards human Application: ChIP-seq:5 µg Product info:https://www.abcam.com/en-us/products/primary-antibodies/histone-h3-tri-methyl-k9-antibody-chip-grade-ab8898?srsltid=AfmBOooFMQga1E8Juh6ZSuQ26HRnugH7c5XAlwnPa--v1nODRysTZcW

Rabbit polyclonal Anti-Histone H3 (tri methyl K36) antibody Vacliated for reactivity towards human Application: ChIP-seq:5 µg Product info:https://www.abcam.com/en-us/products/primary-antibodies/histone-h3-tri-methyl-k36-antibody-chip-grade-ab9050?srsltid=AfmBOopqshYCTnAj05BKZCj_zci-3VhTGwjOlalyCaSqwVlcVYfpTv2H

Rabbit polyclonal Anti-Histone H3 (tri methyl K4) antibody Vacliated for reactivity towards human Application: Immunoblot: 1:1000; ChIP-seq:5 µg Product info:https://www.abcam.com/en-us/products/primary-antibodies/histone-h3-tri-methyl-k4-antibody-chip-grade-ab8580?srsltid=AfmBOoplzhSLZ07orJvzoYoLnrZoLClTg8Ui5Asw_6elGbTt-FQJ26SV

Rabbit polyclonal Anti-Histone H3 (acetylation K27) antibody Vacliated for reactivity towards human Application: ChIP-seq:5 µg Product info:https://www.diagenode.com/en/p/h3k27ac-polyclonal-antibody-premium-50-mg-18-ml

Rabbit polyclonal Anti-KDM4A antibody Vacliated for reactivity towards human Application: ChIP-seq:5 µg Product info:https://www.fortislife.com/products/primary-antibodies/rabbit-anti-jmjd2a-antibody/BETHYL-A300-861

Rabbit polyclonal Anti-KDM4B antibody Vacliated for reactivity towards human Application: ChIP-seq:5 µg Product info:https://www.activemotif.com/catalog/details/61221/jmjd2b-kdm4b-antibody-pab

Rabbit monoclonal Anti-AIF antibody (Clone D39D2) Vacliated for reactivity towards human Application: Immunoblot: 1:1000 Product info:https://www.cellsignal.com/products/primary-antibodies/aif-d39d2-xp-rabbit-mab/5318?srsltid=AfmBOoquAXQCFZ0DsNN2sab46XFhYfHNxvqS2gS6zVga1QnvQotbeyZO

Mouse polyclonal Anti-Histone H3 antibody Vacliated for reactivity towards human Application: Immunoblot: 1:1000 Product info:https://www.activemotif.com/catalog/details/39763

Rabbit monoclonal Anti-HA-Tag antibody (Clone C29F4) Vacliated for reactivity towards human Application: Immunoblot: 1:1000 Product info:https://www.cellsignal.com/products/primary-antibodies/ha-tag-c29f4-rabbit-mab/3724?srsltid=AfmBOoouv8Hv9PPIhbO4aMuHs_rJzgnwOV5b65L1Xx3gDrf4as5TFKBv

Rabbit monoclonal Anti-KDM4B antibody (Clone D7E6) Vacliated for reactivity towards human Application: Immunoblot: 1:1000 Product info:https://www.cellsignal.com/products/primary-antibodies/jmjd2b-d7e6-rabbit-mab/8639?srsltid=AfmBOoRlcAbi4QUEOLckZnxb-zFoVWi5n2v8eqwdlGzTDPTpW3mQUtDA

Rabbit monoclonal Anti-KDM4A antibody (CloneC37E5) Vacliated for reactivity towards human Application: Immunoblot: 1:500 Product info:https://www.cellsignal.com/products/primary-antibodies/jmjd2a-c37e5-rabbit-mab/5328?srsltid=AfmBOooD9i9hovycABC6f-HNEzmrWapVYfce96dMJQUq5VMTsE67dxS

Rabbit polyclonal Anti-pan methyl Lysine antibody Vacliated for reactivity towards human Application: Immuno precipitation:5 µg Product info:https://www.abcam.com/en-us/products/primary-antibodies/pan-methyl-lysine-antibody-chip-grade-ab7315?srsltid=AfmBOopam9TnArn1iVtvMS3B_j1_GWty_QDw3rN_-oe92d2jXksS1sM

Mouse monoclonal Anyi-CTCF antibody (Clone 48) Vacliated for reactivity towards human Application: Immunoblot: 1:1000 Product info:https://www.bdbiosciences.com/en-us/products/reagents/microscopy-imaging-reagents/immunofluorescence-reagents/purified-mouse-anti-ctcf.612149?tab=product_details

Eukaryotic cell lines

Policy information about [cell lines](#)

Cell line source(s)

BT549 cell line ATCC HTB-122
 CAL120 cell line ATCC ACC 459
 CAL51 cell line DSMZ ACC 302
 CAL851 cell line DSMZ ACC 440
 DU4475 cell line ATCC HTB-123
 HCC1143 cell line ATCC CRL-2321
 HCC1187 cell line ATCC CRL-2322
 HCC1395 cell line ATCC CRL-2324
 HCC1569 cell line ATCC CRL-2330
 HCC1806 cell line ATCC CRL-2335
 HCC1937 cell line ATCC CRL-2336
 HCC1954 cell line ATCC CRL-2338
 HCC2157 cell line ATCC CRL-2340
 HCC38 cell line ATCC CRL-2314
 HCC70 cell line ATCC CRL-2315
 HDQ-P1 cell line DSMZ ACC 494
 HS578T cell line ATCC HTB-126
 MCF7 cell line ATCC HTB-22
 MDA-MB-231 cell line ATCC HTB-26
 MDA-MB-436 cell line ATCC HTB-130
 MDA-MB-468 cell line ATCC HTB-132
 SUM1315 cell line Stephen Ethier, University of Michigan
 SUM149 cell line Stephen Ethier, University of Michigan
 SUM159 cell line Stephen Ethier, University of Michigan
 SUM3153 cell line Stephen Ethier, University of Michigan
 T47D cell line ATCC HTB-133
 293FT cell line Thermo Fisher Scientific R70007

Authentication

The identity of the cell lines was confirmed based on STR and exome-seq analyses.

Mycoplasma contamination

Cell lines were routinely tested for mycoplasma and rodent pathogen contamination. No contamination was found at any

Mycoplasma contamination	time point.
Commonly misidentified lines (See ICLAC register)	No commonly misidentified lines were used in this study.

Animals and other organisms

Policy information about [studies involving animals](#); [ARRIVE guidelines](#) recommended for reporting animal research

Laboratory animals	For xenograft assays using KDM4C knockdown HCC1954 and SUM149 models, and cisplatin/QC6352/BSO drug combination assay, female NCr nude (CrTac:NCr-Foxn1nu) mice were purchased from Taconic Biosciences at 5-6 weeks of age. For experiments using HCl-041 PDX, KDM4C knockdown HCC1806, and CTSL knockout SUM149 and HCC1806 models, female NSG (NOD.Cg-Prkdcscid Il2rgtm1Wjl/SzJ) mice were purchased from The Jackson Laboratory at 5-6 weeks of age. Mice were housed 5 to a cage with ad libitum access to food and water in 20°C ambient temperature, 40-50% humidity, and 12-hour light/12-hour dark cycle.
Wild animals	No wild animals were used in this study.
Field-collected samples	No field-collected samples were used in this study.
Ethics oversight	Animal studies were performed according to protocol 11-023 approved by the Dana-Farber Cancer Institute Animal Care and Use Committee.

Note that full information on the approval of the study protocol must also be provided in the manuscript.

ChIP-seq

Data deposition

- Confirm that both raw and final processed data have been deposited in a public database such as [GEO](#).
- Confirm that you have deposited or provided access to graph files (e.g. BED files) for the called peaks.

Data access links <i>May remain private before publication.</i>	The ChIP-seq data has been deposited as a SubSeries in GEO under the SuperSeries ID code (GSE199913).
--	---

Files in database submission	<p>Sample Name processed data file (Bigwig) raw fastq files (first 87 samples are single-end, last 10 samples are paired-end)</p> <p>HCC1954_shKDM4C_17_Control_Input NA 20140623-HCC1954input-GP1109_S3_R1.fastq.gz</p> <p>HCC1954_shKDM4C-17_Control_K9me3_1 HCC1954_shKDM4C-17_Control_K9me3_2.rep1_treat_pileup.bw 20151226-HCC1954-CONTROL-K9me3-GP2601_S5_R1_001.fastq.gz</p> <p>HCC1954_shKDM4C-17_Control_K9me3_2 HCC1954_shKDM4C-17_Control_KDM4C_1.rep1_treat_pileup.bw 20161016_1954C_K9_C3_GP3575_S5_R1_001.fastq.gz</p> <p>HCC1954_shKDM4C-17_Doxy_K9me3_1 HCC1954_shKDM4C-17_Doxy_K9me3_1.rep1_treat_pileup.bw 20151226-HCC1954-DOXY-K9me3-GP2601_S6_R1_001.fastq.gz</p> <p>HCC1954_shKDM4C-17_Doxy_K9me3_2 HCC1954_shKDM4C-17_Doxy_K9me3_2.rep1_treat_pileup.bw 20161016_1954D_K9_C4_GP3575_S6_R1_001.fastq.gz</p> <p>HCC1954_shKDM4C-17_ML324_K9me3_1 HCC1954_shKDM4C-17_ML326_K9me3_1.rep1_treat_pileup.bw 20151226-HCC1954-ML-K9me3-GP2601_S7_R1_001.fastq.gz</p> <p>HCC1954_shKDM4C-17_ML324_K9me3_2 HCC1954_shKDM4C-17_ML327_K9me3_2.rep1_treat_pileup.bw 20161016_1954M_K9_C5_GP3575_S7_R1_001.fastq.gz</p> <p>HCC1954_shKDM4C-17_Control_K36me3_1 HCC1954_shKDM4C-17_Control_K36me3_1.rep1_treat_pileup.bw 20151222-HCC1954-Control-K36me3-GP2600_S3_R1_001.fastq.gz</p> <p>HCC1954_shKDM4C-17_Control_K36me3_2 HCC1954_shKDM4C-17_Control_K36me3_2.rep1_treat_pileup.bw 20161129_1954_C_K36_GP3718_S1_R1_001.fastq.gz</p> <p>HCC1954_shKDM4C-17_Doxy_K36me3_1 HCC1954_shKDM4C-17_Doxy_K36me3_1.rep1_treat_pileup.bw 20151222-HCC1954-Doxy-K36me3-GP2600_S4_R1_001.fastq.gz</p> <p>HCC1954_shKDM4C-17_Doxy_K36me3_2 HCC1954_shKDM4C-17_Doxy_K36me3_2.rep1_treat_pileup.bw 20161129_1954_D_K36_GP3718_S2_R1_001.fastq.gz</p> <p>HCC1954_shKDM4C-17_ML324_K36me3_1 HCC1954_shKDM4C-17_ML328_K36me3_1.rep1_treat_pileup.bw 20151222-HCC1954-ML324-K36me3-GP2600_S5_R1_001.fastq.gz</p> <p>HCC1954_shKDM4C-17_ML324_K36me3_2 HCC1954_shKDM4C-17_ML329_K36me3_2.rep1_treat_pileup.bw 20161129_1954_M_K36_GP3718_S3_R1_001.fastq.gz</p> <p>HCC1954_shKDM4C-17_Control_KDM4C_1 HCC1954_shKDM4C-17_Control_KDM4C_1.rep1_treat_pileup.bw 20151218-HCC1954-Control-JMJ-GP2598_S1_R1_001.fastq.gz</p> <p>HCC1954_shKDM4C-17_Control_KDM4C_2 HCC1954_shKDM4C-17_Control_KDM4C_2.rep1_treat_pileup.bw 20161016_1954C_JMJ_A11_GP3573_S9_R1_001.fastq.gz</p> <p>HCC1954_shKDM4C-17_Control_H3K4me3 HCC1954_shKDM4C-17_Control_H3K4me3.rep1_treat_pileup.bw 20161016_1954C_K4_B1_GP3573_S3_R1_001.fastq.gz</p> <p>HCC1954_shKDM4C-17_Doxy_H3K4me3 HCC1954_shKDM4C-17_Doxy_H3K4me3.rep1_treat_pileup.bw 20161016_1954D_K4_B2_GP3573_S4_R1_001.fastq.gz</p> <p>HCC1954_shKDM4C-17_ML324_H3K4me3 HCC1954_shKDM4C-17_ML330_H3K4me3.rep1_treat_pileup.bw 20161016_1954M_K4_B3_GP3573_S5_R1_001.fastq.gz</p> <p>SUM149_shKDM4C_17_Control_Input_3 NA 180406_S149_17C_INPUT_GP5435_S7_R1_001.fastq.gz</p> <p>SUM149_shKDM4C_17_Control_K9me3_1 SUM149_shKDM4C-17_Control_K9me3_1.rep1_treat_pileup.bw 20150727-N149-K9-GP2134_S1_R1_001.fastq.gz</p> <p>SUM149_shKDM4C_17_Control_K9me3_2 SUM149_shKDM4C-17_Control_K9me3_2.rep1_treat_pileup.bw</p>
------------------------------	---

20150917-149-17-K9me3-utube-GP2281_S11_R1_001.fastq.gz
SUM149_shKDM4C_17_Control_K9me3_3 SUM149_shKDM4C-17_Control_K9me3_3.rep1_treat_pileup.bw 20150917-149-
K9me3-Abcam150uM-GP2281_S6_R1_001.fastq.gz
SUM149_shKDM4C_17_Control_K9me3_4 SUM149_shKDM4C-17_Control_K9me3_4.rep1_treat_pileup.bw 20151226-
SUM149-Control-K9me3-GP2601_S8_R1_001.fastq.gz
SUM149_shKDM4C_17_Control_K9me3_5 SUM149_shKDM4C-17_Control_K9me3_5.rep1_treat_pileup.bw
20161016_149C_K9_C6_GP3575_S8_R1_001.fastq.gz
SUM149_shKDM4C_17_Doxy_K9me3_1 SUM149_shKDM4C-17_Doxy_K9me3_1.rep1_treat_pileup.bw 20150727-D149-K9-
GP2134_S2_R1_001.fastq.gz
SUM149_shKDM4C_17_Doxy_K9me3_2 SUM149_shKDM4C-17_Doxy_K9me3_2.rep1_treat_pileup.bw 20151226-SUM149-
Doxy-K9me3-GP2601_S9_R1_001.fastq.gz
SUM149_shKDM4C_17_Doxy_K9me3_3 SUM149_shKDM4C-17_Doxy_K9me3_3.rep1_treat_pileup.bw
20161016_149D_K9_C7_GP3575_S9_R1_001.fastq.gz
SUM149_shKDM4C_17_ML324_K9me3_1 SUM149_shKDM4C-17_ML324_K9me3_1.rep1_treat_pileup.bw 20150727-M149-
K9-GP2134_S3_R1_001.fastq.gz
SUM149_shKDM4C_17_ML324_K9me3_2 SUM149_shKDM4C-17_ML324_K9me3_2.rep1_treat_pileup.bw 20151226-
SUM149-ML324-K9me3-GP2601_S10_R1_001.fastq.gz
SUM149_shKDM4C_17_ML324_K9me3_3 SUM149_shKDM4C-17_ML324_K9me3_3.rep1_treat_pileup.bw
20161016_149M_K9_C8_GP3575_S10_R1_001.fastq.gz
SUM149_shKDM4C-17_Control_K36me3_1 SUM149_shKDM4C-17_Control_K36me3_1.rep1_treat_pileup.bw 20150727-
N149-K36-GP2134_S6_R1_001.fastq.gz
SUM149_shKDM4C-17_Control_K36me3_2 SUM149_shKDM4C-17_Control_K36me3_2.rep1_treat_pileup.bw
20150917-149-17-K36me3-utube-GP2281_S12_R1_001.fastq.gz
SUM149_shKDM4C-17_Control_K36me3_3 SUM149_shKDM4C-17_Control_K36me3_3.rep1_treat_pileup.bw 20151222-
SUM149-Control-K36me3-GP2600_S6_R1_001.fastq.gz
SUM149_shKDM4C-17_Control_K36me3_4 SUM149_shKDM4C-17_Control_K36me3_4.rep1_treat_pileup.bw
20161129_149_C_K36_GP3718_S4_R1_001.fastq.gz
SUM149_shKDM4C-17_Control_K36me3_5 SUM149_shKDM4C-17_Control_K36me3_5.rep1_treat_pileup.bw 20141126-
SUM149-No-K36me3-GP1520_S4_R1_001.fastq.gz
SUM149_shKDM4C_17_Doxy_K36me3_1 SUM149_shKDM4C-17_Doxy_K36me3_1.rep1_treat_pileup.bw 20150727-D149-
K36-GP2134_S7_R1_001.fastq.gz
SUM149_shKDM4C_17_Doxy_K36me3_2 SUM149_shKDM4C-17_Doxy_K36me3_2.rep1_treat_pileup.bw 20151222-
SUM149-Doxy-K36me3-GP2600_S7_R1_001.fastq.gz
SUM149_shKDM4C_17_Doxy_K36me3_3 SUM149_shKDM4C-17_Doxy_K36me3_3.rep1_treat_pileup.bw 20141126-
SUM149-Doxy-K36me3-GP1520_S5_R1_001.fastq.gz
SUM149_shKDM4C_17_ML324_K36me3_1 SUM149_shKDM4C-17_ML324_K36me3_1.rep1_treat_pileup.bw 20150727-
M149-K36-GP2134_S8_R1_001.fastq.gz
SUM149_shKDM4C_17_ML324_K36me3_2 SUM149_shKDM4C-17_ML324_K36me3_2.rep1_treat_pileup.bw 20151222-
SUM149-ML324-K36me3-GP2600_S8_R1_001.fastq.gz
SUM149_shKDM4C_17_ML324_K36me3_3 SUM149_shKDM4C-17_ML324_K36me3_3.rep1_treat_pileup.bw
20161129_149_M_K36_GP3718_S5_R1_001.fastq.gz
SUM149_shKDM4C_17_ML324_K36me3_4 SUM149_shKDM4C-17_ML324_K36me3_4.rep1_treat_pileup.bw 20141126-
SUM149-ML-K36me3-GP1520_S6_R1_001.fastq.gz
SUM149_shKDM4C-17_Control_H3K4me3 SUM149_shKDM4C-17_Control_H3K4me3.rep1_treat_pileup.bw
20161016_149C_K4_B4_GP3573_S6_R1_001.fastq.gz
SUM149_shKDM4C-17_Doxy_H3K4me3 SUM149_shKDM4C-17_Doxy_H3K4me3.rep1_treat_pileup.bw
20161016_149D_K4_B5_GP3573_S7_R1_001.fastq.gz
SUM149_shKDM4C-17_ML324_H3K4me3 SUM149_shKDM4C-17_ML324_H3K4me3.rep1_treat_pileup.bw
20161016_149M_K4_B6_GP3573_S8_R1_001.fastq.gz
SUM149_shKDM4C-17_Control_KDM4C_1 SUM149_shKDM4C-17_Control_KDM4C_1.rep1_treat_pileup.bw 20150728-
N149J-GP2135_S1_R1_001.fastq.gz
SUM149_shKDM4C-17_Control_KDM4C_2 SUM149_shKDM4C-17_Control_KDM4C_2.rep1_treat_pileup.bw
20150917-149-17-JMJD2C-utube-GP2281_S10_R1_001.fastq.gz
SUM149_shKDM4C-17_Control_KDM4C_3 SUM149_shKDM4C-17_Control_KDM4C_3.rep1_treat_pileup.bw 20151218-
SUM149-Control-JMJ-GP2598_S4_R1_001.fastq.gz
SUM149_shKDM4C-17_Control_KDM4C_4 SUM149_shKDM4C-17_Control_KDM4C_4.rep1_treat_pileup.bw
20161016_149C_JMJ_B1_GP3575_S1_R1_001.fastq.gz
SUM149_Parental_Control_K27me3 SUM149_Parental_Control_K27me3.rep1_treat_pileup.bw
20180516_S149_C_K27m3_GP5611_S13_R1_001.fastq.gz
HCC70_Parental_Untreated_INPUT NA 20150728-H70I-GP2135_S6_R1_001.fastq.gz
HCC70_Parental_Untreated_KDM4C HCC70_Parental_Untreated_KDM4C.rep1_treat_pileup.bw 20150728-H70I-
GP2135_S4_R1_001.fastq.gz
MCF7_Parental_Untreated_KDM4C MCF7_Parental_Untreated_KDM4C.rep1_treat_pileup.bw 20150728-M7J-
GP2135_S5_R1_001.fastq.gz
MCF7_Parental_Untreated_K9me3 MCF7_Parental_Untreated_K9me3.rep1_treat_pileup.bw 20150727-M7-K9-
GP2134_S5_R1_001.fastq.gz
MCF7_Parental_Untreated_K36me3 MCF7_Parental_Untreated_K36me3.rep1_treat_pileup.bw 20150727-M7-K36-
GP2134_S10_R1_001.fastq.gz
HCC2157_Parental_Untreated_KDM4C HCC2157_Parental_Untreated_KDM4C.rep1_treat_pileup.bw
20161216_HCC2157_JMJ_GP3794_S9_R1_001.fastq.gz
T47D_shKDM4C_17_Control_INPUT NA 20150506-T47D-DMSO-INPUT-GP1906_S7_R1_001.fastq.gz
T47D_shKDM4C-17_Control_KDM4C T47D_shKDM4C-17_Control_KDM4C.rep1_treat_pileup.bw
20161016_T47DC_JMJ_B3_GP3575_S3_R1_001.fastq.gz
T47D_shKDM4C_17_Control_K9me3_1 T47D_shKDM4C-17_Control_K9me3_1.rep1_treat_pileup.bw
20170311_T47D_C_K9_GP4112_S6_R1_001.fastq.gz
T47D_shKDM4C_17_Control_K36me3_1 T47D_shKDM4C-17_Control_k36me3_1.rep1_treat_pileup.bw

20161129_T47D_C_K36_GP3718_S6_R1_001.fastq.gz
SUM149_Parental_Control_INPUT NA 20180516_S149_C_INPUT_GP5612_S1_R1_001.fastq.gz
SUM149_Parental_ML324_INPUT NA 20180516_S149_M_INPUT_GP5612_S2_R1_001.fastq.gz
SUM149_Parental_Control_CTSL SUM149_Parental_Control_CTSL.rep1_treat_pileup.bw
20161215_149_C_CTL_GP3793_S7_R1_001.fastq.gz
SUM149_Parental_ML324_CTSL SUM149_Parental_ML324_CTSL.rep1_treat_pileup.bw
20161215_149_M_CTL_GP3793_S8_R1_001.fastq.gz
SUM149_Resistant_Control_CTSL SUM149_ML324-R_Control_CTSL.rep1_treat_pileup.bw
20161215_149_RC_CTL_GP3793_S9_R1_001.fastq.gz
SUM149_Resistant_ML324_CTSL SUM149_ML324-R_ML324_CTSL.rep1_treat_pileup.bw
20161215_149_RM_CTL_GP3793_S10_R1_001.fastq.gz
SUM149_Parental_Control_GRHL2 SUM149_Parental_Control_GRHL2.rep1_treat_pileup.bw
20180507_S149_C_GRHL2_GP5566_S5_R1_001.fastq.gz
SUM149_Parental_ML324_GRHL2 SUM149_Parental_ML324_GRHL2.rep1_treat_pileup.bw
20180507_S149_M_GRHL2_GP5566_S6_R1_001.fastq.gz
HCC1954_Parental_Control_INPUT NA 20180430_1954_C_INPUT_GP5539_S7_R1_001.fastq.gz
HCC1954_Parental_Control_CTSL HCC1954_Parental_Control_CTSL.rep1_treat_pileup.bw
20180430_1954_C_CTSL_GP5539_S1_R1_001.fastq.gz
HCC1954_Parental_Control_GRHL2 HCC1954_Parental_Control_GRHL2.rep1_treat_pileup.bw
20180430_1954_C_GRHL2_GP5539_S3_R1_001.fastq.gz
SUM149_C_KDM4A SUM149_C_KDM4A.rep1_treat_pileup.bw 20190310_SUM149_C_KDM4A_GP6745_S1_R1_001.fastq.gz
SUM149_C_KDM4B SUM149_C_KDM4B.rep1_treat_pileup.bw 20190310_SUM149_C_KDM4B_GP6745_S5_R1_001.fastq.gz
SUM149_C_KDM4C SUM149_C_KDM4C.rep1_treat_pileup.bw 20190310_SUM149_C_KDM4C_GP6745_S9_R1_001.fastq.gz
SUM149_M_KDM4A SUM149_M_KDM4A.rep1_treat_pileup.bw
20190310_SUM149_M_KDM4A_GP6745_S2_R1_001.fastq.gz
SUM149_M_KDM4B SUM149_M_KDM4B.rep1_treat_pileup.bw
20190310_SUM149_M_KDM4B_GP6745_S6_R1_001.fastq.gz
SUM149_M_KDM4C SUM149_M_KDM4C.rep1_treat_pileup.bw
20190310_SUM149_M_KDM4C_GP6745_S10_R1_001.fastq.gz
SUM149_sgGRHL2_C_CTSL SUM149_GRHL2_C_CTSL.rep1_treat_pileup.bw
20190310_SUM149_GRHL2_C_CTSL_GP6744_S11_R1_001.fastq.gz
SUM149_sgScramble_C_CTSL SUM149_ScrB_C_CTSL.rep1_treat_pileup.bw
20190310_SUM149_ScrB_C_CTSL_GP6744_S9_R1_001.fastq.gz
SUM149_V5_H3_C_Ct SUM149_V5_H3_C_Ct.rep1_treat_pileup.bw
20190310_SUM149_V5_H3_C_Ct_GP6744_S1_R1_001.fastq.gz
SUM149_V5_H3_C_V5 SUM149_V5_H3_C_V5.rep1_treat_pileup.bw
20190310_SUM149_V5_H3_C_V5_GP6744_S5_R1_001.fastq.gz
SUM149_V5_H3_M_Ct SUM149_V5_H3_M_Ct.rep1_treat_pileup.bw
20190310_SUM149_V5_H3_M_Ct_GP6744_S2_R1_001.fastq.gz
SUM149_V5_H3_M_V5 SUM149_V5_H3_M_V5.rep1_treat_pileup.bw
20190310_SUM149_V5_H3_M_V5_GP6744_S6_R1_001.fastq.gz
SUM149_GFP_H3_C_Ct SUM149_GFP_H3_C_Ct.rep1_treat_pileup.bw
20190310_SUM149_GFP_H3_C_Ct_GP6743_S1_R1_001.fastq.gz
SUM149_GFP_H3_C_GFP SUM149_GFP_H3_C_GFP.rep1_treat_pileup.bw
20190310_SUM149_GFP_H3_C_GFP_GP6743_S3_R1_001.fastq.gz
SUM149_GFP_H3_M_Ct SUM149_GFP_H3_M_Ct.rep1_treat_pileup.bw
20190310_SUM149_GFP_H3_M_Ct_GP6743_S2_R1_001.fastq.gz
SUM149_GFP_H3_M_GFP SUM149_GFP_H3_M_GFP.rep1_treat_pileup.bw
20190310_SUM149_GFP_H3_M_GFP_GP6743_S4_R1_001.fastq.gz
HCC1806_sh5_Vehicle_Input NA 20240725_HCC1806_Veh_Input_ZL12286_S168_L008_R1_001.fastq.gz
20240725_HCC1806_Veh_Input_ZL12286_S168_L008_R2_001.fastq.gz
HCC1806_sh5_Vehicle_H3K9me3_rep1 HCC1806_H3K9me3_Veh_rep1.bw
20240725_HCC1806_Veh_K9_1_ZL12286_S152_L008_R1_001.fastq.gz
20240725_HCC1806_Veh_K9_1_ZL12286_S152_L008_R2_001.fastq.gz
HCC1806_sh5_Vehicle_H3K9me3_rep2 HCC1806_H3K9me3_Veh_rep2.bw
20240725_HCC1806_Veh_K9_2_ZL12286_S153_L008_R1_001.fastq.gz
20240725_HCC1806_Veh_K9_2_ZL12286_S153_L008_R2_001.fastq.gz
HCC1806_sh5_Vehicle_H3K36me3_rep1 HCC1806_H3K36m3_Veh_rep1.bw
20240725_HCC1806_Veh_K36_1_ZL12286_S160_L008_R1_001.fastq.gz
20240725_HCC1806_Veh_K36_1_ZL12286_S160_L008_R2_001.fastq.gz
HCC1806_sh5_Vehicle_H3K36me3_rep2 HCC1806_H3K36me3_Veh_rep2.bw
20240725_HCC1806_Veh_K36_2_ZL12286_S161_L008_R1_001.fastq.gz
20240725_HCC1806_Veh_K36_2_ZL12286_S161_L008_R2_001.fastq.gz
HCC1806_sh5_shKDM4C_Input NA 20240725_HCC1806_Dox_Input_ZL12286_S169_L008_R1_001.fastq.gz
20240725_HCC1806_Dox_Input_ZL12286_S169_L008_R2_001.fastq.gz
HCC1806_sh5_shKDM4C_H3K9me3_rep1 HCC1806_H3K9me3_shKDM4C_rep1.bw
20240725_HCC1806_Dox_K9_1_ZL12286_S154_L008_R1_001.fastq.gz
20240725_HCC1806_Dox_K9_1_ZL12286_S154_L008_R2_001.fastq.gz
HCC1806_sh5_shKDM4C_H3K9me3_rep2 HCC1806_H3K9me3_shKDM4C_rep2.bw
20240725_HCC1806_Dox_K9_2_ZL12286_S155_L008_R1_001.fastq.gz
20240725_HCC1806_Dox_K9_2_ZL12286_S155_L008_R2_001.fastq.gz
HCC1806_sh5_shKDM4C_H3K36me3_rep1 HCC1806_H3K36m3_shKDM4C_rep1.bw
20240725_HCC1806_Dox_K36_1_ZL12286_S162_L008_R1_001.fastq.gz
20240725_HCC1806_Dox_K36_1_ZL12286_S162_L008_R2_001.fastq.gz
HCC1806_sh5_shKDM4C_H3K36me3_rep2 HCC1806_H3K36me3_shKDM4C_rep2.bw

20240725_HCC1806_Dox_K36_2_ZL12286_S163_L008_R1_001.fastq.gz
 20240725_HCC1806_Dox_K36_2_ZL12286_S163_L008_R2_001.fastq.gz

Genome browser session
 (e.g. [UCSC](#))

N/A

Methodology

Replicates

Samples were sequenced without replicates

Sequencing depth

Total reads and mapped reads for each sample are list below:
 Sample Total reads Mapped reads
 HCC1954_shKDM4C-17_Control_Input 41337134 40508691
 HCC1954_shKDM4C-17_Control_K9me3_1 35650438 35254271
 HCC1954_shKDM4C-17_Control_K9me3_2 69686476 68650919
 HCC1954_shKDM4C-17_Doxy_K9me3_1 52364752 51651492
 HCC1954_shKDM4C-17_Doxy_K9me3_2 72186523 71155032
 HCC1954_shKDM4C-17_ML324_K9me3_1 59889055 59332877
 HCC1954_shKDM4C-17_ML324_K9me3_2 75425157 74324524
 HCC1954_shKDM4C-17_Control_K36me3_1 64032303 63508870
 HCC1954_shKDM4C-17_Control_K36me3_2 63477308 62935996
 HCC1954_shKDM4C-17_Doxy_K36me3_1 63942137 63470769
 HCC1954_shKDM4C-17_Doxy_K36me3_2 66498082 65932361
 HCC1954_shKDM4C-17_ML324_K36me3_1 67186223 66616821
 HCC1954_shKDM4C-17_ML324_K36me3_2 61683058 61113788
 HCC1954_shKDM4C-17_Control_KDM4C_1 64503732 63744575
 HCC1954_shKDM4C-17_Control_KDM4C_2 47495897 46542830
 HCC1954_shKDM4C-17_Control_H3K4me3 49332574 48392176
 HCC1954_shKDM4C-17_Doxy_H3K4me3 54622248 53607668
 HCC1954_shKDM4C-17_ML324_H3K4me3 55656966 54596743
 SUM149_shKDM4C-17_Control_Input_3 49322784 48900869
 SUM149_shKDM4C-17_Control_K9me3_1 52768119 51723420
 SUM149_shKDM4C-17_Control_K9me3_2 34518124 33530615
 SUM149_shKDM4C-17_Control_K9me3_3 45920035 44266460
 SUM149_shKDM4C-17_Control_K9me3_4 77964643 76869055
 SUM149_shKDM4C-17_Control_K9me3_5 33748977 33145200
 SUM149_shKDM4C-17_Doxy_K9me3_1 53887540 52982582
 SUM149_shKDM4C-17_Doxy_K9me3_2 5817497 5744053
 SUM149_shKDM4C-17_Doxy_K9me3_3 57675016 56702389
 SUM149_shKDM4C-17_ML324_K9me3_1 43647241 42626233
 SUM149_shKDM4C-17_ML324_K9me3_2 58205744 57621055
 SUM149_shKDM4C-17_ML324_K9me3_3 48038238 47401625
 SUM149_shKDM4C-17_Control_K36me3_1 46560838 46174173
 SUM149_shKDM4C-17_Control_K36me3_2 32526373 31953022
 SUM149_shKDM4C-17_Control_K36me3_3 63458026 63046561
 SUM149_shKDM4C-17_Control_K36me3_4 62590933 61985700
 SUM149_shKDM4C-17_Control_K36me3_5 38767418 37693203
 SUM149_shKDM4C-17_Doxy_K36me3_1 59718811 59296737
 SUM149_shKDM4C-17_Doxy_K36me3_2 52225986 51867463
 SUM149_shKDM4C-17_Doxy_K36me3_3 57093783 55559936
 SUM149_shKDM4C-17_ML324_K36me3_1 44656702 44268443
 SUM149_shKDM4C-17_ML324_K36me3_2 49668179 49313573
 SUM149_shKDM4C-17_ML324_K36me3_3 66780988 66230959
 SUM149_shKDM4C-17_ML324_K36me3_4 61884460 59909565
 SUM149_shKDM4C-17_Control_H3K4me3 55539815 54380325
 SUM149_shKDM4C-17_Doxy_H3K4me3 52797037 51742385
 SUM149_shKDM4C-17_ML324_H3K4me3 42542595 41706550
 SUM149_shKDM4C-17_Control_KDM4C_1 51952956 51242251
 SUM149_shKDM4C-17_Control_KDM4C_2 39709747 38646767
 SUM149_shKDM4C-17_Control_KDM4C_3 53758843 52748982
 SUM149_shKDM4C-17_Control_KDM4C_4 57085372 55975068
 SUM149_Parental_Control_K27me3 33706284 33076818
 HCC70_Parental_Untreated_INPUT 71399350 70798465
 HCC70_Parental_Untreated_KDM4C 49448188 48781400
 MCF7_Parental_Untreated_KDM4C 51791943 51152407
 MCF7_Parental_Untreated_K9me3 55206835 54159768
 MCF7_Parental_Untreated_K36me3 56327253 55796610
 HCC2157_Parental_Untreated_KDM4C 54765134 53482859
 T47D_shKDM4C-17_Control_INPUT 66982316 66471712
 T47D_shKDM4C-17_Control_KDM4C 56749252 55527416
 T47D_shKDM4C-17_Control_K9me3_1 45236822 44208791
 T47D_shKDM4C-17_Control_K36me3_1 54557802 54130497
 SUM149_Parental_Control_INPUT 39210940 38718439
 SUM149_Parental_ML324_INPUT 34839122 34358586
 SUM149_Parental_Control_CTSL 59313832 58638940
 SUM149_Parental_ML324_CTSL 65554888 64930215

SUM149_ML324-R_Control_CTSL 57213657 56649638
 SUM149_ML324-R_ML324_CTSL 61397786 60799339
 SUM149_Parental_Control_GrHL2 42969183 42448097
 SUM149_Parental_ML324_GrHL2 34808283 34394105
 SUM149_Parental_Control_INPUT 39210940 38718439
 HCC1954_Parental_Control_CTSL 35486472 35129813
 HCC1954_Parental_Control_GrHL2 37744481 37362500
 SUM149_C_KDM4A 29381502 29162002
 SUM149_C_KDM4B 31531231 31238012
 SUM149_C_KDM4C 27988857 27759865
 SUM149_M_KDM4A 27378552 27148471
 SUM149_M_KDM4B 35639193 35319510
 SUM149_M_KDM4C 37197182 36900802
 SUM149_sgGrHL2_C_CTSL 45943203 45544150
 SUM149_sgScramble_C_CTSL 46167863 45737817
 SUM149_V5_H3_C_Ct 37016508 36623119
 SUM149_V5_H3_C_V5 36402115 36022268
 SUM149_V5_H3_M_Ct 35471500 35100958
 SUM149_V5_H3_M_V5 37951278 37567682
 SUM149_GFP_H3_C_Ct 40817278 40266728
 SUM149_GFP_H3_C_GFP 34433880 33954700
 SUM149_GFP_H3_M_Ct 33657105 33185044
 SUM149_GFP_H3_M_GFP 27536713 27151567
 HCC1806_sh5_Vehicle_Input 94096888 94075590
 HCC1806_sh5_Vehicle_H3K9me3_rep1 84424411 84476918
 HCC1806_sh5_Vehicle_H3K9me3_rep2 88802017 88854067
 HCC1806_sh5_Vehicle_H3K36me3_rep1 72683147 72701115
 HCC1806_sh5_Vehicle_H3K36me3_rep2 66996566 67012625
 HCC1806_sh5_shKDM4C_Input 82387126 82407395
 HCC1806_sh5_shKDM4C_H3K9me3_rep1 100552214 100617843
 HCC1806_sh5_shKDM4C_H3K9me3_rep2 99835844 99905731
 HCC1806_sh5_shKDM4C_H3K36me3_rep1 95469296 95497613
 HCC1806_sh5_shKDM4C_H3K36me3_rep2 95089343 95114661

Antibodies

Rabbit polyclonal KDM4C antibody Novus Biologicals Cat# NBP1-49600, RRID:AB_10011699
 Goat polyclonal Anti-cathepsin L antibody Novus Biologicals Cat# AF952, RRID:AB_355737
 Rabbit polyclonal Anti-GrHL2 antibody Sigma-Aldrich Cat# HPA004820, RRID:AB_1857928
 Rabbit polyclonal Anti-Histone H3 antibody (C-terminus) Abcam Cat# ab1791, RRID:AB_302613
 Rabbit polyclonal Anti-GFP antibody Novus Biologicals Cat# NB600-308, RRID:AB_10003058
 Rabbit polyclonal Anti-V5 Tag antibody Novus Biologicals Cat# NB600-381, RRID:AB_10001084
 Rabbit polyclonal Anti-Histone H3 (tri methyl K9) antibody Abcam Cat# ab8898, RRID:AB_306848
 Rabbit polyclonal Anti-Histone H3 (tri methyl K36) antibody Abcam Cat# ab9050, RRID:AB_306966
 Rabbit polyclonal Anti-Histone H3 (tri methyl K4) antibody Abcam Cat# ab8580, RRID:AB_306649
 Rabbit polyclonal Anti-Histone H3 (acetylation K27) antibody Diagenode C15410196, RRID:AB_2637079 (ChIP-seq)
 Rabbit polyclonal Anti-JMJD2A antibody Bethyl Laboratories Cat# A300-861A, RRID:AB_609461
 Rabbit polyclonal Anti-JMJD2B antibody Active Motif Cat# 61222, RRID:AB_2615033

Peak calling parameters

Peak calling is used the Model-Based Analysis of ChIP-seq 2 (MACS v2.1.2), with a q-value (FDR) threshold of 0.01.

Data quality

We evaluated multiple quality control criteria based on alignment information and peak quality: (i) sequence quality score; (ii) uniquely mappable reads (reads that can only map to one location in the genome); (iii) uniquely mappable locations (locations that can only be mapped by at least one read); (iv) peak overlap with Velcro regions, a comprehensive set of locations – also called consensus signal artifact regions – in the genome that have anomalous, unstructured high signal or read counts in next-generation sequencing experiments independent of cell line and of type of experiment; (v) number of total peaks (the minimum required was 1,000); (vi) high-confidence peaks (the number of peaks that are tenfold enriched over background); (vii) percentage overlap with known DHS sites derived from the ENCODE Project (the minimum required to meet the threshold was 80%); and (viii) peak conservation (a measure of sequence similarity across species based on the hypothesis that conserved sequences are more likely to be functional).

Software

CHIPS(<https://github.com/liulab-dfci/CHIPS>) for QC; BWA(<http://bio-bwa.sourceforge.net/>) for mapping; MACS2(<http://liulab.dfci.harvard.edu/MACS/>) for peak calling. ChIP-seq peak calling was performed using CHIPS pipeline and analyzed by Seqplots (v.1.12.0), BEDtools (v.2.30.0), deepTools (v.3.5.0).

Flow Cytometry

Plots

Confirm that:

- The axis labels state the marker and fluorochrome used (e.g. CD4-FITC).
- The axis scales are clearly visible. Include numbers along axes only for bottom left plot of group (a 'group' is an analysis of identical markers).
- All plots are contour plots with outliers or pseudocolor plots.
- A numerical value for number of cells or percentage (with statistics) is provided.

Methodology

Sample preparation	Reactive oxygen species levels were assessed using CellROX Green (Fisher Scientific) and CTSL Magic Red Assay Kit (MyBiosource) following manufacturer's protocol. Briefly, 2×10^5 cells seeded in 6 well plates and treated with DMSO, $1 \mu\text{g/ml}$ doxycycline or $1 \mu\text{M}$ QC6352 for 5 days. For flow cytometry, cells were first digested and then stained with $200 \mu\text{l}$ PBS solution containing 1x magic red and 1x CellROX green for 30 minutes in 37°C . Stained cells were dissociated to single cells and resuspended in $300 \mu\text{l}$ PBS and analyzed on BD LSRFortessa™ Cell Analyzer with FITC and PE-Texas Red channel. An unstained sample was used as negative control.
Instrument	BD LSRFortessa™ Cell Analyzer was used for flow cytometric analysis.
Software	BD FACSDiva™ Software was used to data collection and FlowJo v10.10 was used for data analysis.
Cell population abundance	Gates were conservative and consistent across samples to ensure purity within each independent experiment. We collected at least 10,000 cells per condition.
Gating strategy	FSC/SSC-area was used to select live cells and discriminate doublets. No further gating strategy was applied for the fluorescence analysis as statistic comparison was performed based on geometric mean of intensity merging from three independent experiments.

- Tick this box to confirm that a figure exemplifying the gating strategy is provided in the Supplementary Information.